UNIVERSITÄT BONN

Single-cell dissections of Rosette-to-Lumen stage embryoids - and the Glucose-6-phosphate isomerase-induced arthritis model

Dissertation

zur

Erlangung des Doktorgrades (Dr. rer. nat.)

der

Mathematisch-Naturwissenschaftlichen Fakultät

der

Rheinischen Friedrich-Wilhelms-Universität Bonn

in der Fachrichtung Molekulare Biomedizin

vorgelegt von

Arik Horne

aus

Waldbröl, Deutschland

Bonn, März 2023

Angefertigt mit Genehmigung der Mathematisch-Naturwissenschaftliche Fakultät
der Rheinischen Friedrich-Wilhelms-Universität Bonn

1. Gutachter: Prof. Dr. med. Joachim L. Schultze
2. Gutachter: Prof. Dr. rer. nat. Waldemar Kolanus

Tag der Promotion: 16.02.2024
Erscheinungsjahr: 2024

Eidesstattliche Erklärung

Hiermit versichere ich, dass die vorliegende Arbeit ohne unzulässige Hilfe Dritter and ohne die Benutzung anderer als der angegebenen Quellen angefertigt wurde. Die aus fremden Quellen direkt oder indirekt übernommenen Gedanken sind gemäß §10 der Promotionsordnung vom 17.02.2022 als solche kenntlich gemacht.

Die Erzeugung der RtL-embryoids and deren mikroskopische Analyse wurde von Jan Langkabel ausgeführt. Des Weiteren wurde zusammen mit Lisa Holsten die *in silico* Experimente für die Integration der RtL-embryoid Daten in einen Referenzdatensatz durchgeführt.
Die Seq-Well Experimente für die Erhebung des Einzelzell-Datensatz der G6PI-induzierten Arthritis wurden in enger Zusammenarbeit mit Dr. Nico Andreas aus der Arbeitsgruppe von Prof. Dr. med Thomas Kamradt durchgeführt.

Teile dieser Arbeit wurden bereits in folgenden Originalpublikationen veröffentlicht:

Langkabel, J**.**, **Horne, A**., Bonaguro, L., et al., 2021. Induction of Rosette-to-Lumen stage embryoids using reprogramming paradigms in ESCs. Nat Commun 12, 7322 (2021) DOI: https://doi.org/10.1038/s41467-021-27586-w

Langkabel, J., **Horne, A.**, Bonaguro, L., et al.,2021. Induction of peri-implantation stage synthetic embryos using reprogramming paradigms in ESCs. BioRxiv 2021.01.25.428068. DOI: 10.1101/2021.01.25.428068

Berlin, den……..

.....……

Arik Horne

Acknowledgement

It has been an exciting scientific journey over the last few years, and I am very thankful for the help and support I have received along the way.

To begin with, I would like to thank Prof. Dr. med. Joachim L. Schultze for his guidance. Thanks for the support, trust, and freedom you have given me to develop these projects. As a scientist, I can tell you that working with you was a pleasure.

I also want to thank PD Dr. med. Marc Beyer for introducing me to this working group and Prof. Dr. rer. nat. Waldemar Kolanus for being my second examiner.

Moreover, my special thanks go to Dr. Lorenzo Bonaguro, Dr. Kevin Baßler, and Lisa Holsten. It was terrific getting your advice and your support.

An important person for me was Dr. Jan Langkabel. Thank you for the 1 million phone calls and the outstanding collaboration for our paper. It was a pleasure to work with you. I would also like to thank Otwin Balser, who ignited in me the spark of passion for biology.

I would also like to thank some additional people of the AG Schultze and AG Beyer, Dr. Matthias Becker, Dr. Kristian Händler, Elke Meyer, Heidi Theis, Tarek Elmzzahi, Nico Reusch, Dr. Martina van Uelft, Jonas Schulte-Schrepping, Dr. Theo Kapellos, Michael Kraut, Dr. Tal Pecht, Dr. Elena De Domenico, Adem Saglam, Charlotte Kröger, Ioanna Gemünd, Dr. Thomas Ulas, Dr. Nico Andreas, Dr. Anna C. Aschenbrenner.

Also, I want to thank my friends for their help. To begin with, I would like to thank Dr. Marcel Hövels, who was with me when things were challenging and when they were good. Thank you for being my friend. I would also like to thank everyone in the “Schafott” because they always showed me that life is more than scientific work. Further, I want to thank Anne, Lukas, Philip, Beate, Sebastian, Monika, Kai, Kolja, and Thomas for being

good friends and for their constant support. Without you, I never would make it through the years. Thank you for making them so rewarding.

Zum Schluss möchte ich meiner Familie danken. Liebe Edeltraud Horne und Lore Schneider, vielen Dank, dass Ihr mir meinen Weg ermöglicht habt. Ich habe euch unendlich lieb. Lieber Roland Horne, danke auch Dir, dass Du in den schweren Momenten immer ein offenes Ohr hattest. Vielen Dank auch an Jonas, Jennifer, Tom, Elena, Norbert, Margret, and Monika.

Content

Table index

Figure index

Abbreviations

These abbreviations do not include gene names, chemicals, or acronyms for computational tools or wet lab technologies.

2D	2-dimensional
3D	3-dimensional
ArInf	arthritic inflammation
APCs	antigen-presenting cells
aSLFs	activated-sublining fibroblasts
AUC	area under the curve
AVE	anterior VE
CCs	chondrocytes
cDNA	complementary deoxyribonucleic acid
CPAs	citrullinated peptide antibodies
DCs	dendritic cells
DEGs	differentially expressed genes
DIExE	distal EXE
DMEM	Dulbecco’s modified Eagle’s medium
DOX	doxycycline
dsDNA	double-stranded DNA
DVE	distal VE
E	embryonic day
EBs	embryoid bodies
ECM	extracellular matrix
EmVE	embryonic VE
EPI	epiblasts
Epi-like	Epiblast-like
ER	endoplasmic reticulum
ERK	extracellular-signal-regulated kinases

ESCs	embryonic stem cells
ETX	ESC + TSC + XEN embryos
ExE	extraembryonic ectoderm
ExE-like	extraembryonic ectoderm-like
ExVE	extraembryonic VE
FACS	fluorescence-activated cell sorting
FCS	fetal calf serum
FGF	fibroblast growth factor
G6PI	glucose-6-phosphate isomerase
GEO	Gene Expression Omnibus
GFP	Green Fluorescent Protein
GOEA	Gene Ontology Enrichment Analysis
HLA	human leukocyte antigens
IF	immunofluorescence
hSLFs	healthy-sublining fibroblasts
ICM	inner cell mass
iETX	induced ESC + TSC + XEN embryos
iTSC	induced trophoblast stem cell
iXEN	induced extraembryonic endoderm stem cell
LLFs	synovial lining layer fibroblasts
MHC	major histocompatibility complex
MHC I	MHC class I
MHC II	MHC class II
MMP	Matrix metalloproteinases
mRNA	messenger ribonucleic acid
NK cells	natural killer cells
OA	osteoarthritis
PAMPs	pathogen-associated molecular patterns
PBS	phosphate-buffered saline

PCs	principal components
PE	primitive endoderm
pERK	phosphorylated ERK
PGC	primordial germ cell
PrExE	proximal ExE
RA	Rheumatoid arthritis
scRNA-seq	single-cell ribonucleic acid sequencing
SDS-PAGE	sodium dodecyl sulfate-polyacrylamide gel electrophoresis
SFs	synovial fibroblasts
SLFs	sublining fibroblasts
SLMs	synovial lining macrophages
TCRs	T cell receptors
TE	trophectoderm
TF	transcription factor
TPM	transcripts per million reads
Tregs	regulatory T cells
TSCs	trophoblast stem cells
UMAP	Uniform manifold approximation and projection
UPR	Unfolded Protein Response
VE	visceral endoderm
VE-like	visceral endoderm-like
XEN	extraembryonic endoderm

List of publications

1. *“Decoding mechanism of action and sensitivity to drug candidates from integrated transcriptome and chromatin state”*
   Caterina Carraro, Lorenzo Bonaguro, Jonas Schulte-Schrepping, **Arik Horne**, Marie Oestreich et al., 2022.
   eLife **11**:e78012.
   doi: https://doi.org/10.7554/eLife.78012

2. “*Inflammatory blood neutrophils in COPD stem from activated bone marrow progenitors*”
   Theodore Kapellos, Kevin Bassler, Wataru Fujii, Tal Pecht, Lorenzo Bonaguro, Iz abela Galvao, Adem Saglam, Erica Dudkin, Amit Frishberg, Elena De Domenico, **Arik Horne** et al., 2022.
   ERJ Open Research 2022 8: 210
   doi: 10.1183/23120541.LSC-2022.210

3. *“Alveolar macrophages in early stage COPD show functional deviations with properties of impaired immune activation”*
   Kevin Baßler, Wataru Fujii, Theodore S Kapellos, Erika Dudkin, Nico Reusch, **Arik Horne**, Benedikt Reiz et al.,2022.
   Frontiers in Immunology 13 (2022).
   doi: 10.3389/fimmu.2022.917232

4. “*Decoding mechanism of action and susceptibility to drug candidates from integrated transcriptome and chromatin state*”
   Caterina Carraro, Lorenzo Bonaguro, Jonas Schulte-Schrepping, **Arik Horne**, Marie Oestreich, Stefanie Warnat-Herresthal et al., 2022.
   bioRxiv, Cold Spring Harbor Laboratory

doi: https://doi.org/10.1101/2022.02.21.481294

5. *"Induction of Rosette-to-Lumen stage embryoids using reprogramming paradigms in ESCs"*
   Jan Langkabel, **Arik Horne**, Lorenzo Bonaguro, Lisa Holsten et al., 2021.
   Nat Commun 12, 7322 (2021)
   doi: https://doi.org/10.1038/s41467-021-27586-w

6. "*Disease severity-specific neutrophil signatures in blood transcriptomes stratify COVID-19 patients*"
   Anna C. Aschenbrenner, Maria Mouktaroudi, Benjamin Krämer, Marie Oestreich, Nikolaos Antonakos, Melanie Nuesch-Germano, Konstantina Gkizeli, […], **Arik Horne** et al., 2021.
   Genome Med 13, 7 (2021)
   doi: https://doi.org/10.1038/s41467-021-27586-w

7. "*Late Breaking Abstract - Blood and bronchoalveolar neutrophil signatures associate with COPD severity*"
   Theodore Kapellos, Kevin Bassler, Wataru Fujii, Christina Nalkurthi, Amit Frishberg, Tal Pecht, Lorenzo Bonaguro, Erika Dudkin, Elena De Domenico, Adem Saglam, **Arik Horne** et al., 2021.
   European Respiratory Journal 2021 58: OA1596
   doi: 10.1183/13993003.congress-2021.OA1596

8. *"Induction of peri-implantation stage synthetic embryos using reprogramming paradigms in ESCs"*
   Jan Langkabel, **Arik Horne**, Lorenzo Bonaguro, Tatiana Hesse, Alexej Knaus, Yannick Riedel, Kristian Händler et al., 2021
   bioRxiv, Cold Spring Harbor Laboratory
   doi: https://doi.org/10.1101/2021.01.25.428068

9. "*CRELD1 modulates homeostasis of the immune system in mice and humans*"
   Lorenzo Bonaguro, Maren Köhne, Lisa Schmidleithner, Jonas Schulte-Schrepping, Stefanie Warnat-Herresthal, **Arik Horne**, Paul Kern, Patrick Günther et al., 2021.
   Nat Immunol 21, 1517–1527 (2020).
   doi: https://doi.org/10.1038/s41590-020-00811-2

10. "*Severe COVID-19 Is Marked by a Dysregulated Myeloid Cell Compartment*"
    Jonas Schulte-Schrepping, Nico Reusch, Daniela Paclik, Kevin Baßler, Stephan Schlickeiser, Bowen Zhang, Benjamin Krämer, Tobias Krammer, Sophia Brumhard, Lorenzo Bonaguro, Elena De Domenico, […], **Arik Horne**, Miriam Herbert et al., 2020.
    Cell, September. 182 (6): 1419–1440.e23
    doi: https://doi.org/10.1016/j.cell.2020.08.001

11. "Cxcr4 distinguishes HSC-derived monocytes from microglia and reveals monocyte immune responses to experimental stroke"
    Yves Werner, Elvira Mass, Praveen Ashok Kumar, Thomas Ulas, Kristian Händler, **Arik Horne**, Kathrin Klee, Amelie Lupp, Dagmar Schütz et al., 2020.
    Neurosci 23, 351–362 (2020)
    doi: https://doi.org/10.1038/s41593-020-0585-y

12. "*Suppressive myeloid cells are a hallmark of severe COVID-19*"
    Jonas Schulte-Schrepping, Nico Reusch, Daniela Paclik, Kevin Baßler, Stephan Schlickeiser, Bowen Zhang, Benjamin Krämer, […]**, Arik Horne**, Miriam Herbert et al., 2020.
    medRxiv, Cold Spring Harbor Laboratory
    doi: https://doi.org/10.1101/2020.06.03.20119818

13. *"Alterations of multiple alveolar macrophage states in chronic obstructive pulmonary disease"*
    Kevin Baßler, Wataru Fujii, Theodore S Kapellos, **Arik Horne**, Benedikt Reiz, Erika Dudkin, Malte Lücken, Nico Reusch et al., 2020.
    bioRxiv, Cold Spring Harbor Laboratory
    doi: https://doi.org/10.1101/2020.05.28.121541

14. *"Disease severity-specific neutrophil signatures in blood transcriptomes stratify COVID-19 patients"*
    Thomas Ulas, Lea Seep, Jona Schulte-Schrepping, Elena De Domenico, Simachew Mengiste, Heidi Theis, Michael Kraut, Matthias Becker, Jannik Gierlich, Lena Lenkeit, Anna Drews, Martina van Uelft, Kilian Dahm, Shobhit Agrawal, Ioanna D Gemuend, **Arik Horne**, Lisa Holsten et al., 2020.
    medRxiv, Cold Spring Harbor Laboratory
    doi: https://doi.org/10.1101/2020.07.07.20148395

15. "Fate mapping reveals a Cxcr4-dependent immune response of monocytes to experimental stroke"
    E Mass, Y Werner, T Ulas, K Haendler, **A Horne**, K Klee, PA Kumar, D Schuetz, F Saaber, C Redecker, JL Schultze, F Geissmann, R Stumm et al., 2019.
    European journal of immunology., 2019, Vol.49
    doi: 10.1002/eji.201970300

Summary

Single-cell omics (SCO), particularly single-cell RNA-sequencing (scRNA-seq), are widely used to describe dynamic biological and pathophysiological processes. This thesis explores the utility of SCO in characterizing dynamic processes in the in vitro generation of embryo-like structures and a pathophysiological condition in tissue usually sparse in cells, the joint. More specifically, scRNA-seq was used to analyze the transcriptional signatures of cells obtained from a new stem-cell-based embryo model, the Rosette-to-Lumen stage embryoids (RtL-embryoids) and an established glucose-6-phosphate isomerase (G6PI) regulatory T cells (Tregs) depletion model for the induction of acute and chronic arthritis.

In 3 dimensional (3D) cell culture environments, blastocyst-derived stem cell lines are self-organized into embryolike structures. Using a 3D cell co-culture system, embryo-like structures can be generated based on transcription factor-mediated reprogramming of embryonic stem cells. In these cultures, embryonic stem cells self-organize into compartmentalized, elongated structures that mimic the inner regions of the early postimplantation embryos. The Smart-Seq 2 scRNA-seq protocol was used to identify transcriptomic profiles similar to epiblasts, primitive-/visceral endoderm, and extraembryonic ectoderms of early murine embryos around E4.5 to E5.5. SCOs revealed how stem-cell-based embryos progressed from rosette formation to lumenogenesis, followed by epiblast-like cells development from naïve- to primed pluripotency. In addition, lineage specification of primordial germ cells and distal/anterior visceral endoderm-like cells were observed respectively in epiblast- or visceral endoderm-like compartments. Applying SCO to RtL-embryoids led to new findings in early embryogenesis.

Murine models of induced arthritis are valuable tools for studying the pathogenic process of arthritic inflammation (ArInf). For example, G6PI-induced arthritis is a spontaneously remitting experimental arthritis model in which the depletion of Tregs can further modulate to induce non-remitting, chronic, and destructive arthritis. The Seq-Well scRNA-seq platform was applied to describe mesenchymal and immune cells in ArInf. Sampling over

time allowed us to define dynamic processes of transcription in individual cells during ArInf. Here, an increased gradient of Notch signaling was identified between sublining fibroblasts (SLFs) and lining layer fibroblasts (LLFs). Furthermore, in ArInf, a counteractive *Prg4* gradient was observed in fibroblasts of the synovium, which was tightly restricted to the lining layer of fibroblasts in the healthy synovium. This counteractive *Prg4* gradient was connected to the loss of synovial barrier integrity formed by a distinct population of Cx3cr1^{+} tissue-resident macrophages, which get lost in ArInf. Arthritis remission and expansion of this specialized macrophage subcluster resulted in a reduced expression of *Prg4* in the SLFs. ScRNA-seq provided a cellular framework for understanding the pathomechanisms of ArInf, which is a prerequisite for developing new therapies for this disease.

In conclusion, scRNA-seq provided considerable insight into the development of RtL-embryoids but is equally suited to identifying rare cell populations in complex tissue under pathophysiological conditions.

Zusammenfassung

Einzelzell-Genomik insbesondere Einzelzell-RNA-Sequenzierung, wird zunehmend zur Beschreibung dynamischer biologischer und pathophysiologischer Prozesse eingesetzt. In dieser Arbeit habe ich mich mit der Frage beschäftigt, ob die Einzelzell-Genomik am aussagekräftigsten ist, um dynamische Prozesse bei der *in vitro* Erzeugung von Embryo-ähnlichen Strukturen, in einem halbkünstlichen Zellsystem und bei einem pathophysiologischen Zustand in einem normalerweise zellarmen Gewebe zu beschreiben, dem Gelenk. Insbesondere habe ich scRNA-seq verwendet, um die Transkriptionssignaturen von Zellen zu analysieren, die aus einem neuen stammzellbasierten Embryomodell (Embryoide im Rosetten-zu-Lumen-Stadium) und einem etablierten Modell zur Depletion von regulatorischen T-Zellen für die Induktion von akuter und chronischer Arthritis stammen. Aufgrund der Unterschiede in den modellierten biologischen Systemen befassen sich die Hauptabschnitte dieser Arbeit mit der Analyse von Embryoiden im Rosette-to-Lumen-Stadium und dem Modell der Depletion von regulatorischen T-Zellen in der Glukose-6-Phosphat-Isomerase induzierten Arthritis.

In 3D-Zellkulturumgebungen organisieren sich die aus Blastozysten gewonnenen Stammzelllinien selbst zu embryoähnlichen Strukturen. Mit Hilfe eines 3D-Zell-Kokultursystems können embryoähnliche Strukturen durch Transkriptionsfaktor-vermittelte Reprogrammierung von embryonalen Stammzellen erzeugt werden. In diesen Kulturen organisieren sich die embryonalen Stammzellen selbst zu kompartimentierten, länglichen Strukturen, die die inneren Regionen des frühen Postimplantationsembryos ähnlich sind. Das hochempfindliche Smart-Seq 2 einzelzell-RNA-sequenzierungs Protokoll wurde verwendet, um transkriptomische Profile zu identifizieren, die Epiblasten, primitivem/visceralem Endoderm und extraembryonalen Ektodermen von frühen Mäuseembryonen um E4.5 bis E5.5 ähneln. Einzelzell-Genomik zeigten im Detail, wie stammzellbasierte Embryonen von der Rosettenbildung zur Lumenogenese fortschreiten, gefolgt von der Entwicklung der Epiblast ähnlichen Zellen von der naiven zur primären Pluripotenz. Darüber hinaus wurde die differenzierung von primordialen Keimzellen und

distalen/anterioren viszeralen Endoderm-ähnlichen Zellen in epiblastischen- bzw. viszeralen Endoderm-ähnlichen Kompartimenten beobachtet. Die Anwendung von Einzelzell-Genomik auf dieses *in vitro* System für schnelle und reproduzierbare embryoähnliche Strukturen führte zu wichtigen neuen Erkenntnissen über die Mechanismen der frühen Embryogenese.
Murine Modelle der induzierten Arthritis sind nützliche Instrumente zur Untersuchung des pathogenen Prozesses arthritischer Entzündungen. Die durch Glukose-6-Phosphat-Isomerase induzierte Arthritis ist ein spontan remittierendes experimentelles Arthritismodell, das durch Depletion von regulatorischen T-Zellen weiter moduliert werden kann, um eine chronische und destruktive Arthritis zu induzieren. Ich habe die kostengünstige Seq-Well einzelzell-RNA-sequenzierungs Plattform eingesetzt, um Mesenchymale- und Immunzellen bei akuten und chronischen Entzündungen zu beschreiben. Anhand von Zellisolaten an bestimmten Zeitpunkten in der arthritischen Entzündung konnte ich dynamische Prozesse in einzelnen Zellen im Gelenk definieren. Hier konnte ich einen verstärkten Gradienten der Notch-Signalisierung innerhalb synovialen Fibroblasten feststellen. Dies war auch in arthritischen Chondrozyten zu beobachten.

Darüber hinaus wurde bei akuter und chronischer Arthritis ein gegenläufiger *Prg4*-Gradient in Fibroblasten der Synovialis beobachtet. Die Expression von *Prg4* war in der gesunden Synovialis eng auf die Fibroblasten der inneren Gelenkschicht beschränkt. Dieser gegenläufige *Prg4*-Gradient wurde mit dem Verlust der Integrität der synovialen Barriere in Verbindung gebracht, die durch eine bestimmte Population von Cx3cr1^{+}-Makrophagen im Gewebe gebildet wird, die bei akuter und chronischer Arthritis verloren gehen. In der Remission der Arthritis verringerte sich die Expression von *Prg4* in den Fibroblasten, der inneren Synovialis. Mit dieser Arbeit zeigen wir, dass die Einzelzell-RNA-Sequenzierung eingesetzt werden kann, um dynamisch Pathomechanismen der arthritischen Entzündung zu verstehen, welches eine Voraussetzung ist für die Entwicklung neuer Therapien in diesem Feld ist.

In Anbetracht dieser Ergebnisse lieferte die Einzelzell-RNA-Sequenzierung bedeutende Einblicke in die Entwicklung von *in vitro* erzeugten embryoähnlichen Strukturen, ist aber ebenso geeignet, seltene Zellpopulationen in komplexem Gewebe unter pathophysiologischen Bedingungen zu identifizieren.

1 Introduction

SCOs have been increasingly used, particularly scRNA-seq, which is suited to describe dynamic biological and pathophysiological processes. This method was used to characterise a semi-artificial cell system, the RtL-embryoids, and sparse cell types in the joint under pathophysiological conditions with the G6PI-T-reg depletion model.
The introduction should outline the path literature has taken to create the foundations for these two model systems and provide the basic knowledge for this thesis.

1.1 Introduction for the analysis of the RtL-embryoid Smart-seq2 dataset

In vitro models of mammalian embryogenesis based on cell culture are gaining increasing attention from scientists thanks to their ability to recapitulate embryogenesis or specific developmental hallmarks. This section describes the basic knowledge of early mouse embryogenesis and embryonic stem cells (ESCs). A comprehensive starting point is given here for an in deeps SCO analysis.

1.1.1 Early mouse embryogenesis

At the beginning of murine embryonic development, the morula becomes compacted and gradually differentiates into the trophectoderm (TE) around the inner cell mass (ICM) (Johnson, 1981). The second cell fate decision is followed by embryonic day (E) 3.5 when ICM has been segregated into pluripotent epiblasts (EPI) and primitive endoderm (PE), arranged as a salt-and-pepper pattern. A layer of PE cells forms on the surface of the blastocoel cavity during the late blastocyst stage (**Figure 1**). The EPI gives rise to the embryo, amnion, and extraembryonic mesoderm of the yolk sac. The placenta is formed by TE cells, and the PE creates the extraembryonic ectoderm (ExE) linages (Chazaud et al., 2006; Plusa et al., 2008). As the visceral endoderm (VE) develops, it encloses the Epi and the ExE. The PE cells migrate along the inner surface of TE to form a membrane in

conjunction with trophoblast giant cells (**Figure 1**). The structure being referred to is a thick, multilayered basement membrane located between the parietal endoderm cells and the trophoblast cells in rodents. It is primarily composed of collagen and laminin proteins (Hogan et al., 1980). The primary function of this membrane is the physical separation of the embryo and the maternal cells while allowing nutrition to pass (Gardner, 1983).

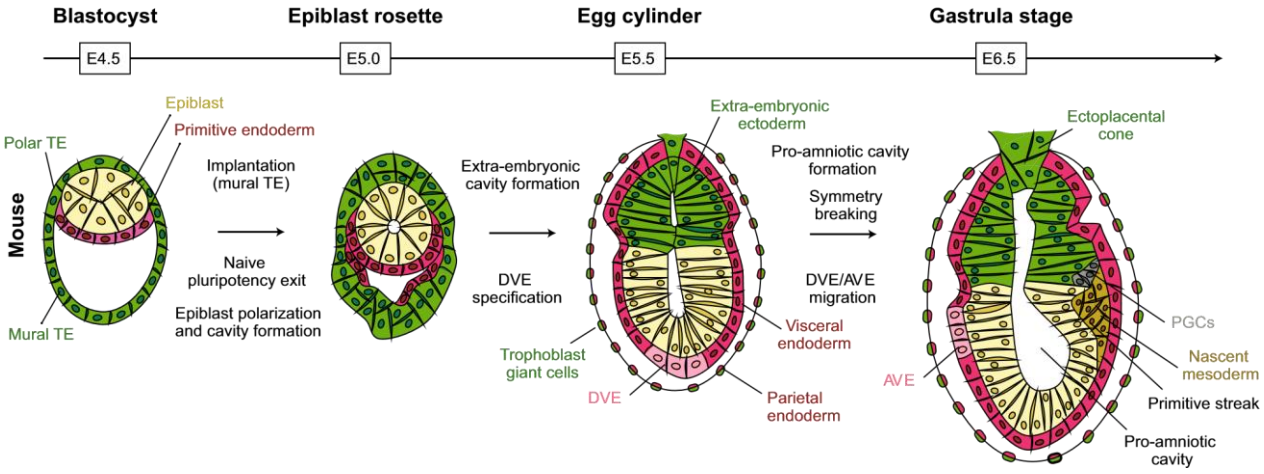

Figure 1. Overview of mouse development from E4.5 to E6.5

The blastocyst in the mouse is ready to implant into the uterus by E4.5. This stage comprises the naive pluripotent epiblast and two extraembryonic tissues, trophectoderm (TE) and primitive endoderm (PE). Trophectoderm plays a fundamental role in the process of implantation. Exiting from naive pluripotency and upon exposure to the extracellular matrix secreted by the extraembryonic tissues, the epiblast undergoes polarization, rosette formation, and subsequent lumenogenesis. During E5.5, the polar trophectoderm forms the extraembryonic ectoderm adjacent to the epiblast and undergoes lumen formation. The pro-amniotic cavity is formed by fusing the extraembryonic ectoderm (EXE) and epiblast cavity. The visceral endoderm originates from the PE and surrounds both tissues. The PE is also responsible for forming the parietal endoderm adjacent to trophoblast giant cells derived from the mural trophectoderm. Distal visceral endoderm (DVE) and anterior visceral endoderm (AVE) are subsets of visceral endoderm cells, which migrate to the epiblast-EXE boundary to determine the future anterior side of the embryo. The primitive streak develops in the posterior epiblast by E6.5, gastrulation begins, and Primordial germ cells (PGCs) become distinct at the boundary between the posterior epiblast and EXE (Figure taken from Shahbazi and Zernicka-Goetz, 2018).

The VE cells surround the EPI and ExE. The VE cells are morphologically and transcriptionally distinct at E5.0 and represent embryonic VE (EmVE) and extraembryonic VE (ExVE) (Langkabel et al., 2021). It is important to note that the EmVE cells are flatter and look more like epithelial cells, whereas the ExVE cells are cube-shaped (Takaoka et al., 2011). Until E5.5, the EmVE starts to migrate proximally to the embryo and forms the distal VE (DVE), which represents an essential signalling center of early embryogenesis. The next step in this process is a migration of DVE cells to the proximal-anterior region of the embryo, forming the anterior VE (AVE) required for anterior-posterior axis patterning in the anterior-posterior axis of the early mouse embryo (**Figure 1**). AVE and proximal epiblast are critical signaling centers for establishing the anterior-posterior axis (Rodriguez et al., 2005; Takaoka et al., 2011).

Between E5.0 and E5.5, the proximal epiblast signalling center is induced in a rim at the boundary between EPI and ExE. Reciprocal interactions between EPI, VE, and ExE are crucial for establishing these signaling centers. At the same time, a gradient of FGFR-dependent extracellular-signal-regulated kinases (ERK) activation shaps the morphology of the ExE. Starting at E5.5, activation of the ERK signaling pathway became localized to a ring-shaped region in the innermost, proximal area of the ExE. This pattern of ERK activation gradually decreased in intensity in the following days. However, the ectoplacental cone, which marks the most distal end of the ExE, exhibits an ERK activation sustained in the central cell population (Corson et al., 2003).

1.1.2 From Embryonic stem cells to Embryoid bodies

ESCs can be classified as pluripotent stem cells derived from the ICM of a preimplantation embryo at the early stage. ESC can self-renew endlessly *in vitro* and differentiate into all three primitive germ layers - mesoderm, ectoderm, endoderm, and germ cells. ESCs were first derived from murine embryos (Evans and Kaufman, 1981; Martin, 1981), and human ESC lines followed (Reubinoff et al., 2000). As a next step, a method for generating pluripotent cells was developed by combining embryonic genes with somatic cells through

retroviral transduction. Both mice and human somatic cells can be reprogrammed into induced pluripotent stem cells (iPS) with similar differentiation capacities and self-renewal abilities to ESCs (Takahashi and Yamanaka, 2006; Takahashi et al., 2007).

The ability of ESCs or iPS cells to contribute to all tissues of an organism can be tested by introducing the cells into a blastocyst-stage embryo (Gossler et al., 1986). In addition, injections of ESCs into various tissues of adult organisms cause teratomas, which contain cells from the three germ layers disorganized into benign tumors. Blastocyst injection and teratoma studies demonstrate that the environment into which pluripotent cells are introduced can influence differentiation. However, while *in vivo* studies have some mechanistic insights into how environmental factors may affect stem cell differentiation, they are limited in providing mechanical information. ESC differentiation *in vitro*, on the other hand, allows for more controlled methods of presenting morphogens in the microenvironment of the stem cell and directly assessing differentiated cell phenotypes. ESC differentiation *in vitro* is typically induced in two ways: monolayer culture on defined matrices (Ying et al., 2003) and the formation of embryoid bodies (EBs) in suspension (Doetschman et al., 1985). In monolayer culture, ESCs are maintained in a more defined substrate and are constantly exposed to soluble media components. However, ESCs are arranged in 3D aggregates in EBs that more accurately mimic the complex assembly of cell adhesions and intercellular signaling during early embryogenesis.

1.1.3 ESC differentiation in EBs

The improvement of cellular differentiation in EBs made it possible to observe genetic defects in ESCs in a complex environment that would be lethal in normal embryonic development. (Li et al., 2001; Wu et al., 2007). The differentiation process of EBs begins with the formation of aggregated ESCs, whose size is regulated by the number of cells that self-assemble by cell-cell adhesion receptors (Dang et al., 2004; Larue et al., 1996). After the cell aggregation, the first sign of differentiation is the spontaneous formation of a layer of PE on the exterior surface of the EBs (Maurer et al., 2008). The PI 3-kinase pathway is responsible for forming a PE layer on the exterior of EBs in combination with fibroblast growth factor (FGF) signaling (Chen et al., 2000; Esner et al., 2002). The PE

cells exhibit an epithelial morphology on the EB surface, differentiate further into VE and parietal endoderm, and deposit a basement membrane rich in laminin and collagen IV (Li et al., 2001). In most EBs, cystic cavities result from the apoptosis of cells not in contact with the basement membrane dividing the PE cell layer from the remaining mass of undifferentiated cells (Murray and Edgar, 2000; Yu et al., 2007).

The results of microarray analysis indicate that EBs express genes that reflect the sequence of normal development, such as primitive ectoderm formation and gastrulation (Dvash et al., 2004). Furthermore, EBs can generate various cells in all three germ layers (Itskovitz-Eldor et al., 2000). Collectively, with 3D aggregates of pluripotent stem cells, it is possible to observe early ES cell differentiation in a spatiotemporal manner until specific developmental stages.

1.1.4 Embryoid differentiation to early embryo-like structures

From a blastocyst, three distinct stem cell types can be generated and propagated indefinitely: trophoblast stem cells (TSCs) (Tanaka et al., 1998) and ESCs (Evans and Kaufman, 1981), and extraembryonic endoderm (XEN) (Kunath et al., 2005) stem cells. Previous studies demonstrated that blastocyst-derived stem cells (ESCs, TSCs, and XEN cells) could form early embryo-like structures, forming tissues resembling early inner embryonic architecture when co-cultured in 3D cell culture environments (Sozen et al., 2018; Zhang et al., 2019b).

Several key features of embryogenesis are visible in these structures, including patterning events, and they have been shown to implant into the uterus (Zhang et al., 2019b). However, implantation that occurs at the blastocyst stage, mediated by trophectoderm, must be considered a question since trophectoderm is absent from the previously described embryo model. Therefore, whether the observed implantations are mechanically induced uterine reactions must be examined. Nevertheless, these models can simulate specific developmental events during early embryogenesis.

Precise timing is critical for the successful generation of stem cell-based embryo models due to differences in proliferation and cell cycle. However, researchers have found that a

population of TSCs and two ESC lines can be combined to generate induced ESC + TSC + XEN embryos (iETX) (Amadei et al., 2021). By overexpressing Gata4, one of these ESC lines can be reprogrammed to become VE-like. This new system has significantly better developmental potential than previously presented ESC + TSC + XEN embryos (ETX) (Sozen et al., 2018), relying on ESC culture without transcription factor (TF) overexpression. iETX embryos establish a robust anterior signaling center that migrates unilaterally to create the embryo's symmetry. Additionally, these embryos undergo gastrulation, generating embryonic and extra-embryonic mesoderm, as well as definitive endoderm. Therefore, these fully formed embryoids serve as a potent *in vitro* model for investigating the functions of various cell lineages and genes in development. By providing an environment that mimics *in vivo* embryonic development, these models enable researchers to study complex developmental processes in a more controlled and manipulable setting.

1.2 Introduction for the analysis of the G6PI induced arthritis Seq-Well dataset

Experimental models are crucial for understanding the pathophysiological conditions of complex diseases. The combination of SCO and the G6PI-T-reg depletion model allows the detection of rare cell types in the synovial microenvironment and their specific function in the ArInf. This section includes an overview of the immune system and cellular composition of the synovium. Furthermore, it contains an introduction to rheumatoid arthritis, the current modeling approaches for arthritis, and the recent SCO approaches in the arthritic field.

1.2.1 The immune system

The immune system is a biological defense of higher organisms that prevents tissue damage caused by pathogens. It is a complex of cellular, chemical, and mechanical mediators evolved and adapted to protect the organism from every challenge that can endanger its vitality and function. A significant difference from other organ systems in the human body is that the immune system must have the potential to be activated when needed and consequently inactivated when the possible danger has been cleared (Parkin and Cohen, 2001). This system must be controlled to maintain this balance between initiation and insensitivity. Interference of this mechanism has pathological outcomes. For example, an uninhibited reaction can lead to autoimmunity, although an insufficient response is associated with cancer or chronic infection (Hu et al., 2018).

The immune system is traditionally separated into two major parts, the innate and the adaptive immune system (**Figure 2**). The innate immune system functions as the first line of defense and allows a direct response against pathogens. The innate immune cells are called myeloid cells and include monocytes, macrophages, dendritic cells (DCs), mast cells, and granulocytes, including neutrophils, eosinophils, and basophils. In cells of innate immunity, the complement system recognizes conserved patterns like pathogen-associated molecular patterns (PAMPs), which appear on microbes and are absent in endogenous cells (Ricklin et al., 2010). The binding of PAMPs by pathogen recognition receptors is followed by initiating an effector phase and clearance of the infection.

However, PAMPs are shared by different classes of pathogens, and therefore the innate immune response is not specific but without delay against a general pathogen class (Medzhitov and Janeway, 2000).

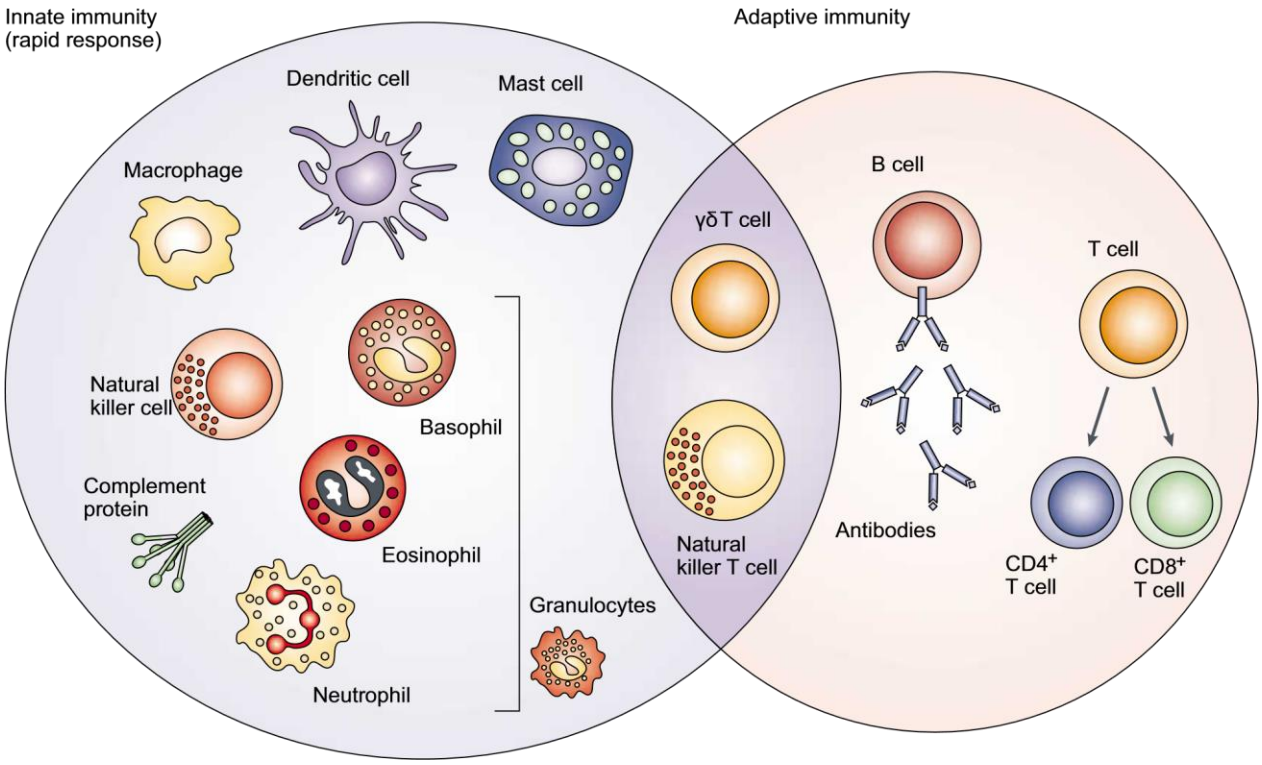

Figure 2. The innate and adaptive immune system

The innate immune system is the first line of defense for the body against infection. Comprised of soluble mediators (complement proteins) and several cell types, including granulocytes (basophils, neutrophils, and eosinophils), monocytes, macrophages, dendritic cells, mast cells, and ILCs. The innate immune system responds quickly and non-specifically to pathogens and can also activate the adaptive immune system. The adaptive response is slower but provides high specificity and cellular memory, composed of B and T cells, γδ T cells, and Natural killer T cells. Natural killer T cells and γδ T cells are cytotoxic lymphocytes on the boundary between innate and adaptive immunity (Figure taken from Dranoff, 2004).

The adaptive immune system is highly specific for the recognition of pathogens. It expands and adapts throughout an individual's lifetime, but the response is slower than innate immunity. This specific immune response is known as lymphocytic mediated. However,

the adaptive immune system becomes activated by the innate immune system, enabling a pathogen-specific immune response. Antigen-presenting cells (APCs), mainly DCs, activate B and T lymphocytes by migrating from the specific and processed antigens on major histocompatibility complex (MHC) to the secondary lymphatic organs at the same time upregulating co-stimulatory molecules and producing cytokines (Schenten and Medzhitov, 2011). However, the adaptive immune response is performed by lymphocytes and includes T cells and B cells. The specificity of T cells and B cells towards a pathogen originates from surface proteins that recognize particular molecular structures. T cells carry the T cell receptors (TCRs) on their surface, which are specialized in creating a wide range of antigen-specificities. Each T cell carries TCRs of unique antigen specificity. This principle of significant receptor variability in recognizing a wide range of molecular patterns is also found in immunoglobulins or antibodies expressed by B cells. T and B cells develop their specificity against specific antigens by randomised rearrangement of a genomic locus coding for the TCR and B cell receptor (Medzhitov and Janeway, 2000). This process is based on recombination and can lead to the generation of T or B cell clones. Every clone can bind to a specific exogenous peptide bound to MHC class I (MHC I) or II on the surface APCs, such as DCs, monocytes, and macrophages, connecting innate and adaptive immune systems.

The MHC surface receptors for antigen presentation are classified into MHC I and class II (MHC II) molecules. MHC II molecules are primarily found at the surface of APCs and present antigens derived from extracellular pathogens (Rock et al., 2016) processed after phagocytosis. In contrast, MHC I molecules are expressed by all cells with a nucleus and present antigens of intracellular pathogens during infection (Rock et al., 2016). MHC I present peptides obtained by the regular cellular protein turnover during homeostasis. The constant presentation of loaded MHC I molecules on the surface of all nucleated body cells is an immunological safety net for the body since the MHC I molecule serves as an inhibitory ligand for natural killer cells (NK cells). Some viral infections (Hansen and Bouvier, 2009) and cancer cells (Garrido et al., 2016) cause a reduction in MHC I surface protein concentration. However, this reduced concentration activates NK cells, leading to NK cell-mediated killing of the cell (Höglund and Brodin, 2010).

Collectively, the immune system of vertebrates is a highly organized and complex of cells interacting with each other to form a variety of defense mechanisms against pathogenic influences.

1.2.2 Anatomical structure and cellular composition of synovial joints

Synovial joints are characterized by a joint gap between the articulating skeletal elements filled with synovial fluid (Waschke et al., 2015) (**Figure 3**). The synovial joints are also characterized by cartilage covering the articular surfaces, an articular capsule surrounding the entire joint, ligaments that stabilize the capsule, and muscles that enable movement (Waschke et al., 2015). The collagenous extracellular matrix (ECM) necessary for cartilage formation is produced by specialized cells called chondrocytes (CCs) (Buffrénil and Quilhac, 2021). The synovial fluid is a viscous transudate from the blood, and it contains hyaluronic acid proteins like lubricin, encoded by the *Prg4* gene. The synovial fluid serves several essential functions in the joint, including nourishing the joint cells, providing lubrication, and absorbing shock (Waschke et al., 2015). There are two layers of the joint capsules: an outer fibrous layer (synovial-sublining layer) and a thin inner layer (synovial-lining layer) (Culemann et al., 2019a) (**Figure 3**). The synovial-lining layer, as the name says, lines the joint space and consists of two distinct cell types synovial lining macrophages (SLM) and lining layer fibroblasts (LLFs) (Culemann et al., 2019a). These two cell types form a boundary membrane between the synovial fluid and subsynovial interstitial fluid. The subsynovial interstitium contains a large number of lymphatic and blood vessels as well as SLFs and interstitial macrophages (Culemann et al., 2019a; Waschke et al., 2015).

In contrast, the synovial fluid in the joint space is almost free from immune cells (Orr et al., 2017). Although synovial joints experience extreme mechanical stress and the surrounding tissues release large amounts of inflammation-stimulating metabolic products like hyaluronic acid-derived products, this does not activate the immune system. Because of the high number of macrophages and the specialized morphology, synovial joints appear as immune-privileged tissue (Culemann et al., 2019a).

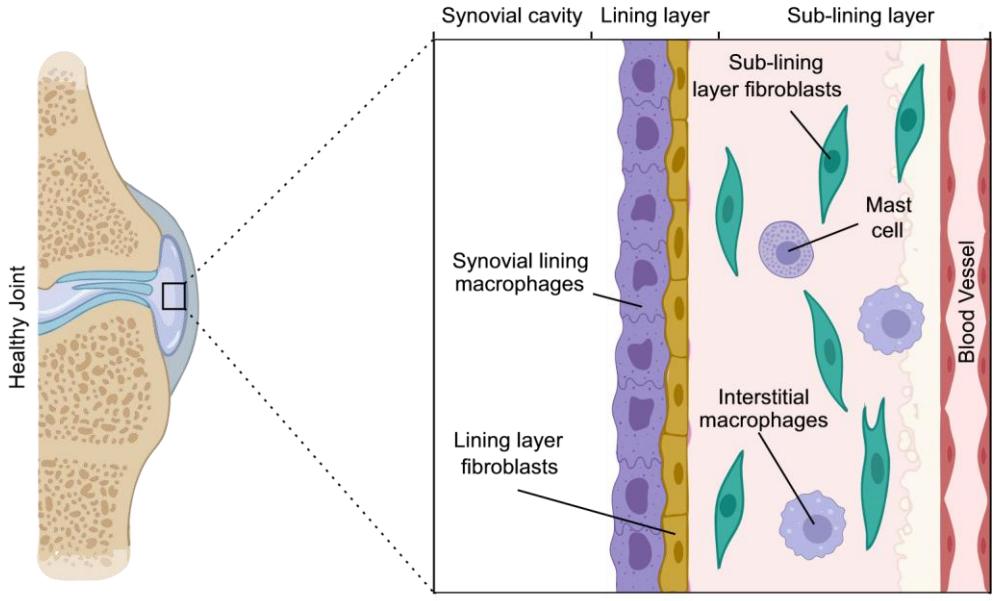

Figure 3. Architecture and cell composition of the synovium

Synovial tissue is composed mainly of two cell types: tissue-resident macrophages and synovial fibroblasts. The tissue macrophages include an immune-regulatory population of interstitial macrophages located in the sublining layer. The lining layer consists of highly organized synovial lining macrophages that form an immunological barrier. Adjacent to the lining layer are lining layer fibroblasts, which secrete hyaluronic acid and lubricin into the synovial cavity to provide lubrication. The sublining layer contains sublining fibroblasts and interstitial macrophages, which play a crucial role in the formation and remodeling of the extracellular matrix. Together, these cell populations contribute to the maintenance of the synovial tissue's structure and function, including immune regulation, lubrication, and matrix remodeling.

1.2.3 Rheumatic Arthritis

Rheumatoid arthritis (RA) is a severe systemic autoimmune disease predominantly described by inflammation of joints and the development of autoantibodies (McInnes and Schett, 2011; Smolen et al., 2018). In the context of RA, anti-IgG antibodies, known as rheumatoid factors, and antibodies against citrullinated peptides. Citrullinated peptide antibodies (CPAs) are used for diagnostic purposes in RA (McInnes and Schett, 2011;

Smolen et al., 2018). RA is one of the most widespread autoimmune diseases, with a prevalence of about 1% of the western population (McInnes and Schett, 2011; Smolen et al., 2018). Common risk factors for the pathogenesis of RA are genetic predisposition, gender, and environmental factors (McInnes and Schett, 2011; Smolen et al., 2018) (**Figure 4**). Alleles of the human leukocyte antigens (HLA) are known genetic predispositions. Specifically, alleles of the HLA-DR class II antigens have been associated with an increased risk of RA. There is also evidence that epigenetic factors can contribute to RA development (McInnes and Schett, 2011; Smolen et al., 2018).

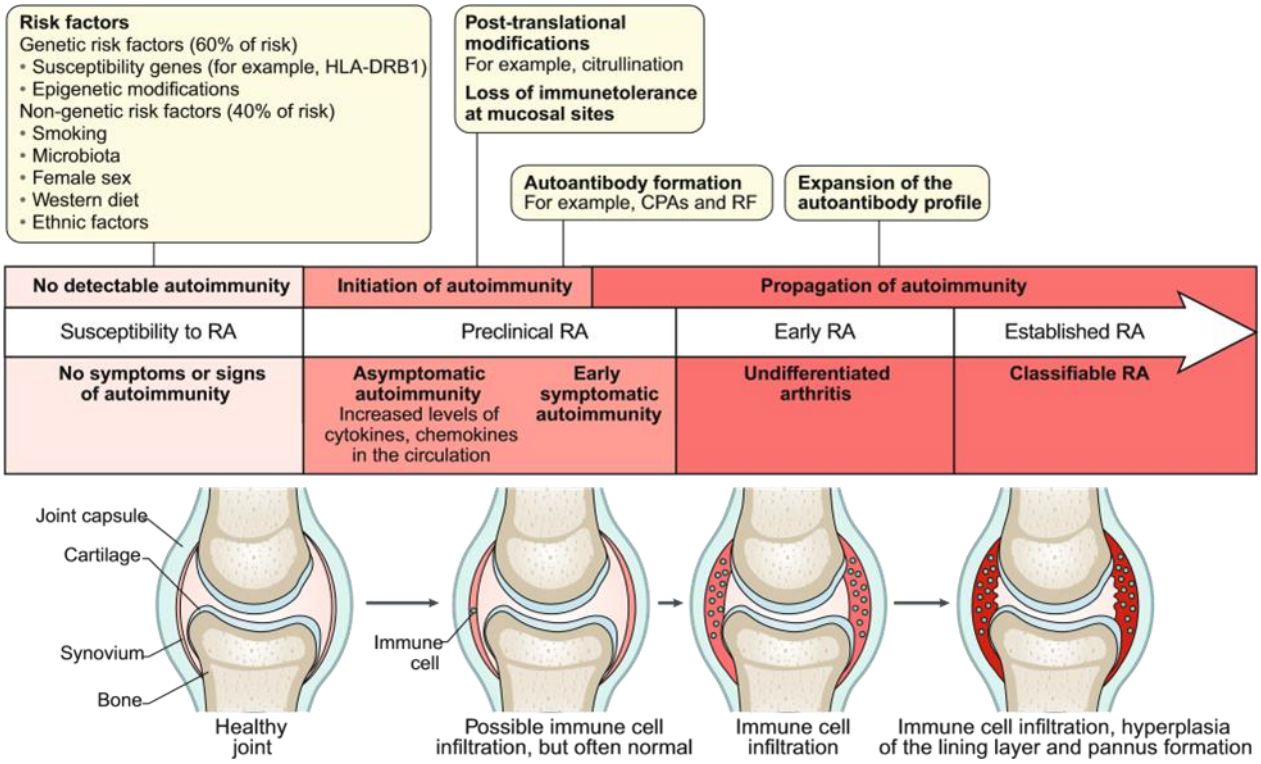

Figure 4. Risk factors and development of RA

Multiple risk factors contribute to rheumatoid arthritis (RA), and RA is likely to be triggered by genetic and non-genetic risk factors. Synovitis (inflammation of the synovium) and clinical symptoms develop years before autoimmunity begins against modified self-proteins. Citrullinated protein antibody (CPA); rheumatoid factor (RF) (Figure modified from Smolen et al., 2018).

Additionally, tobacco use and particulate matter inhalation are common risk factors for RA (McInnes and Schett, 2011; Smolen et al., 2018). RA also has a gender-specific prevalence. Women are two to three times more likely to develop RA than men. Women's immunomodulatory impact of estrogen is under debate, which could cause this gender difference (Smolen et al., 2018; Ngo et al., 2014). Microbiome-specific risks are also considered. Specifically, the microbiome of the intestinal tract is discussed as an essential component of the pathogenesis of RA (Smolen et al., 2018). The prevalence of rare bacterial species like actinobacteria in patients with RA is disproportionately higher than in individuals in the control group without RA, while usually abundant species decrease (Smolen et al., 2018; Chen et al., 2016b). Among the viral types, Eppstein-Barr is considered to be involved in RA pathogenesis (McInnes and Schett, 2011; Tan and Smolen, 2016).

There is only a partial understanding of the mechanisms that cause RA. Years before the first clinical rheumatic symptoms appear autoimmunity may develop in the patients (Smolen et al., 2018; Scherer et al., 2018). A combination of genetic exposure to various risk factors and a genetic background combined with persistent exposure to various risk factors led to the loss of self-tolerance and resulted in the formation of RA. The formation of CPAs is often used as a model scenario for the development of RA (Smolen et al., 2018). It has been suggested that inhalation of tobacco smoke or the presence of certain bacteria may increase the expression of peptidylarginine deiminase (Smolen et al., 2018). In mucosal stromal cells, peptidylarginine deiminase is involved in the cirullination of proteins of mucosal stromal cells. Professional APCs present to $CD4^+$ T cells with these neoantigens in the presence of altered citrullinated proteins. These lead to antibodies against self-antigens, including CPAs (Smolen et al., 2018). As well as citrullination, other post-translational modifications, such as nonenzymatic carbamylations are discussed as neoantigens which result in autoantibody production (Smolen et al., 2018). However, the inflammation of joints is not necessarily associated with the production of autoantibodies. In serum, CPAs and anti-carbamylated protein antibodies are detectable years before the clinical manifestation of RA (Smolen et al., 2018; Shi et al., 2014; Trouw et al., 2017). Inflammation appears to be triggered by immune complex formation and complement activation. Additionally, joint inflammation associated with RA is characterized by

increased vascular permeability, infiltration of immune cells into synovial tissue, hyperplasia of the synovial membrane, and pannus formation (McInnes and Schett, 2011; Smolen et al., 2018).

Chronic inflammation of the joints eventually leads to cartilage destruction and erosion of bone tissue over time. These destructive processes can lead to complete loss of joint function and go together with severe pain. Unfortunately, there is now no way to cure RA. However, symptom reduction can be achieved through immunosuppressive treatment and specific treatment strategies, such as the use of biopharmaceuticals, which target proinflammatory cytokines, receptor signaling pathways, or cells of the adaptive immune system (Smolen et al., 2018; Smolen et al., 2016; Kurowska-Stolarska and Alivernini, 2017). Although these specific therapeutics have revolutionized the treatment of RA, unfortunately, they are insufficiently effective in a substantial proportion of patients with RA (Kurowska-Stolarska and Alivernini, 2017; Nagy and van Vollenhoven, 2015).

It is crucial to understand the multifactorial pathogenesis of RA in cellular and molecular processes to develop new therapeutics and personalised medicine approaches.

1.2.4 Model systems for arthritis research

1.2.4.1 The arthritis model in general

Experimental arthritis models are crucial to Rheumatology research. One reason for this is that little is known about the pathogenesis of RA, which might occur months or even years before clinical symptoms of the disease. In addition, tissue for analysis (Synovial membrane) is usually obtained via operations. Surgical interventions such as joint replacement surgery or synovectomies are performed at advanced stages of RA. Therefore the availability of healthy or acutely inflamed tissue is rare. Although findings from animal experiments can only be applied to a limited extent to human arthritis, they nonetheless provide a better understanding of some aspects of human disease,

particularly understanding the initial steps in the pathogenesis of arthritis, and allow the use of novel therapeutics.

1.2.4.2 G6PI-induced arthritis model

G6PI is a protein with multiple functions. It is an essential cytosolic enzyme of the energy cycle, has glycolytic activity, and has additional functions as an extracellular signaling molecule. Known as autocrine motility and neural growth, G6PI is thought to play a role in autoimmunity and cancer (Bockermann et al., 2005). G6PI also plays a crucial role in the development of arthritis in mice. Studies have demonstrated that a bovine pancreas ribonuclease-specific T-cell receptor transgenic mouse crossed with NOD mice (the so-called K/BxN mouse) is prone to arthritis. It was conclusively demonstrated through a series of experiments that transgenic T-cell receptors recognized G6PI as part of MHC class II (Korganow et al., 1999; Matsumoto et al., 1999).
The Protocol published by Bockermann et al. describes an induction of acute self-limiting arthritis via an injection of G6PI at the tail's base in mice (Bockermann et al., 2005). This G6PI model was extended with an injection of anti-CD25 before immunization, leading to a depletion of Tregs and non-remitting, chronic, and destructive G6PI-induced arthritis (Frey et al., 2010). Experimental coverage of the various stages of arthritis is helpful and is utilized in this study.

1.3 ScRNA-seq in arthritis research

ScRNA-seq has emerged as a powerful tool for studying biological systems in which cellular heterogeneity is a prominent factor, such as complex tissues or the immune system. In the years since the first scRNA-seq study on mouse embryos was published in 2009 (Tang et al., 2009), this technique has fast enhanced resolution, throughput, and precision. As a result, it is possible to analyze thousands of single cells simultaneously with great depth and accuracy. Several scRNA-seq methods have been developed,

following a similar set of procedures, including single-cell isolation, cell lysis, reverse transcription, complementary deoxyribonucleic acid (cDNA) amplification, and library preparation. By labeling individual transcripts from each cell with barcodes, scRNA-seq can improve its accuracy and throughput (Klein et al., 2015; Macosko et al., 2015). However, all methods generate large and complex data sets that require specialized bioinformatics algorithms (Stegle et al., 2015). With the variety of scRNA-seq methods on offer and the differences in throughput and sensitivity, choosing the most appropriate platform for a study may be difficult. Platforms are usually selected based on the type of biological sample analyzed and the specific biological question which has to be answered. For example, the high throughput of the Seq-Well platform (Gierahn et al., 2017) and its portability makes this technology excellent options for profiling single cells in complex experimental settings. Therefore I decided to utilize the Seq-Well platform for the single-cell analysis of the G6PI-arthritis model.

ScRNA-seq studies have already been conducted to investigate the complexity of arthritis at a single-cell level. For example, a portable microfluidic control system performed scRNA-seq on synovial tissue samples in RA. Over 20,000 cells were analyzed, revealing the identity of the hematopoietic cells infiltrating the synovium and the presence of distinct subtypes of synovial fibroblasts (SFs) (Stephenson et al., 2018). In synovial tissue samples from patients with RA or osteoarthritis (OA), a scRNA-seq study could also identify transcriptomically distinct fibroblast subpopulations (Mizoguchi et al., 2018). The fibroblast subsets demonstrated distinct gene expression patterns, anatomical locations, and functional properties, such as invasive migration, osteoclastogenesis, and pro-inflammatory cytokine production. In addition, a high proportion of the $CD34^{+}$ $THY1^{+}$ subset was observed in the synovium of patients with RA compared to OA patients, and the presence of this subset in the synovium of RA patients was associated with a high level of immune cell infiltration, a high level of synovitis inflammatory score, and arthritic progression (Mizoguchi et al., 2018; Stephenson et al., 2018). A re-exposure rodent experiment further described this synovitis and the checkpoints between remission and persistence of the inflammatory fibroblasts (Friščić et al., 2021). Adaptive immunity did not play a role in tissue priming. SFs that were repeatedly stimulated showed elevated metabolic activity, which resulted in increased migration, invasion, and

osteoclastogenesis. These findings could be connected to human SF and showed that the intracellular tissue priming relies on the complement receptor activation and downstream mammalian target of rapamycin- and hypoxia-inducible factor 1α-mediated metabolic in SFs (Friščić et al., 2021). Also, another scRNA-seq study showed that SFs display positional identity under the control of endothelium-derived Notch signalling, thereby contributing to inflammation and pathology in inflammatory arthritis (Wei et al., 2020). Further, it was possible via fate-mapping approaches combined with light-sheet microscopy and scRNA-seq to identify CX_3CR1^+ tissue-resident macrophages. This specialized cell type forms an internal immunological barrier at the synovial lining and physically isolates the synovial cavity. These epithelial-like SLMs limit inflammation by protecting intra-articular structures with tight junctions (Culemann et al., 2019a). These studies have the potential to contribute to a better understanding of the underlying pathological mechanisms of arthritic diseases and improve patient treatment outcomes.

However, human SCO studies in arthritis research depend on joint replacement surgery or synovectomies. This dependency limits the availability of healthy or acutely inflamed tissue. Nevertheless, the pathogenesis might occur months or even years before the clinical intervention. These circumstances lead to an increasing knowledge gap in pathophysiological processes in healthy and acutely inflamed tissue. The combination of SCO and the G6PI-T-reg depletion model allows insights into these pathophysiological processes.

2 Aims of the thesis

In this thesis, SCO was used, specifically scRNA-seq, to describe dynamic biological processes in RtL-embryoids and pathophysiological processes in sparse cell types in the synovium with the G6PI T-reg depletion model.

Models that use cell culture to recapitulate embryogenesis or other critical developmental stages are gaining increasing interest in the scientific community, as they can be used to study mammalian embryogenesis *in vitro*. It has been previously demonstrated that three types of blastocyst-derived stem cells (ESCs, TSCs, and XEN cells) can be co-cultured in 3D cell culture environments to form early embryo-like structures (Sozen et al., 2018; Zhang et al., 2019b).

The aim was to develop an alternative method for generating stem-cell-based embryo models, using a transcription factor-mediated cellular reprogramming approach of genetically manipulated ESCs to give rise to induced trophoblast stem cell- (iTSC) or induced XEN- (iXEN) identities. This method eliminates the need for multiple individual stem cell cultures (ESC, TSC, and XEN cells) and complex cell culture reagents. Further, the aim was to apply scRNA-seq to reveal the dynamic biology of the resulting embryoid and compare the resulting dataset with their natural counterparts to assess their potential to mimic natural embryonic development.

RA is a chronic immune-mediated inflammation that is restricted to synovial joints. It is one of the most widespread autoimmune diseases, with a prevalence of about 1% of the western population (McInnes and Schett, 2011; Smolen et al., 2018).

The aim was to study the pathophysiological processes in homeostasis, acute- and chronic arthritis with the help of the G6PI-Treg depletion model (Frey et al., 2010). To achieve this, scRNA-seq was performed on the synovial microenvironment. To pursue a robust foundation for identifying gene signatures for tissue-resident synovial cells in acute and chronic inflammation. With a particular focus on SLMs and SFs. Both cell types provide the synovium's architectural and functional landscape in the healthy joint. Therefore, the results obtained from this study should be interpreted considering the specialized synovial tissue niches during inflammation to clarify the underlying mechanisms for this disease.

3 Material and Methods

3.1 Resource Tables

Table 1. Table of Antibodies

Antibodies	Source	Identifier
Goat polyclonal anti-CDX2	Santa Cruz	sc-19478
Goat polyclonal anti-GATA4	Santa Cruz	sc-1237
Goat-polyclonal anti-CD40	R&D Systems	AF440
Goat-polyclonal anti-LEFTY1	R&D Systems	AF746
Rabbit-polyclonal anti-p44/42 MAPK (Erk1/2)	Cell signaling	#9101
Mouse-polyclonal anti-OCT6	Absea	060204E04
Mouse-polyclonal anti-ESRRB	Perseus Proteomics	PP-H6705-00
Rabbit-polyclonal anti-NANOG	ReproCell	RCAB002P-F
Rabbit-polyclonal anti-EOMES	Abcam	ab23345
Goat-polyclonal anti-KLF4	R&D Systems	AF3158
Rat-polyclonal anti-PODXL	R&D Systems	MAB1556
Goat-polyclonal anti-OTX2	Abcam	AF1979
Rabbit-polyclonal anti-GATA3	Abcam	ab199428
Mouse-polyclonal anti-OCT4	Santa Cruz	sc-5279
Alexa Fluor 488-Phalloidin	Invitrogen	A12379
Alexa Fluor 594-Phalloidin	Invitrogen	A12381
Donkey polyclonal secondary antibody to Goat IgG-H&L (Alexa Fluor 594)	Abcam	ab150132
Chicken polyclonal secondary antibody to Goat IgG-H&L (Alexa Fluor 647)	Invitrogen	A-21469
Goat polyclonal secondary antibody to Rabbit IgG-H&L (Alexa Fluor 594)	Invitrogen	A-11012
Goat polyclonal secondary antibody to Rat IgG-H&L (Alexa Fluor 488)	Invitrogen	A-11006
Goat polyclonal secondary antibody to Mouse IgG-H&L (Alexa Fluor 488)	Invitrogen	A-11001
Donkey polyclonal secondary antibody to Mouse IgG-H&L (Alexa Fluor 594)	Invitrogen	A-21203
Chicken polyclonal secondary antibody to Rat IgG-H&L (Alexa Fluor 647)	Invitrogen	A-21472
Goat polyclonal secondary antibody to Rabbit IgG-H&L (Alexa Fluor 488)	Invitrogen	A-11008
Goat polyclonal anti-CDX2	Santa Cruz	sc-19478
Goat polyclonal anti-GATA4	Santa Cruz	sc-1237
Goat-polyclonal anti-PKCz	Santa Cruz	sc-216-G
Goat-polyclonal anti-CD40	R&D Systems	AF440

Goat-polyclonal anti-LEFTY1	R&D Systems	AF746
Rabbit-polyclonal anti-p44/42 MAPK (Erk1/2)	Cell signaling	#9101
Mouse-polyclonal anti-OCT6	Santa Cruz	060204E04
Mouse-polyclonal anti-ESRRB	Perseus Proteomics	PP-H6705-00
Mouse-polyclonal anti-OCT4	Santa Cruz	sc-5279
Rabbit-polyclonal anti-NANOG	ReproCell	RCAB002P-F
Rabbit-polyclonal anti-EOMES	Abcam	ab23345
Goat-polyclonal anti-KLF4	R&D Systems	AF3158
Alexa Fluor 488-Phalloidin	Invitrogen	A12379
Alexa Fluor 594-Phalloidin	Invitrogen	A12381
Rat-polyclonal anti-PODXL	R&D Systems	MAB1556
Goat-polyclonal anti-OTX2	R&D Systems	AF1979
Rabbit-polyclonal anti-GATA3	Abcam	ab199428

Table 2. Table of Oligonucleotides

Oligonucleotides	Source	Identifier
Tn5ME-B Oligo: 5`-GTCTCGTGGGCTCGGAGATGTGTATAAGAGACAG-3`	IDT	custom
Tn5MErev Oligo: 5`-[phos]CTGTCTCTTATACACATCT-3`	IDT	custom
TSO primer	IDT	custom
template-switching oligo	Eurogentec	custom
Smart PCR primer	Eurofins Scientific	custom
P5-Smart-PCR primer	IDT	custom
ISPCR primers	IDT	custom
barcoded primer	IDT	custom
N70X Oligo	Illumina	custom

Table 3. Table of Cell lines

Cell lines	Source	Identifier
Kermit ESCs	AG Schorle	N/A
KNUT1 ESCs	AG Schorle	N/A
5 Factor ESCs	AG Schorle	N/A
iGATA6 ESCs	AG Schorle	N/A
HEK 293T cell line	Dr. Michael Peitz ATCC	N/A

5 Factor_mCHerry and iGATA6_mCherry ESCs	AG Schorle	N/A

Table 4. Table of Commercial assays and kits

Commercial assays and kits	Source	Identifier
LIVE/DEAD Fixable Near-IR Dead Cell Stain	Invitrogen	#L34975
MinElute PCR Purification Kit	Qiagen	#28004
TapeStation HS D5000 Reagents	Agilent	#5067-5593
High Sensitivity D5000 ScreenTape	Agilent	#5067-5592
NEBNext High-Fidelity 2x PCR Master Mix	NEB	#M0541L
Nextera XT DNA Library Preparation Kit	Illumina	#FC-131-1096
2x Kapa Hifi HotStart Readymix	Kapa Biosystems	KK-2602
NextSeq® 500/550 High Output Kit v2.1	Illumina	#20030410
NextSeq PhiX Control Kit	Illumina	#FC-110-3002
NxGenTM RNase Inhibitor	Lucigen	#F83923-1
Exonuclease I	NEB	#M0293S
Maxima H Minus Reverse Transcriptase	Thermo Fisher	#EPO0753
AMPure XP beads	Beckman Coulter	#A63881
LifterSlip™	Electron Microscopy Science	#72186-60
Polycarbonate (PCTE) membrane filters	Sterlitech	PCT00162X22100
mRNA Capture beads	Chemgenes	MACOSKO-2011-10
SuperScript™ II Reverse Transkriptase	Thermo Fisher	18064071
Dow SYLGARD™ 184 Silicone Encapsulant Clear	Dow	184 SIL ELAST KIT

Table 5. Table of R packages

Software	Source	Identifier
biomaRt	(Durinck et al., 2005)	RRID: SCR_002987
limma	(Ritchie et al., 2015)	RRID: SCR_010943
scran	(Lun et al., 2016)	RRID: SCR_016944
GSEA	(Yu et al., 2012)	bioconductor.org/packages/release/bioc/html/clusterProfiler
AUCell	(Aibar et al., 2017)	bioconductor.org/packages/release/bioc/html/AUCell
Seurat	(Butler et al., 2018)	RRID: SCR_007322
pheatmap	author: Raivo Kolde	RRID: SCR_016418
ggraph	author: Thomas Lin Pedersen	cran.rproject.org/web/packages/ggraph
ggplot2	(Wickham, 2016)	RRID: SCR_014601

RStudio	RStudio, Inc.	RRID: SCR_000432
nichenetr	(Browaeys et al., 2020)	github.com/saeyslab/nichenetr
FlowJo	Tree Star Inc.	RRID: SCR_008520
FACS DIVA	BD Biosciences	version 8.0.1
ImageJ	(Schneider et al., 2012)	RRID: SCR_003070
iRegulon	(Janky et al., 2014)	http://iregulon.aertslab.org/
Cytoscape	(Shannon et al., 2003)	RRID:SCR_003032 (version v3.7.1)
FASTQC	(Simon Andrews et al., 2010)	(version 0.11.7)
bcl2fastq2	Illumina	RRID: SCR_015058
STAR	(Dobin et al., 2013)	RRID: SCR_015899
Kallisto	(Bray et al., 2016)	version 0.2.1
tximport	(Soneson et al., 2015)	bioconductor.org/packages/release/bioc/html/tximport

Table 6. Table of Chemicals

Chemicals	Source	Identifier
Acetic acid	ProLabo	20104298
Aceton	Roth	T161.1
Agarose	Sigma	A9539
3-aminopropyltriethoxysilane	Sigma	A3648-100ml
Betaine	Sigma	B0300
β-Mercaptoethanol	Sigma	63689-100mL-F
Bovine serum albumin	Sigma	A9418-100G
Chitosan	Sigma	C3646-100G
DMEM	Thermo Fisher Scientific	11960069
DMEM + GlutaMAX	Gibco	31966-021
dNTP	NEB	#N04465
Dimethylformamid	Sigma	227056-1L
Doxycycline	Sigma	D9891
Ethylenediaminetetraacetic acid	Sigma	03690-100ML
Essential amino acids	Gibco	11130-036
2i CHIR-99021	Cayman Chemical	13122
FCS	Gibco	10270-106
FGF4	Reliatech	100-017 L
Ficoll PM-400	Sigma	F5415-50ml

Formalin	Sigma	100496
Guanidine Hydrochloride	Sigma	G3272
Guanidine Thiocyanate	AmBion	AM9422
Heparin	Sigma	H3149-10KU
Hoechst 33342 Stain Solution	Invitrogen	H1399
L-glutamine	Gibco	25030-024
Leukemia inhibitory factor	Sigma	ESG1107
$MgCl_2$	Sigma	63069-100ML
NaCl	Sigma	S6546-4L
NaCO3	Sigma	223530-500G
Nuclease free H_2O	Invitrogen	10977-035
Nonessential amino acids	Gibco	11140-035
Polybrene	Sigma	TR-1003
PBS	Thermo Fisher	10010023
Mirdametinib	BioGems	3911091
3D-Activated Amino (PDITC)	Sigma	258555-5g
Penicillin/ Streptomycin	Gibco	15140-122
Poly glutamic acid	Sigma	P4761-100MG
Pyridine	SIgma	270970-1l
Recombinant RNase Inhibitor	Takara	2313 A
Rnase Inhibitor	Lucigen	F83923-1
RPMI 1640	Thermo Fisher Scientific	11875- 093
Roti®-Mount FluorCare DAPI	Roth	HP20.1
Sarosyl	Sigma	L-7414
Sodium dodecyl sulfate (SDS)	life technologies	15553-035
Silicone Elastomer	DowCorning	184 SIL ELAST KIT 0.5 PG
Sodium pyruvate	Thermo Fisher Scientific	11360070
StemPro Accutase Cell Dissociation Reagent	Gibco	A1110501
Sylgard	DowCorning	184 SIL ELAST KIT 0.5 PG
Tris-HCL pH8	Thermo Fisher	15568025
Triton X-100	AppliChem	A4975
TrypLE express	Gibco	12604-013
Tween-20	AppliChem	A44974

Table 7. Table of Consumables

Other	Source	Identifier
10 ml syringe	Braun	4606108V
4-well dishes	Thermo Fisher	267061
Cell Culture Dishes	Greiner Bio-One	627861
40 µm cell strainer	BD	8720373563798
Glass slide	Corning	2947-75x25
Lifter slip	Electron Microscopy Science	72186-60
MicroTissues® 3D Petri Dish®	Sigma–Aldrich	Z764094-6EA
Polycarbonate membrane	Sterlitech	PCT00162X22100
Razor blades	AmericanLine	66403

3.2 Methods for the generation and analysis of RtL-embryoids

3.2.1 Generation of ES cell lines

Kermit ESCs were generated from blastocysts of Oct3/4_GFP transgenic mice (Yoshimizu et al., 1999; Kaiser et al., 2020) by using standard ES derivation protocols (Peitz et al., 2007). The Schorle Laboratory also derived the ES cell line KNUT1. Cdx2, Tfap2c, Eomes, Gata3, and Ets2 ESCs (5 Factor / 5F-ESCs) were previously generated and characterized by the Schorle Laboratory (Kaiser et al., 2020). An iXEN cell line was created by lentiviral transduction of ESCs using the pCW57.1_Gata6 plasmid, a gift from Constance Ciaudo (Addgene plasmid #73537; [http://n2t.net/addgene:73537]). In addition, lentiviral particles were produced in 293 T HEK cells (ATCC order number #CRL-3216; Human embryonic kidney cells, harboring an SV40 large T antigen; Cell line received from Dr. Michael Peitz) by co-transfection of the lentiviral pCW57.1_Gata6 plasmid with VSV-G (pMD2.G, Addgene #12259) and helper plasmid (psPAX2, Addgene #12260) by calcium-phosphate precipitation. The virus-containing supernatant was harvested 48 h and 72 h after transfection, pooled and filtered through 0.4 µm SFCA membranes, and stored at −80°C. A wild-type ESC line established by the Schorle Laboratory was cultured under standard ESC conditions with feeders until reaching ~60%

confluency. At this point, viral transductions were performed overnight in a six-well dish using 800 µL of standard ESC medium with 200 µL virus-containing supernatant supplemented with 8 µg/mL polybrene (Sigma–Aldrich). Positive clones were selected by supplementing the culture medium with 1 µg/mL puromycin for three days. All lentiviral protocols were performed under S2 conditions. Jan Langkabel (AG Schorle- Department of Developmental Pathology; University of Bonn) performed all Steam cell line experiments. (3.2.1 is modified from Langkabel and Horne et al. 2021).

3.2.2 Cell culture of ES cell lines

ES cells were cultured on gelatin-coated plates in ES cell medium consisting of DMEM + GlutaMAX (Gibco) supplemented with 2 mM L-glutamine (Gibco), 50 U/mL penicillin/streptomycin (Gibco), 1× nonessential amino acids (Gibco), 1× essential amino acids (Gibco), 0.1 mM β-Mercaptoethanol (Gibco), 15% fetal calf serum (FCS) (Gibco), LIF (1000 U/mL; Sigma–Aldrich), and 2i (3 µM CHIR-99021, Cayman Chemical; 1 µM PD0325901, BioGems). Induced TS cells reprogrammed from 5 Factor ESCs were cultured in TSC Medium consisting of advanced RPMI 1640 (Thermo Fisher Scientific), 20% FCS, 2 mM L-glutamine, 1 mM sodium pyruvate (Thermo Fisher Scientific), 50 U/mL penicillin/streptomycin, and 0.1 mM β-Mercaptoethanol. A mixture consisting of 70% feeder-MEF conditioned TSC medium and 30% fresh, unconditioned TSC medium was prepared and supplemented with FGF4 (Reliatech; 25 ng/mL), Heparin (Sigma–Aldrich; 1 µg/mL) for the culture of iTSCs. iXEN cells reprogrammed from iGATA6 ESCs were cultured on gelatin-coated culture dishes in XEN cell culture medium consisting of RPMI 1640, 15% FCS, 2 mM L-glutamine, and 50 U/mL penicillin/streptomycin. Jan Langkabel (AG Schorle- Department of Developmental Pathology; University of Bonn) performed the cell culture of ES cell lines. (3.2.2 is modified from Langkabel and Horne et al. 2021).

3.2.3 3D cell culture and generation of RtL-embryoids

3D cell culture dishes were generated using the MicroTissues® 3D Petri Dish® micro-mold spheroids (Sigma–Aldrich) according to the manufacturer's protocol with 2% molten cell culture grade Agarose (Sigma–Aldrich; in sterile saline (0.9% w/v NaCl)). 3D Petri Dish®, holding 256 microwells, were equilibrated in reconstructed embryo medium (Zhang et al., 2019b) for 1 h at room temperature in a 12-well plate. The reconstructed embryo medium consisted of 39% advanced RPMI 1640 and 39% DMEM (Thermo Fisher Scientific) supplemented with 17.5% FCS, 2 mM L-glutamine, 0.1 mM β-Mercaptoethanol, 0.1 mM MEM nonessential amino acids, 1 mM sodium pyruvate, 1% penicillin-streptomycin (Zhang et al., 2019b). Before seeding, each of the three ESC lines used to generate RtL-embryoids was diluted to cell counts resulting in an average-based seeding of 6 Kermit ESCs (or KNUT1 ESCs), 16 5-Factor ESCs and 5 iGATA6 ESCs per microwell of the 3D Petri Dish®. The diluted ESC populations were then pooled, centrifuged, and resuspended in an ES cell medium before seeding on the 3D Petri Dish®. Cells were cultured with ES cell medium without doxycycline (DOX) for 24 h to allow the cells to form EBs before switching the culture medium to a reconstructed embryo medium supplemented with 2 µg/mL DOX (Sigma–Aldrich). Aggregates were cultured under this condition for 3 days, inducing transgene expression and reprograming into iTSCs or iXEN cells, leading to self-organization into RtL-embryoids. Generated structures were harvested from their 3D Petri Dish® by placing the agarose pad upside-down into a new 12-well plate filled with 2 mL phosphate-buffered saline (PBS) and centrifugation at 45 × g for 3 min, forcing the aggregates out of their microwells. (3.2.3 is modified from Langkabel and Horne et al. 2021).

3.2.4 Quantification of correctly compartmented RtL-embryoids.

To quantify compartmentalization of the structures, Kermit ESC, 5-Factor ESCs, and iGATA6_mCherry ESCs were used for seeding the starting cell populations in average ratios per microwell, as previously introduced. Quantification of compartmented structures

was performed in three independent experiments, assessing a total of 1167 aggregates (day 4) and 778 aggregates (day 5). Structures were regarded as correctly compartmented if they exhibited the formation of clearly separated Epi- and ExE-like compartments surrounded by a complete monolayer of VE-like tissue (**Figure 6C**). Structures comprised of all three cell lineages which failed to completely segregate into an Epi- or ExE-like compartment or displayed an incomplete VE-like tissue were regarded as incorrectly compartmented (**Figure 8F, G**). Jan Langkabel (AG Schorle- Department of Developmental Pathology; University of Bonn) performed the generation of RtL-embryoids. (3.2.3 is modified from Langkabel and Horne et al. 2021).

3.2.5 Derivation of stem cells from RtL-embryoids

ESC-like and ExE-like stem cells were derived from RtL-embryoids by outgrowth culture performed in 2i/LIF supplemented ESC medium or FGF4/Heparin supplemented TSC medium, respectively. Therefore, RtL-embryoids were generated as described before and seeded onto gelatin-coated cell culture plates in either ES or TS medium, where they were allowed to settle and attach. Next, aggregates were cultured in these conditions until cellular outgrowth formed, at which point the cells were dissociated by incubation in TrypLE express (Gibco) and passaged onto a new, gelatin-coated culture plate. Once colonies had formed, they were picked and cultured in individual mono-cultures before characterization by immunofluorescence (IF) staining for ES and TS markers. Jan Langkabel (AG Schorle- Department of Developmental Pathology; University of Bonn) performed the derivation of stem cells. (3.2.5 is modified from Langkabel and Horne et al. 2021).

3.2.6 IF staining of stem cells derived from RtL-embryoids

For IF staining, cells were washed twice with PBS, fixed for 10 min with 4% formalin (Sigma–Aldrich), washed twice, and permeabilized with Triton X-100 ((AppliChem); 0.5% in PBS). Blocking was performed in blocking solution (2% BSA (Sigma–Aldrich), 0.1%

Triton X-100 (AppliChem) in PBS) for 1 h at room temperature. Incubation with the primary antibody was performed in blocking buffer o/n at 4°C. Cells were washed three times with PBS before incubation with secondary antibody in blocking buffer for 2 h at room temperature and protected from light. Cells were washed three times with PBS and kept protected from light before imaging. The nuclei were stained for 10 min in PBS using Hoechst33342 (Invitrogen; 1 µg/mL).

Primary antibodies used and dilutions: Goat-polyclonal anti-CDX2 (Santa Cruz; 1:200), Rabbit polyclonal anti-EOMES (Abcam; 1:400), Mouse-polyclonal anti-OCT4 (Santa Cruz; 1:300), Rabbit-polyclonal anti-NANOG (ReproCell; 1:300). Secondary antibodies used and dilutions: Donkey polyclonal secondary antibody to Goat IgG-H&L Alexa Fluor 594 (Abcam; 1:500), Goat-polyclonal secondary antibody to Rabbit IgG-H&L Alexa Fluor 594 (Invitrogen; 1:500), Donkey polyclonal secondary antibody to Mouse IgGH& L (Alexa Fluor 594) (Invitrogen; 1:500). Jan Langkabel (AG Schorle- Department of Developmental Pathology; University of Bonn) performed the derivation IF staining of stem cells. (3.2.6 is modified from Langkabel and Horne et al. 2021).

3.2.7 Imaging and image processing

Confocal images of RtL-embryoids were acquired using a VisiScope spinning disk confocal microscope (Visitron) with a ×20, ×40, or ×63 objective. Images in **Figure 6** A-C were acquired using an inverted DM IRB (Leica) microscope with a ×10 objective. The images were processed and merged using the open-source image processing package Fiji (version 1.53c). Jan Langkabel (AG Schorle- Department of Developmental Pathology; University of Bonn) performed imaging and image processing. (3.2.7 is modified from Langkabel and Horne et al. 2021).

3.2.8 5 Factor ESCs reprogramming in 2D culture

5-Factor ESCs were seeded onto gelatin-coated cell culture dishes in ES-medium and cultured at 37°C and 7.5% CO_2 until small colonies had formed. Transgene induction and

reprogramming were initiated by changing the cell culture medium to TS medium, consisting of 70% feeder-MEF conditioned TS medium and 30% freshly prepared TS medium, supplemented with FGF4 (25 ng/mL), Heparin (1 µg/mL), and DOX (2 µg/mL). Cells were cultured under these conditions for 3 days before omitting DOX from the culture medium, stopping transgene expression. The culture medium was replaced with fresh culture medium every 48 h. For fluorescence-activated cell sorting (FACS) and subsequent scRNA-Seq analysis, cells were cultured for another 24 h without DOX supplementation before harvesting by washing with PBS and incubation in StemPro Accutase Cell Dissociation Reagent (Gibco). Once cells had dissociated, the reaction was stopped by adding a TS culture medium to the cells. The single-cell suspension was pelleted by centrifugation and washed twice with PBS before staining for CD40. Staining for CD40 (Goat-polyclonal anti-CD40; R&D Systems) was performed in FACS buffer (2% FCS in PBS; Dilution: 1:300) for 30 min on ice. Cells were washed three times with FACS buffer, resuspended in FACS buffer with secondary antibody (Chicken anti-Goat IgG (H + L) Cross-Absorbed Secondary Antibody, Alexa Fluor 647; Invitrogen; Dilution: 1:300) and incubated for 30 min on ice in the dark. Cells were washed three times with FACS buffer and kept in the dark until sorting. Jan Langkabel (AG Schorle- Department of Developmental Pathology; University of Bonn) performed the Cellular reprogramming of 5 Factor ESCs in a 2 dimensional (2D) mono-culture. (3.2.8 is modified from Langkabel and Horne et al. 2021).

3.2.9 iGATA6 ESC reprogramming in 2D mono-culture

To analyze iGATA6 ESC reprogramming in 2D mono-cultured, iGATA6_mCherry ESCs were seeded onto gelatin-coated cell culture dishes in ES-medium and cultured at 37°C and 7.5% CO_2 until small colonies had formed. Transgene induction and reprogramming were initiated by changing the cell culture medium to a XEN cell culture medium supplemented with 2 µg/mL DOX. Cells were cultured under these conditions for 3 days before omitting DOX from the culture medium, stopping transgene expression. The culture medium was replaced with fresh culture medium every 48 h. For FACS and subsequent

scRNA-Seq analysis, cells were cultured for another 24 h without DOX supplementation before harvesting by washing with PBS and incubation in StemPro Accutase Cell Dissociation Reagent (Gibco). Once cells had dissociated, the reaction was stopped by adding a XEN cell culture medium to the cells. iXEN cells derived from iGATA6_mCherry were not stained before sorting by FACS, as mCherry expression was used as the fluorescent marker for sorting. Cells were pelleted by centrifugation, resuspended in FACS buffer, and kept on ice until sorting. Jan Langkabel (AG Schorle- Department of Developmental Pathology; University of Bonn) performed cellular reprogramming of iGATA6 ESCs in 2D mono-culture. (3.2.9 is modified from Langkabel and Horne et al. 2021).

3.2.10 FACS sorting of cells from RtL-embryoids and 2D mono-culture reprogramming

FACS was used to separate cells of each embryo-like compartment for subsequent transcriptional profiling by scRNA-Seq. Therefore, RtL-embryoids were built from Kermit ESCs, 5-Factor ESCs, and a mCherry-transduced iGATA6 ESC line in described ratios. A total of more than 600 correctly assembled RtL-embryoids were handpicked after reprogramming and depletion from DOX. This was followed by pooling and dissociation into a single-cell suspension by incubation for 15 min in StemPro Accutase Cell Dissociation Reagent. After passing through a 40 µm cell strainer (Becton Dickinson), cells were stained against CD40 (Goat-polyclonal anti-CD40; R&D Systems), a surface protein expressed on cells of ExE-identity, allowing for FACS of either Green Fluorescent Protein (GFP), mCherry, or Alexa-647 for isolation of Kermit ESCs, iXEN cells or iTSCs, respectively. Staining for CD40 was performed in FACS buffer (2% FCS in PBS; Dilution: 1:300) for 30 min on ice. Then, cells were washed three times with FACS buffer, resuspended in FACS buffer with secondary antibody (Chicken anti-Goat IgG (H + L) Cross-Absorbed Secondary Antibody, Alexa Fluor 647; Invitrogen; Dilution: 1:300), and incubated for 30 min on ice in the dark. Cells were washed three times with FACS buffer and kept in the dark until sorting. According to the manufacturer's protocol, live/dead staining was performed using the Fixable Near-IR Dead Cell-Cell Stain Kit (Invitrogen;

L34975) by incubation for 15 min at RT. Flow cytometry and sorting were performed using FACS DIVA (version 8.0.1) on BD Aria III (BD Bioscience Pharmingen). For cells obtained from reprogramming in 2D mono-culture, the identical FACS setup was used like for the RtL-embryoids. (3.2.10 is modified from Langkabel and Horne et al. 2021).

3.2.11 Library preparation and sequencing using Smart-Seq2

Our new index-sorted single-cell transcriptome dataset was based on the Smart-Seq2 protocol (Picelli et al., 2013). Cells were FACS sorted into eight 384-well plates containing 2.3 µL lysis buffer (Guanidine Hydrochloride (50 mM; Sigma–Aldrich), dNTPs (17.4 mM; NEB), Smart dT30VN primer (2.2 µM; IDT) retaining protein expression information for every well to subsequently match with the respective single-cell transcriptomic data in an index sorting approach. Plates were sealed and stored at −80°C until further processing. Smart-Seq2 libraries were generated on a Tecan Freedom EVO and Nanodrop II (BioNex) system, as previously described (Picelli et al., 2013). In short, lysed cells were incubated at 95°C for 3 min. 2.7 µL RT mix containing SuperScript II buffer (Invitrogen), 9.3 mM DTT, 370 mM Betaine (Sigma–Aldrich), 15 mM $MgCl_2$ (Sigma–Aldrich), 9.3 U SuperScript II RT (Invitrogen), 1.85 U recombinant RNase Inhibitor (Takara), and 1.85 µM template-switching oligo (Eurogentec) was aliquoted to each lysed cell using a Nanodrop II liquid handling system (BioNex) and incubeding at 42°C for 90 min and 70°C for 15 min. A 7.5 µL preamplification mix containing KAPA HiFi HotStart ReadyMix (KAPA) and 2 µM ISPCR primers (IDT) were added to each well, and full-length cDNA was amplified for 16 cycles. cDNA was purified with 1× Agencourt AMPure XP beads (Beckman Coulter) and eluted in 14 µL nuclease-free water (Invitrogen). Concentration and cDNA size was checked for select representative wells using a High Sensitivity DNA5000 assay for the Tapestation 4200 (Agilent). cDNA was diluted to an average of 200 pg/µL, and 100 pg cDNA from each cell was tagmented by adding 1 µL TD and 0.5 µL ATM from a Nextera XT DNA Library Preparation Kit (Illumina) to 0.5 µL diluted cDNA in each well of a fresh 384-well plate. The tagmentation reaction was incubated at 55°C for 8 min before removing the Tn5 from the DNA by adding 0.5 µL NT buffer per well. In

addition, 1 µL well-specific indexing primer mix from Nextera XT Index Kit v2 Sets A-D and 1.5 µL NPM was added to each well, and the tagmented cDNA was amplified for 14 cycles according to the manufacturer's specifications. According to the manufacturer's protocol, PCR products from all wells were pooled and purified with 1× Agencourt AMPure XP beads (Beckman Coulter). The fragment size distribution was determined using a High Sensitivity DNA5000 assay for the Tapestation 4200 (Agilent), and library concentration was determined using a Qubit double-stranded DNA (dsDNA) HS assay (Thermo Fischer). Libraries were clustered at 1.4 pM concentration using High Output v2 chemistry and sequenced on a NextSeq500 system SR 75 bp with 2*8 bp index reads. Single-cell data were demultiplexed using bcl2fastq2 v2.20. (3.2.11 is modified from Langkabel and Horne et al. 2021).

3.2.12 ScRNA-Seq raw data processing

Following sequencing by the Smart- Seq2 method (Picelli et al., 2013), RNA-Seq libraries were subjected to initial quality control using FASTQC (version 0.11.7) implemented in a scRNA pre-processing pipeline (docker image and scripts available at [https://hub.docker.com/r/pwlb/rna-seqpipeline-base/] (version 0.1.1); [https://bitbucket.org/limes_bonn/bulk-rna-kallistoqc/src/master/] (version 0.2.1)). Raw reads were pseudoaligned to the mouse transcriptome (GRCm38, Gencode vM16 primary assembly) using Kallisto with default settings (version 0.44.0) (Bray et al., 2016). Based on the pseudo alignment estimated by Kallisto, transcript levels were quantified as transcripts per million reads (TPM). TPM counts were filtered for mitochondrial-, pseudo- and ribosomal genes before being imported into R using tximport (version 1.16.1) (Soneson et al., 2015), and transcript information was summarized at the gene level. The resulting dataset of 29,960 features across 1931 samples were analysis using the R package Seurat (version 3.1.2) (Butler et al., 2018). (3.2.12 is modified from Langkabel and Horne et al. 2021).

3.2.13 Data quality control

Cells with less than 2500 expressed genes, and less than 500,000 aligned sequencing reads were excluded from the further analysis. After filtering, the 3D co-culture dataset contained 29,960 features across 961 samples. The 3D co-culture and 2D culture combined dataset contained the same feature number across 1385 samples. 'LogNormalization' (Seurat version 3.1.2) was applied before downstream analysis. Next, the original gene counts for each cell were normalized by total transcript counts, multiplied by 10,000 (TP10K), and then log-transformed by log10 (TP10k + 1). Next, the genes with the highest cell-to-cell variability in the dataset were determined by calculating the top 2000 most variable genes by selecting the 'vst' method of the 'FindVariableFeatures' function in Seurat (Seurat version 3.1.2). After scaling, the dimensionality of the 3D co-culture data was reduced to 10 principal components (PCs) and the 3D co-culture and 2D mono-culture combined dataset was reduced to 4 PCs used as input for uniform manifold approximation and projection (UMAP) representation. (3.2.18 is modified from Langkabel and Horne et al. 2021).

3.2.14 Clustering and cluster annotation

The Seurat (version 3.1.2) SNN-graph-based Louvain clustering of the 3D co-culture dataset was performed using a resolution of 0.2. Clusters were annotated by comparing cluster marker genes with public resources. In addition, 2D culture clusters were annotated via culture origin. (3.2.14 is modified from Langkabel and Horne et al. 2021).

3.2.15 Differential expression tests and cluster marker genes

Differential expression tests were performed using FindMarkers/FindAllMarkers functions in Seurat (version 3.1.2) with default two-sided non-parametric Wilcoxon Rank Sum test with Bonferroni correction using all genes in the dataset. Cluster marker genes with >1.5 log-fold changes were regarded as significant differentially expressed genes (DEGs).

Cluster marker genes were identified by applying the differential expression tests for upregulated genes between cells in one cluster to all other clusters in the dataset. Top-ranked genes (p-values) from each cluster of interest were extracted for further illustration. All other function arguments were set to default. The differential expression tests were used between 3D co-culture and 2D mono-culture equivalents default settings. (3.2.15 is modified from Langkabel and Horne et al. 2021).

3.2.16 Subset analysis of the VE-like, Epi-like, and ExE-like cells

The VE-like, Epi-like, and ExE-like cell space was examined by subsetting the 3D co-culture dataset. First, the Variable gene selection was repeated (top 2000 variable genes), and VE-like, Epi-like, and ExE-like cells were scaled with Seurat's ScaleData function (version 3.1.2). The dimensionality of the VE-like-cell data was then reduced to 7 PCs, Epi-like cells data to 4 PCs, and ExE-like-cell data to 10 PCs. These reductions served as input for the UMAP calculations. Finally, the SNN-graph-based Louvain clustering of the cells was performed using a resolution of 0.2 for the VE like- cell space, 0.3 for the Epi-like-cell space, and 0.1 for the ExE-like-cell space. (3.2.16 is modified from Langkabel and Horne et al. 2021).

3.2.17 Signature enrichment analysis

A gene signature enrichment analysis using the ‘AUCell’ method (Aibar et al., 2017), implemented in the package (version 1.10.1) in R, was applied to link observed Stem cell clusters to existing studies. The resulting area under the curve (AUC) values were normalized to the maximum possible AUC and subsequently visualized in violin plots. (3.2.17 is modified from Langkabel and Horne et al. 2021).

3.2.18 Integration of the reference datasets

The collection of reference datasets published in Posfai et al., 2021 was kindly supplied as a Seurat object by Ester Posfai. The received object was updated for analysis in R (version 4.0.3) with Seurat (version 4.0.1). The object was subsetted for cells of datasets generated by Chen et al., Mohammed et al., Posfai et al., and Pijuan-Sala et al. (Chen et al., 2016a; Mohammed et al., 2017; Posfai et al., 2017; Pijuan-Sala et al., 2019). The integrated Seurat object was split into the respective datasets. Normalization and variable feature selection were performed independently, as depicted above. Variable features were identified across the datasets applying the function 'SelectIntegrationFeatures'. Scaling and PCA were performed based on these features for each dataset. Integration anchors were identified using 'FindIntegrationAnchors' using 'rpca' reduction and setting 'k.anchor' = 20. The integration was performed with the 'IntegrateData' function by setting 'k.weight' = 45. The integrated data were scaled, and dimensionality reduction by PCA and UMAP was performed. (3.2.18 is modified from Langkabel and Horne et al. 2021).

3.2.19 Label transfer between reference- and the RtL-embryoids dataset

The RtL-embryoid dataset was updated for analysis in Seurat (version 4.0.1.) The 'FindTransferAnchors' function was used to determine anchors between our dataset and the integrated reference datasets. The 'MapQuery' function was used to map our dataset onto the UMAP of the reference dataset. Since non-perfectly intersecting cell identities were expected between the RtL-embryoid dataset and the reference datasets, a 'de-novo visualization' by merging the PCA embeddings of the two datasets and calculating a new UMAP was performed. (3.2.19 is modified from Langkabel and Horne et al. 2021).

3.2.20 Confusion matrix

For visualization of the results of the Label Transfer described above, the percentage of cells from the RtL-embryoid dataset mapped to the respective cells in the reference

dataset was calculated and visualized using pheatmap (version 1.0.12). (3.2.20 is modified from Langkabel and Horne et al. 2021).

3.2.21 Gene Ontology Enrichment Analysis of DEGs in RtL-embryoids

The FindAllMarkers function from the Seurat package used the Wilcoxon Rank Sum test to identify significant DEGs between each cluster. The top 100 DEG sorted by adjusted p-value were used for the Gene Ontology Enrichment Analysis (GOEA). The R package/ClusterProfiler was utilized for the analysis (version 3.14.3) (Yu et al., 2012). (**Fehler! Verweisquelle konnte nicht gefunden werden.** is modified from Langkabel and H orne et al. 2021).

3.2.22 Transcription factor enrichment analysis

The FindAllMarkers function from the Seurat package used the Wilcoxon Rank Sum test to identify significant DEGs between each cluster. All upregulated DEGs were analyzed by Enrichr ChIP enrichment analysis (ChEA16) [http://amp.pharm.mssm.edu/Enrichr/] to determine the TFs that could control the expression of these genes (Chen et al., 2013; Lachmann et al., 2010). (3.2.22 is modified from Langkabel and Horne et al. 2021).

3.2.23 NicheNet analysis

The NicheNet approach predicts which ligands formed by one cell type regulate the expression of target genes in another cell type. Ligand- target links are inferred by RNA expression data of interacting cells with current knowledge on signaling and gene regulatory networks. NicheNet can address the question of which ligands produced by a sender cell are the most active in impacting gene expression in the receiver cell (i.e., ligand activity analysis) (Browaeys et al., 2020). To achieve this, NicheNet assesses how

well these ligands predict the examined changes in gene expression and ranks them accordingly. After ligand ranking, NicheNet infers active ligand-target connections by looking for genes that are impacted in the receiving cell type and have a high possibility of being regulated by the prioritized ligands (Browaeys et al., 2020). (3.2.23 is modified from Langkabel and Horne et al. 2021).

3.2.24 NicheNet Intercellular communication analysis.

For the NicheNet analysis (version 1.0.0) (Browaeys et al., 2020), a ligand activity analysis was performed for every cell type separately (VE-like, Epi-like, and ExE-like cells). All genes that were expressed in >10% of the individual sender cell type and matched at least one receptor from the differentially expressed genes in the receiver cells were accepted as potential ligands. All non-differentially expressed genes were considered as background. The top 6 genes based on the Pearson correlation coefficient were selected for all three cell types for ligand prioritization. To make the activity scores in all three settings comparable to overall ligands, z-score normalization of the Pearson correlation coefficients was performed after combining all ligands for the different cell types. For those ligands, the corresponding receptors are indicated in the ligand-receptor heatmap. The indicated score is assigned to the weight of the interaction between the ligand and receptor in the integrated weighted ligand signaling network. The ligand-target heatmap shows potential regulatory scores for interactions between the 6 top-ranked ligands and 100 top target genes for each cell type. (3.2.24 is modified from Langkabel and Horne et al. 2021).

3.2.25 Data visualization

The R packages Seurat, and ggplot2 (version 3.3.2) (Wickham, 2016) were used to generate figures. GraphPad Prism was used to visualize bar plots and quantitative data (version 8.0.2). Schematics were generated using Powerpoint (version 2110). Finally, flow

cytometry data were visualized using FlowJo (version 10.6.1). (3.2.25 is modified from Langkabel and Horne et al. 2021).

3.2.26 Data and code availability

Raw sequencing data generated in this study have been deposited in the Gene Expression Omnibus (GEO) database under accession code GSE188394. Additionally, data are deposited via FASTGenomics [https://beta.fastgenomics.org/d/200474]. The FASTGenomics platform also provides Seurat objects of the datasets generated in this study. The publicly available datasets analyzed during the current study are from the GEO- and ArrayExpress repositories. GSE84892 (Posfai et al., 2017) GSE74155 (Chen et al., 2016a) GSE100597 (Mohammed et al., 2017) E-MTAB-6967 (Pijuan-Sala et al., 2019). The mouse genome used for kallisto alignment is available from the GENCODE Project. GRCm38, Gencode vM16 primary assembly. All the computational analyses were performed using R programming languages. Scripts of critical steps can be found at [http://github.com/schultzelab/Rosette-to-Lumen-stageembryoids]. Additionally, our code to reproduce the analysis can be accessed via FASTGenomics https://beta.fastgenomics.org/analyses/detail-analysis-9301d957888c40538020f90428bcc763#Result&analysis. (3.2.26 is modified from Langkabel and Horne et al. 2021).

3.3 Methods for the generation and analysis of the G6PI-induced arthritis dataset

3.3.1 Animals and the induction of arthritis

A specific pathogen-free facility was used for breeding and maintaining DBA/1 mice. The appropriate authorities approved the experiments, and they were conducted in compliance with state and institutional guidelines. The recombinant human G6PI was prepared as described previously (Schubert et al., 2004). His-tagged G6PI was expressed in Escherichia coli BL21. To purify recombinant protein from the bacterial lysate, nickel-nitrilotriacetic acid was added, followed by extensive dialysing against PBS and filter sterilization. To assess the purity and integrity of the protein, a sodium dodecyl sulfate-polyacrylamide gel electrophoresis (SDS-PAGE) was performed. A subcutaneous immunization was used to immunize mice aged 6–12 weeks with 400 µg G6PI emulsified in 100 µL complete Freund's adjuvant. To deplete Tregs, mice were injected with 400 g anti-CD25 (PC61.5) 11 and 8 days before vaccination. Control mice were left untreated. A protein G column was utilized to purify the antibody from the hybridoma culture supernatant (GE Healthcare, München, Germany). 0.1 M glycine (pH 2.7) was used to elute the bound IgG from the column after extensive washing with PBS. After dialyzing against PBS, the eluted antibody was sterilised on the filter. In reducing and non-reducing conditions, SDS-PAGE was used to test purity and integrity. Nico Andreas (AG Kamrath-Institute of Immunology; University of Jena) performed the arthritic induction experiments.

3.3.2 Preparation of single-cell suspensions for Seq-Well arrays

Mouse limbs were collected from all mice. After carefully removing the paws' skin, tendons, and muscles, the filaments were carefully cut without injuring the bones to separate them at the wrist and ankle. Isolated paws were digested with 1 mg/mL collagenase type IV (Worthington, LS004189) in a cell culture medium (Dulbecco’s modified Eagle’s medium (DMEM), Sigma, D5796, high glucose); supplemented with 10%

FCS, 1 mM sodium pyruvate (Sigma), 50 µM β-mercaptoethanol (Gibco), 100 U/mL streptomycin, and 10 mg/mL penicillin (PAN Biotech). The cells were strained through cell strainers (70 µm, BD Falcon) and washed in fully supplemented DMEM to remove tissue clumps and separate bones. Cell numbers were defined using a Neubauer chamber.

3.3.3 Preparation of Seq-Well arrays

Seq-Well arrays were prepared as described by Gierahn et al. (Gierahn et al., 2017; Baßler et al., 2022). As a quick overview, the Sylgard base and crosslinker were mixed for 10 min at a mixture ratio of 10:1. Afterward, the wafer was placed with an 86,000 well pattern-holding microscope slide under a vacuum for 15 min to remove air bubbles, then incubated the wafer for 2 hours at 70°C. The arrays were removed from the molds, cut away extra silicone, and prepared for functionalization. Chemical portions are added to the array surfaces that facilitate sealing the semipermeable polycarbonate membranes and the exchange of lysis and hybridization buffers. The arrays were rinsed with EtOH, plasma-treated the arrays for 10 minutes, and then immersed successively in APTES (0.05% APTES in 95% EtOH), acetone, and PDITC buffer (0.2% PDITC, 10% pyridine, 90% DMF). After additional acetone washes, the arrays were spun and dried at 70°C for 2 h. A crucial step in the protocol was incubating the arrays in 0.2% chitosan solution at 37°C and pH 6,3 for 1.5 h, followed by overnight incubation in PGA buffer (20 mg/mL polyglutamic acid, 2 M NaCl, 100 mM sodium carbonate (pH=10)) at room temperature under vacuum. After being removed from the vacuum, arrays were rotated for 3 h at room temperature and then moved to 4°C for at least 24 h before being used. (3.3.3 is modified from Baßler et al. 2022).

3.3.4 Cell loading and Seq-Well library preparation

Seq-Well libraries were created as recently described by Gierahn et al. with some modifications outlined below (Gierahn et al., 2017). After the functionalized arrays were

loaded with messenger ribonucleic acid (mRNA) capture bead and 30,000 cells suspended in RPMI 1640 medium supplemented with 10% FCS were loaded to each array resulting in a total cell number of 720,000 loaded cells throughout all samples derived from two mice per experimental condition. After loading the cells onto the array, the arrays were incubated for 10 min allowing the cells to settle into the wells. The arrays were washed repeatedly with PBS, soaked in RPMI 1640 medium, and then sealed with polycarbonate membranes treated with air plasma under a mild vacuum (Diener electronic). After a 30 min incubation time at 37°C, the arrays were placed in lysis buffer (5M guanidine thiocyanate, 1mM EDTA, 0.5% Sarkosyl, and 1% β-mercaptoethanol in H2O) for 20 min. Afterwards, the arrays were placed in hybridization buffer (2M NaCl, 3mM MgCl2 and 0.5% Tween-20 in PBS) for 40 min. As a next step, the mRNA beads were washed from the arrays and collected using a washing buffer (2M NaCl, 3mM MgCl2, and 20mM Tris-HCl pH 8.0 in H_2O). Maxima Reverse Transcriptase was used to reverse-transcribe the mRNA bound to the bead pellet (Maxima RT buffer, 4% Ficoll PM-400, 1mM dNTPs, 1U/µL RNase inhibitor, 2.5 µM template switch oligonucleotide primer, and 10U/µL Maxima Reverse Transcriptase in H_2O) by incubation for 30 min at room temperature, followed by 90 min incubation at 52°C with end-over-end rotation. To stop the reaction, the beads were washed with TrisEDTA buffer (10mM Tris-HCl pH 8.0 and 1mM EDTA in H_2O) supplemented with 0.1% Tween-20 and TrisEDTA buffer supplemented with 0.5% SDS (TrisEDTA-SDS). The beads were resuspended in 500 µL of H_2O and counted using a Fuchs-Rosenthal cytometer in a bead counting solution (10% PEG, 2.5 M NaCl). Beads were split into pools of 5,000 beads (10 µL). 40 µL PCR reaction mix was added to every pool (2X KAPA HiFi Hotstart Readymix and 25 µM Smart PCR primer in H_2O) for the amplification of reverse-transcribed cDNA libraries (95°C for 3 min, 4 cycles of 98°C for 20 s, 65°C for 45 s, 72°C for 3 min, 12 cycles of 98°C for 20 s, 67°C for 20 s, 72°C for 3 min and final extension of 72°C for 5 min). Following PCR, 16,000-20,000 beads were combined (referred to as 'pools') and further processed. The pools were cleaned with 0.6x volumetric ratio AMPure XP beads by 5 min incubation with beads, followed by 3 min incubation on the magnet, two washes with 80% EtOH, 5 min dry-out, elution with 13 µL H_2O for 3 min, followed by 2 min incubation on the magnet for collection of the eluent. The library integrity was assessed using a High Sensitivity D5000 assay for

the Tapestation 4200 (Agilent). The Tn5 transposase was produced in-house (Picelli et al., 2014) Tn5 coding region (tnpA gene from Escherichia coli, Uniprot accession number: Q46731, residues 1-476) was obtained as a synthesized gene containing the mutations E54K and L372P for hyperactivating the enzyme. Overhangs containing the restriction sites XbaI and SpeI were used to clone the Tn5-Intein-CBD fusion construct into the pTXB1 vector. Sanger sequencing was used to validate the Tn5 coding sequence. A pTXB1-Tn5-Mxe-CBD plasmid was next transformed into the BL21 strain of E.coli which were grown in LB media supplemented with ampicillin at 37°C to an OD600 of approximately 0.8. After lowering the temperature to 10°C, 0.25 mM IPTG was added to induce protein expression. After 4 hours of incubation at 23°C, cells were harvested by centrifugation on a JA 25.50 rotor (Beckman) for 20 min at 10°C. After resuspension in running buffer (20 mM Hepes-KOH, 0.8 M NaCl, 1 mM EDTA, 10% glycerol, 0.2% Triton-X 100), the pellet of cells was disrupted by sonication. In order to elute the nucleic acid contamination of E.coli from cell debris, dropwise additions of polyethyleneimine pH 7.5 with a final concentration of 0.3% were performed after centrifugation at 15,000 rpm on a Beckman JA 25.50 rotor for 30 min. Using the JA 25.50 rotor (Beckman) at 15,000 rpm for 30 min at 10°C, residual nucleic acid contaminations from E.coli were precipitated by adding polyethyleneimine pH 7.5 dropwise to a final concentration of 0.3%. After centrifugation at 12,000 rpm on a Beckman JA 25.50 rotor for 10 minutes at 4°C, the lysate was cleared. After equilibration with running buffer (10 mL), chitin resin (10 mL) was incubated at 4°C for 1 h with the prepared lysate. Beads were washed with 10 column volumes of running buffer. During the elution process using the intein-tag, the Tn5-loaded resin was incubated overnight at 4°C in 3 mL elution buffer (20 mM Hepes-KOH, 0.8 M NaCl, 1 mM EDTA, 10% glycerol, 0.2% Triton-X 100, 100 mM DTT). This was followed by dialysis at 4°C overnight in dialysis buffer (100 mM Hepes-KOH, 0.2 M NaCl, 0.2 mM EDTA, 2 mM DTT, 0.2% Triton-X 100, 20% glycerol). Bradford Assay was used to determine the protein concentration. Glycerol was added to the protein sample's final concentration of 50%. To load Tn5 with linker oligonucleotides (Tn5ME-B/Tn5MErev (Tn5ME-B: 5`- TCTCGTGGGCTCGGAGATGTGTATAAGAGACAG-3`; Tn5MErev: 5`-[phos]CTGTCTCTTATACACATCT-3`)), single-stranded oligonucleotides were mixed in a 1:1 ratio. Pre-annealing was performed by mixing 2 µL of oligonucleotide solution with 8

µL of H_2O and incubating in a thermocycler (95°C for 3 min, 70°C for 3 min, and 45 cycles of -1°C per 30 s)). 0.25 vol. annealed oligonucleotides were mixed with 0.1 vol. Tn5 solution, 0.12. vol. dialysis buffer, and 0.13 vol. H_2O. After 60 min incubation at room temperature, the protein was stored at -20°C. For each cDNA library (1 ng) in the TAPS-DMF buffer (50mM TAPS-NaOH (pH 8.5), 25mM MgCl2, and 50% DMF in H_2O), Tn5 transposase was added for 10 min at 55°C, followed by minElute PCR following the manufacturer's instructions. The final step was to prepare the master mix (2X NEBNext High Fidelity PCR Master Mix, 2.5 µM barcoded index primer, 2.5 µM P5-Smart-PCR primer) and add it to the samples in order to attach the Illumina indices to the tagmented products in a PCR reaction (72°C for 5 min, 98°C for 30 s, 15 cycles of 98°C for 10 s, 63°C for 30 s, 72°C for 1 min). The pools were cleaned using 0.8 x volumetric ratio AMPure XP beads, run with a High Sensitivity DNA5000 Assay on a Tapestation 4200 (Agilent), and quantified with a Qubit high sensitivity dsDNA Assay (3.3.4. is modified from Baßler et al. 2022).

3.3.5 Sequencing of Seq-Well libraries

A NextSeq500 system was used to pool and cluster the Seq-Well libraries at 1.4 pM concentration with 10% PhiX using High Output v2.1 chemistry. Paired-end sequencing was performed with a custom Drop-Seq Read 1 primer for 21 cycles, 8 cycles for the i7 index, and 61 cycles for Read 2. Single-cell data were demultiplexed using bcl2fastq2 (v2.20). (3.3.5 is modified from Baßler et al. 2022).

3.3.6 ScRNA-Seq raw data processing of the Seq-Well data

For preprocessing, the fastq files from Seq-Well experiments were loaded into a pre-processing data pipeline (version 0.31, available at https://github.com /Hoohm/dropSeqPipe) that relies on Drop-seq tools provided by the McCarroll lab (Macosko et al., 2015). Then, STAR alignment was performed within the pipeline using the mouse transcriptome (GRCm38, Gencode vM16 primary assembly). The resulting

datasets were then imported into the R and analyzed with the package ‘Seurat’ (Butler et al., 2018) for further analyses. (3.3.6 is modified from Baßler et al. 2022).

3.3.7 Data quality control

1,536,148 cellular barcodes were detected in the Seurat object, and cellular barcodes with less than 100 expressed genes and more than 20% mitochondrial gene countss were excluded from the following analysis. After filtering, the dataset contained 32,861 features across 33,635 cells. Next, the original gene counts for each cell were normalized by total transcript counts, multiplied by 10,000 (TP10K), and then log-transformed by log10 (TP10k + 1). Next, the genes with the highest cell-to-cell variability in the dataset were determined by calculating the top 2000 most variable genes by selecting the 'vst' method of the 'FindVariableFeatures’ function in Seurat (version 3.1.2). After scaling, the data dimensionality was reduced to 10 PCs used as input for UMAP representation. (3.3.7 is modified from Lankable and Horne et al. 2022).

3.3.8 Clustering and cluster annotation

The Seurat (version 3.1.2) SNN-graph-based Louvain clustering was performed using a resolution of 0.07. Clusters were annotated by comparing cluster marker genes with public sources.

3.3.9 Differential expression tests and cluster marker genes

All differential expression tests were performed using FindMarkers/FindAllMarkers functions in Seurat (version 3.1.2) with default two-sided non-parametric Wilcoxon Rank Sum test with Bonferroni correction using all genes in the dataset. Cluster marker genes with >1.5 log-fold changes were regarded as significantly DEGs. In addition, top-ranked genes (p-values) from each cluster of interest were extracted for further illustration.

3.3.10 Subset analysis of the mesenchymal subcluster, SF subcluster, normalized SF subcluster, and macrophage subcluster

The mesenchymal and macrophage subclusters were explored by subsetting the primary dataset. However, the SF subcluster was generated by subsetting all SLFs and LLFs on day 56. The normalized SF subcluster was investigated by subsetting 1,401 SFs for all experimental groups. The Variable gene selection (top 2000 variable genes) and scaling of the VE-like, Epi-like, and ExE-like cells with the ScaleData function of Seurat (version 3.1.2) was adapted to this dataset.

The dimensionality of the mesenchymal subcluster was then reduced to 10 PCs, SF subcluster to 3 PCs, normalized SF subcluster to 3 PCs, and macrophage subcluster to 10 PCs. These reductions served as input for the UMAP calculations. Finally, the SNN-graph-based Louvain clustering of the cells was performed using 0.07 for the mesenchymal subcluster and 0.1 for the macrophage subcluster.

3.3.11 Enrichment analysis with published scRNA-seq signatures

Using the ‘AUCell’ method (Aibar et al., 2017), a gene signature enrichment analysis was implemented in the package (version 1.10.1) in R. The package was applied to link observed cell clusters to existing studies. The resulting AUC values were normalized to the maximum possible AUC to 1 and subsequently visualized in violin plots.

3.3.12 Gene Ontology term enrichment analysis of acute inflammatory signatures

The FindMarkers function from the Seurat package used the Wilcoxon Rank Sum test to identify significant DEGs for the acute signatures of CCs, SLFs, and LLFs by comparing the cells clusters at day 0 with day 14. All DEGs sorted by adjusted p-value were used for the GOEA test by R package/ClusterProfiler (version 3.14.3) (Yu et al., 2012).

3.3.13 iRegulon transcription factor prediction analysis of chronic signatures

The Cytoscape (version v3.7.1) (Shannon et al., 2003) plug-in iRegulon (version 1.3) (Janky et al., 2014) was used to predict the TFs potentially regulating the chronification in CCs, SLFs, and LLFs. The FindMarkers function from the Seurat package used the Wilcoxon Rank Sum test to identify significant DEGs for the chronification signatures of CCs, SLFs, and LLFs by comparing the cells clusters at day 0 with day 56.

The genomic regions for TF-motif search were limited to 10kb around the respective transcriptional start sites and filtered for predicted TFs, which exceeded a cumulative normalized expression cutoff of 10 in the respective cluster and exhibited a higher expression at day 56 than at day 0. Subsequently, the resulting TFs were sorted counterclockwise by the potential of regulating the most downstream DEGs and constructed a network linking target genes among the cluster-specifically expressed marker genes and expressed regulators for visualization in Cytoscape.

4 Results

4.1 Result sections for Rosette-to-Lumen stage embryoids

This section used scRNA-seq to describe dynamic biological processes in RtL-embryoids. It was possible to identify individual cells and characterize the developmental stage of the RtL-embryoids. Further, it was possible to dissect each embryonic tissue with the obtained scRNA-seq data. Additionally, highly dynamic processes like embryonic tissue interaction and spacial tissue arrangement with a single-cell resolution were deciphered in RtL-embryoids.

4.1.1 Generation of embryo-like structures from reprogrammed ESCs

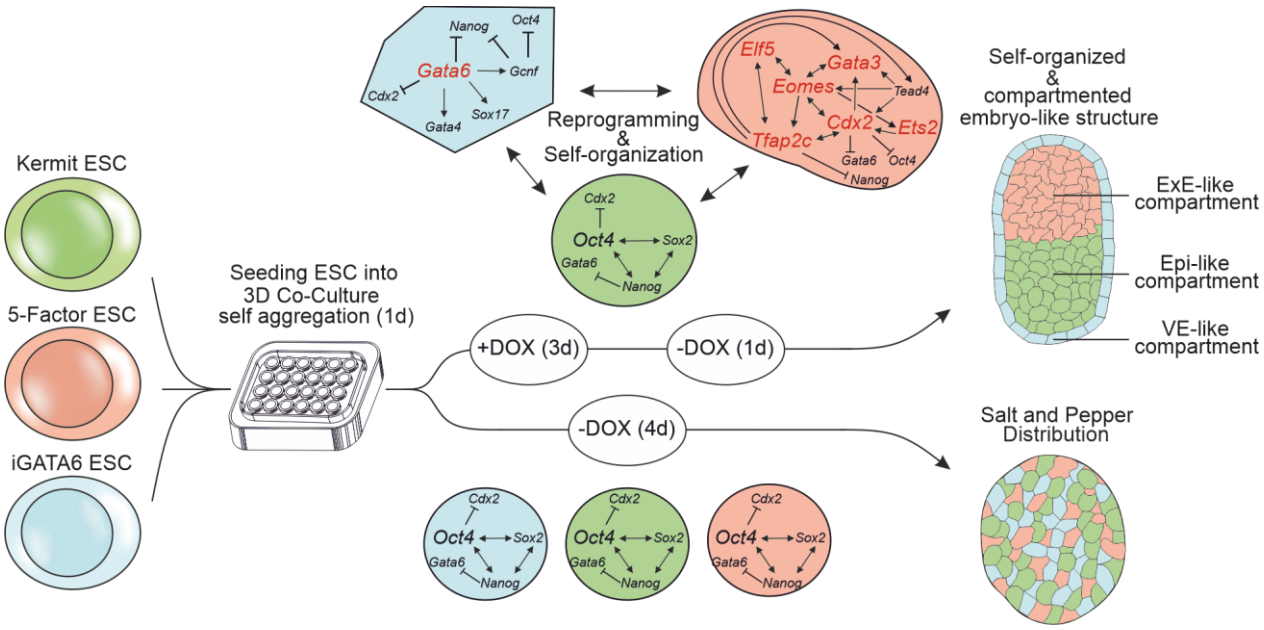

5. Protocol for the generation of embryo-like structures

Schematic protocol for the generation of embryo-like structures following the method introduced in this study. The three starting cell lines are seeded in 3D Petri Dishes and are allowed to settle and aggregate for 24 h. After that, for three days, transgene

expression in 5 Factor and iGATA6 ESCs is initiated by culture medium supplementation with DOX. After an additional day of culture without DOX, aggregates have formed VE-, Epi-, and ExE-like cellular compartment, resembling early, inner embryonic architecture. (Modified from Langkabel and Horne et al. 2021).

In the last two decades, it has been shown that ESCs can be reprogramed into TSCs and XEN cells (Niwa et al., 2005; Niakan et al., 2013; Wamaitha et al., 2015; Kaiser et al., 2020). In this study, the conversion of ESCs to iXEN cells was performed by overexpression of *Gata6* (Niakan et al., 2013; Wamaitha et al., 2015; Ngondo et al., 2018), and the conversion of iTSC was achieved via the overexpression of the transgenes encoding *Ets2*, *Tfap2c*, *Eomes*, *Gata3*, and *Cdx2* (Kaiser et al., 2020). Furthermore, it is known that primary ESCs, TSCs, and XEN cells can arrange themselves in early embryo-like structures and form tissue states which mimic the early embryonic architecture (Sozen et al., 2018; Zhang et al., 2019b). To show that TF-mediated cellular reprogramming is sufficient to generate embryo-like structures,a 5 Factor ESC line (5F-ESC) was used, including DOX-inducible transgenes *Ets2, Tfap2c, Eomes, Gata3,* and *Cdx2* (Kaiser et al., 2020) together with an ESC line carrying an *Oct4* promotor-driving GFP cassette, which was termed ‘Kermit ESC’. As the Kermit ESC gives rice to the ICM, iGATA6 ESCs were predicted to reprogram to iXEN (Niakan et al., 2013; Ngondo et al., 2018), and 5F-ESCs give rise to iTSC (Kaiser et al., 2020). To start the process of embryo-like structure generation, the three ESC lines were seeded in agarose micro-tissue wells to enable non-adherent growth in 3D (**5**). After one day of culture in a standard ESC medium (FCS, 2i/LIF), the culture medium was switched to a reconstructed embryo medium (Zhang et al., 2019b), which contains 2 µg/mL DOX, to start transgene expression of 5F-ESCs and iGATA6-ESCs, initiating reprogramming into an iTSC- or iXEN cell-fate, respectively.

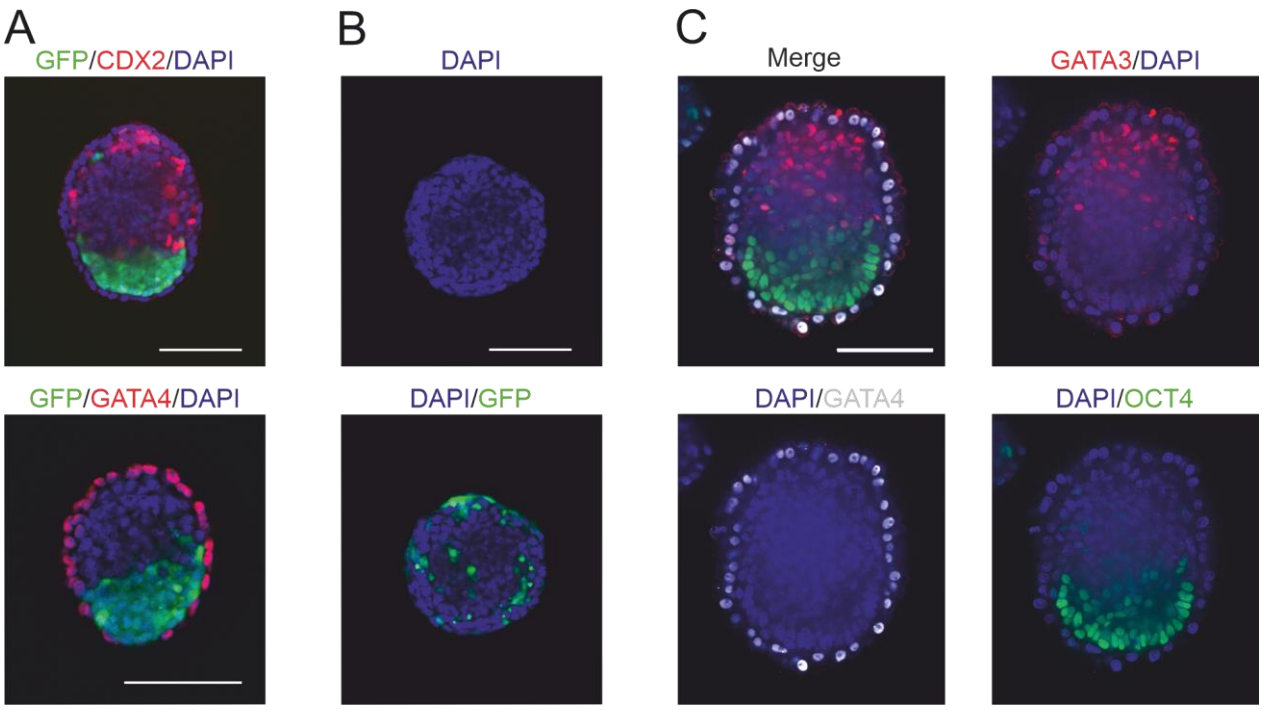

Figure 6. Images of embryo-like structures using reprogramming paradigms in ESCs

A Self-assembled embryo-like structures showing early embryo architecture comprised of an OCT4$^+$ (GFP$^+$; green) Epi-like compartment, next to a CDX2$^+$ (red) ExE-like compartment, both of which are surrounded by a GATA4$^+$ (red) VE-like compartment (lower image). DAPI, blue. **B** Image of aggregate composed of Kermit ESCs, 5 Factor ESCs, and iGATA6 ESCs and cultured without DOX supplementation, showing random distribution and localization of GFP$^+$ Kermit ESC and a complete lack of self-organization. GFP, green; DAPI, blue. Scale bar = 100 µm. **C** Substitution of Kermit ESCs with KNUT1 ESC, a non-fluorescent, unmodified ESC line, resulted in similar self-organization, displaying restriction of Epi- (OCT4$^+$; green), ExE- (GATA3$^+$; red), and VE- (GATA4$^+$; gray) marker expression to their respective compartments. DAPI, blue. Experiments were repeated independently at least three times with similar results (**A**, **B**, **C**). (Modified from Langkabel and Horne et al. 2021).

The cell aggregates showed morphological changes and self-organized into elongated and compartmentalized structures (**Figure 6A**). This finding contrasts significantly with the culture free of DOX. Without DOX, the aggregates exhibited a random cell arrangement known as ‘salt-and-pepper-like’ (**Figure 6B**). This observation implies that transgene induction over three days combined with the culture methods leads to an

internal regulation process of separating and reorganizing the cells in the aggregates. After three days, the culture medium supplemented with DOX was replaced with an ESC medium. One day after this step, the aggregates showed compartmentation into an epiblast-like (Epi-like) compartment consisting of (GFP^+) Kermit ESCs-derived cells, adjacent to CDX2-positive extraembryonic ectoderm-like (ExE-like) compartment most likely derived from 5F-ESCs and a GATA4-positive sphere-like structure which encapsulates the two inner compartments, resembling VE-like (VE-like) compartment (**Figure 6A, C and Figure 7A, B**). It is known that GATA6 induces the expression of *Gata4* (Wamaitha et al., 2015). Therefore, it was suggested that the VE-like compartment is descendants of the iGATA6 ESCs.

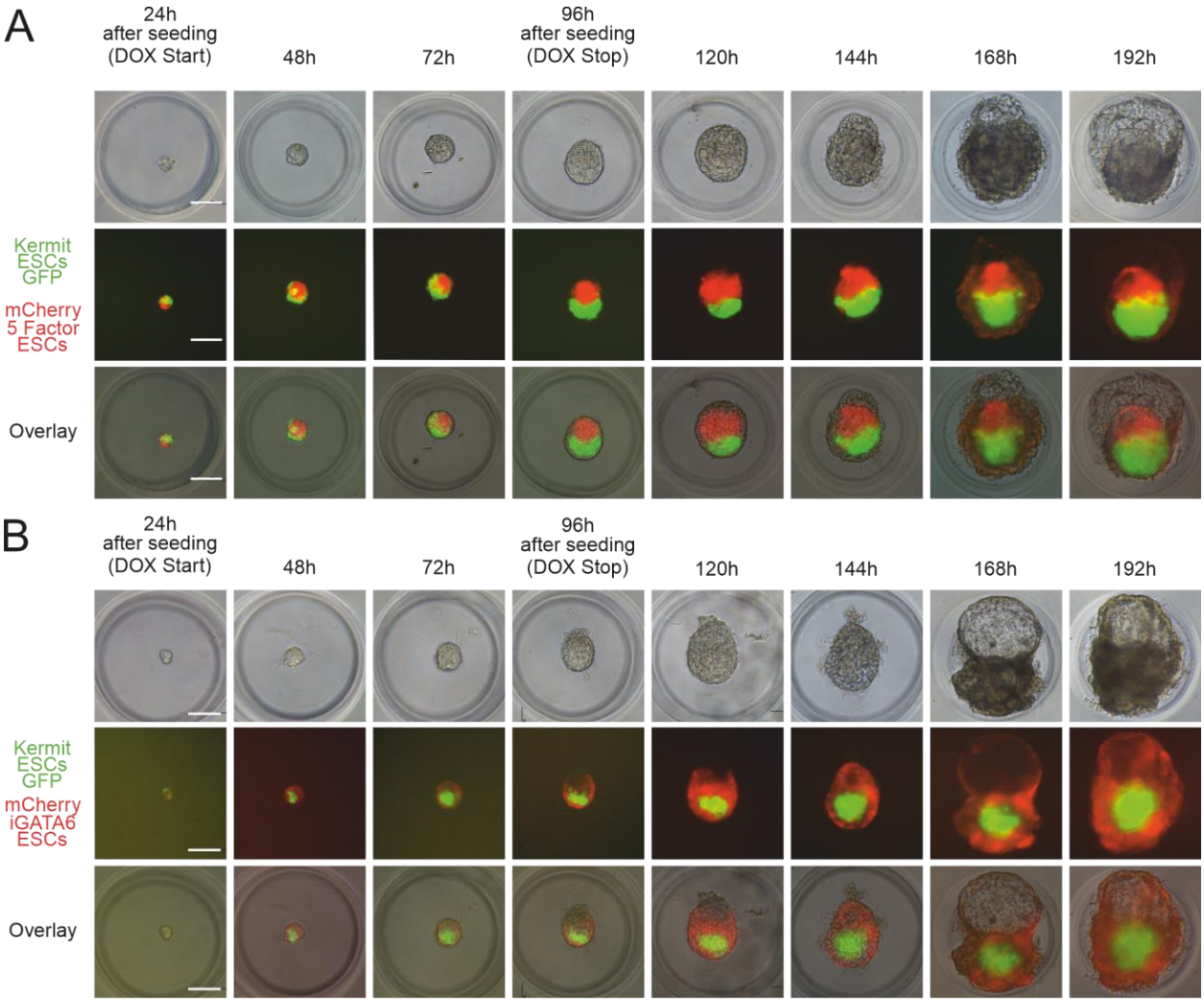

Figure 7. Development of RtL-embryoids over time

A Development of embryo-like structures built from Kermit ESCs, iGATA6 ESCs, and a 5 Factor ESC line transduced with a constitutive mCherry expression cassette. Detection of GFP originating from Kermit ESCs and mCherry from 5 Factor ESCs allows for visualization of self-organization into an epiblast-like (GFP^+, green) and extraembryonic ectoderm-like ($mCherry^+$, red) compartment. **B** Development of embryo-like structures built from Kermit ESCs, 5 Factor ESCs, and an iGATA6 ESC line transduced with a constitutive mCherry cassette. Detection of GFP originating from Kermit ESCs and mCherry from iGATA6 ESCs allows for visualization of self-organization into an epiblast-like (GFP^+, green) and visceral endoderm-like ($mCherry^+$, red) compartment. Scale bars = 100 µm. (Modified from Langkabel and Horne et al. 2021).

4.1.2 Compartmentation efficiency and rosette and lumen formation

Different cell ratios of the three ESC lines were tested to optimize the compartmentation of the embryo-like structures. It has been shown that an averaged combination of 6 Kermit ESCs, 16 5F-ESCs, and 5 iGATA6 ESCs per microwell of the agarose 3D-culture dish yielded the highest number of correctly compartmented structures. This finding is comparable with cell ratios recently published for the generation of ETX embryos (Sozen et al., 2018). Furthermore, 1,167 (day 4) and 778 aggregates (day 5) were counted in three independent experiments. On day 4, 15%, and one day later, 25% of aggregates exhibited the correct compartmentation, suggesting a successful seeding process and showing the reliability of this method for generating embryo-like structures (**Figure 8A**). A comparison of the seeding efficiencies with efficiency rates reported by studies published previously, like ETX embryos (29.8%) (Sozen et al., 2018), iETX embryos (between 20% – 30%)(Amadei et al., 2021), and ETX-embryoids (~23%)(Zhang et al., 2019b) shows comparability of all these approaches.

For a more comprehensive analysis of marker expression and morphological structuring within the Epi-like compartment, GFP^+ Kermit ESCs were substituted with a non-fluorescent ESC line, KNUT1 (Peitz et al., 2007). These embryo-like structures were stained against OCT4, GATA3, and GATA4 and again revealed the organizational ability of the structures, showing an $OCT4^+$ Epi-like compartment next to a $GATA3^+$ ExE-like

compartment, both of which were detected to be surrounded by a GATA4^{+} VE-like layer (**Figure 6A**). Further, rosette and lumen formation in the embryo-like structures were expected, which are central biological processes in mouse embryo development, and they appear from day E4.5 to day E5.25 (**Figure 8B**). Successfully these structures could be shown with an actin staining, showing the aggregation of actin fibers in the center of the inner embryonic and extraembryonic tissues (**Figure 8C, D**). These critical features of embryogenesis lead to the term Rosette-to-Lumen-embryoids (RtL-embryoids), which will be used for these structures in this thesis. In rare cases, a lumen fusion was observed, forming structures that seemingly progressed to a more advanced developmental stage, resembling ~E6.5 embryos (**Figure 8E**). Due to their rareness, it was not easy to further characterize such E6.5-like structures, but this observation indicates the further developmental potential of such RtL-embryoids. Aggregates composed of ESCs and cells reprogrammed from iGATA6 ESCs also showed lumen formation in the center of the ESC compartment, similar to ExE-embryoids (Zhang et al., 2019b), that consist of blastocyst-derived ESCs and XEN cells (**Figure 8H**). Together these hints toward the essential role of the XEN cells in lumenogenesis.

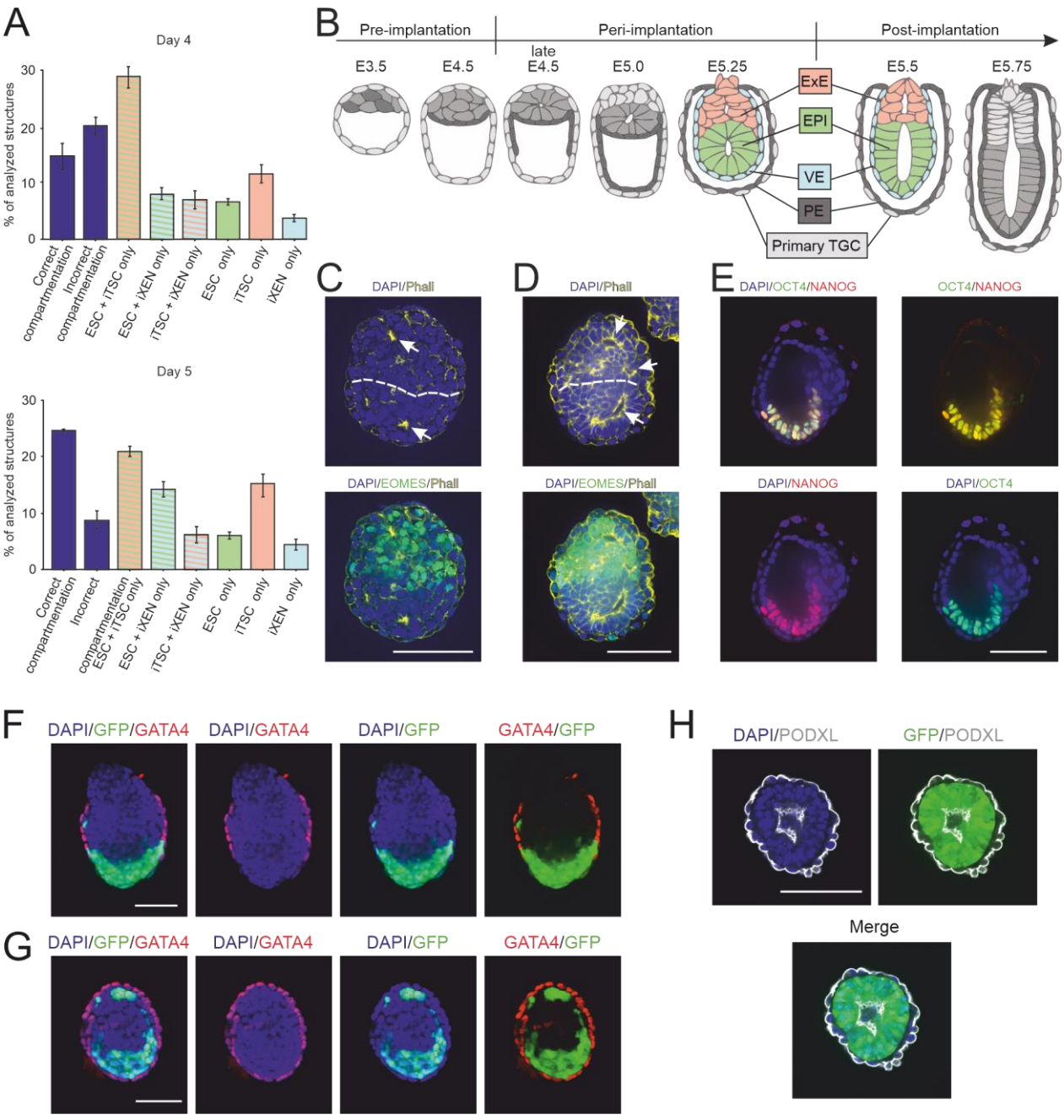

Figure 8. Efficiency of RtL-embryoid development and rosette and lumen formation

A On Day 4 of the protocol (Day of DOX Stop), ~15% (total n = 1167) of the structures analyzed displayed embryo-like architecture (Top Figure). On Day 5 of the protocol, ~25% (total n = 778) of the structures analyzed displayed embryo-like architecture (lower Figure). Data presented as mean values ± SD. **B** Scheme of the embryonic architecture of E3.5 to E5.75 embryos. EPI-, ExE-, and VE-like compartments resemble the inner compartments of murine embryos between E5.25 and E5.5. DiExE Distal ExE, PrExE

Proximal ExE, EPC ectoplacental cone, PE parietal endoderm, TGC trophoblast giant cell. **C** RtL-embryoids displayed rosette formation, indicated by aggregation of actin filaments. **D** RtL-embryoids displayed lumen formation in Epi- and ExE-like compartments. Phalloidin (Phall), yellow; EOMES, green; DAPI, blue. **E** In rare cases, complete lumenogenesis was observed, showing the formation of a cavity spanning both Epi- and ExE-like compartments. Scale bars = 100 µm; Dotted lines indicate the border of Epi- and ExE-like compartments. OCT4, green; NANOG, red; DAPI, blue. White arrows indicate rosette and lumen formation. **F** Examples of incomplete or **G** incorrectly assembled structures excluded from the analysis. Scale bars = 100 µm. GFP, green; GATA4, red; DAPI, blue. **H** Aggregate composed of Kermit ESCs and iGATA6 ESCs readily displays lumen formation, as indicated by staining against PODXL. Scale bar = 100 µm. GFP, green; PODXL, gray; DAPI, blue. Experiments were repeated independently at least three times with similar results (**C**-**H**). (Modified from Langkabel and Horne et al., 2021)

4.1.3 Distinct transcriptional profiles of embryo-like tissues

Self-organization into an embryo-like architecture was observed together with rosette and lumen formation. To get further insights into the biology of RtL-embryoids, scRNA-Seq was used to analyze the transcriptomes of this system to determine whether three distinct cell lineages characterize the three compartments defined immunohistochemically and whether there is further cellular heterogeneity within each compartment. To set up such an experiment, correct compartmentalized RtL-embryoids were preselected and created using a mCherry-transduced iGATA6 ESC line with GFP^+ Kermit ESCs and unstained 5F-ESCs. Correct compartmentalized RtL-embryoids exhibited a $mCherry^+$ sphere-like structure surrounding a GFP^+ compartment and an unstained ExE-like compartment (**Figure 7A**). Aggregates that could not meet the criteria were excluded from the subsequent Smart-seq2 protocol (**Figure 8 F, G**). 24 h after depletion of DOX, RtL-embryoids were harvested and brought to a single cell suspension. Staining against CD40 combined with GFP-signal-based exclusion of Epi-like cells allowed the separation of $CD40^+$ ExE-like cells from the residual cells of the embryo-like structures, as described for the early murine embryo (Rugg-Gunn et al., 2012). Together with GFP and mCherry, this labeling allowed for the identification of VE-like cells ($mCherry^+/GFP^-/CD40^-$), Epi-like cells ($GFP^+/mCherry^-/CD40^-$), and ExE-like cells ($CD40^+/GFP^-/mCherry^-$) (**Figure 9 B**). To

obtain high-quality single-cell transcriptomes, each cell type was sorted proportionally into 384-well plates before Smart-seq2 library preparation (Picelli et al., 2013) (**Figure 9A, B**). 961 cells past our quality criteria (see method section for detailed filtering steps 3.2.13). UMAP was used for dimension reduction. This method separated three distinct cell clusters (**Figure 9C**). Single-cell quality criteria indicated a comparable number of genes per cell, uniquely aligned genetic reads, cell numbers, and read variation between the three clusters (**Figure 9 D - G**). To assess the identity of these three cell clusters, the mapping of known marker genes for Epi, ExE, and VE identified cluster 1 to be VE-like cells (*Amn, Dkk1, Gata4, Sox17*), cluster 2 as Epi-like cells (*Pou5f1, Nanog, Gdf3, Tdgf1*) and cluster 3 as ExE-like cells (*Cdx2, Elf5, Eomes, Tfap2c*) (**Figure 9H, I**). These findings indicate that the previously immunohistochemically identified compartments display lineage-specific marker gene expression. As a next step, the FindAllMarkers() function was used with default settings (two-sided non-parametric Wilcoxon rank-sum test with Bonferroni correction using all genes in the dataset) in the Seurat R package (Butler et al., 2018). All DEGs between the three clusters were identified, the top 100 genes by adjusted p-value were selected, and GOEA was performed. This method revealed enrichment in ‘extracellular structure formation’ and ‘endoderm development’ terms in cells of the VE-like cluster, further supporting their successful transcriptional reprogramming (**Figure 9J**). Cells within the Epi-like cluster were characterized by terms including ‘response to leukemia inhibitory factor’ and ‘gastrulation’. Among the highest enriched gene sets in the ExE-like cluster were the ‘regulation of actin filament−based process’ and ‘epithelial cell development’, suggesting a more differentiated ExE-like compartment. However, enrichment sets like ‘placenta-‘ and ‘embryonic placenta development’ were detected, suggesting specific developmental programs in this cellular compartment (**Figure 9H**). In line with these findings, significant enrichment in gene signatures were found derived from mouse embryos (Cheng et al., 2019), further encouraging the identity of VE-like, Epi-like, and ExE-like cells (**Figure 9K**). TF binding prediction analysis was performed to determine upstream regulators of the transcriptionally reprogrammed ESCs. Strong enrichment of the TF Sall4 was found within cells of the VE-like cluster, which is the key regulator of the XEN lineage-associated genes *Gata4*, *Gata6*, *Sox7*, and *Sox17* (Wamaitha et al., 2015; Lim et al., 2008) (**Figure 9L**). In

the Epi-like cells, an enrichment of known embryonic stem cell TFs were shown (*Pou5f1*, *Sox2*), but the two TFs with the highest enrichment scores were *Tcf3* and *Nac1*, both of which are essential for regulating ESC differentiation and lineage specification of EPI cells in gastrulating mouse embryos (Malleshaiah et al., 2016; Hoffman et al., 2013). The ExE-like cluster demonstrated strong enrichment of *Cdx2*, encoding for a fundamental TF responsible for trophectoderm development (Huang et al., 2017).

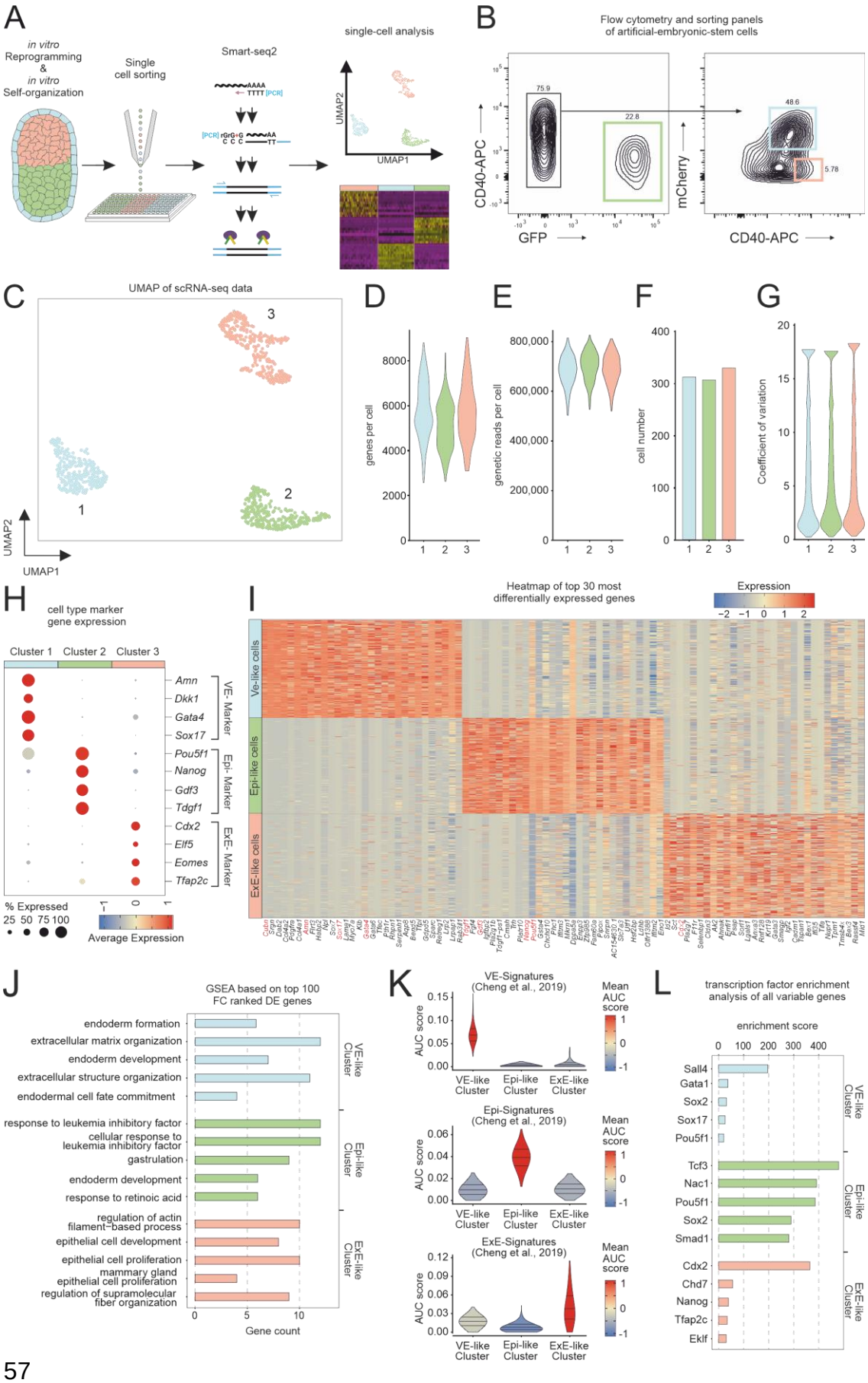
A
in vitro
Reprogramming
&
in vitro
Self-organization
Single
cell sorting
Smart-seq2
single-cell analysis
UMAP2
UMAP1
B
Flow cytometry and sorting panels
of artificial-embryonic-stem cells
CD40-APC
GFP
mCherry
CD40-APC
75.9
22.8
48.6
5.78
C
UMAP of scRNA-seq data
3
2
1
UMAP2
UMAP1
D
genes per cell
E
genetic reads per cell
F
cell number
G
Coefficient of variation
H
cell type marker
gene expression
Cluster 1
Cluster 2
Cluster 3
Amn
Dkk1
Gata4
Sox17
Pou5f1
Nanog
Gdf3
Tdgf1
Cdx2
Elf5
Eomes
Tfap2c
VE- Marker
Epi- Marker
ExE- Marker
% Expressed
25 50 75 100
Average Expression
I
Heatmap of top 30 most
differentially expressed genes
Expression
VE-like cells
Epi-like cells
ExE-like cells
J
GSEA based on top 100
FC ranked DE genes
endoderm formation
extracellular matrix organization
endoderm development
extracellular structure organization
endodermal cell fate commitment
response to leukemia inhibitory factor
cellular response to
leukemia inhibitory factor
gastrulation
endoderm development
response to retinoic acid
regulation of actin
filament−based process
epithelial cell development
epithelial cell proliferation
mammary gland
epithelial cell proliferation
regulation of supramolecular
fiber organization
Gene count
VE-like
Cluster
Epi-like
Cluster
ExE-like
Cluster
K
VE-Signatures
(Cheng et al., 2019)
Epi-Signatures
(Cheng et al., 2019)
ExE-Signatures
(Cheng et al., 2019)
AUC score
Mean
AUC
score
VE-like
Cluster
Epi-like
Cluster
ExE-like
Cluster
L
transcription factor enrichment
analysis of all variable genes
enrichment score
Sall4
Gata1
Sox2
Sox17
Pou5f1
Tcf3
Nac1
Pou5f1
Sox2
Smad1
Cdx2
Chd7
Nanog
Tfap2c
Eklf
VE-like
Cluster
Epi-like
Cluster
ExE-like
Cluster

Figure 9. Flow cytometry of Smart-seq2 experiment and analysis of transcriptional profiles

A Schematic representation of assay performed for Smart-seq2 analysis. **B** Flow cytometry and sorting panels of cells from RtL-embryoids (light red sorting gate ExE-like cells/CD40-APC^{+}; light green sorting gate Epi-like cells/ GFP^{+}; light blue sorting gate VE-like cell/mCherry^{+}). **C** UMAP representation of scRNA-seq results, showing 3 distinct transcriptomic clusters. **D** – **G** scRNA-seq library statistic of data obtained from Smart-seq2 technology. **H** Dot Plots showing expression of stem-cell-specific marker genes (*Amn*, *Dkk1*, *Gata4*, *Sox17* = VE-like cells; *Pou5f1/Oct4*, *Nanog*, *Gdf3*, *Tdgf1* = Epi-like cells; *Cdx2*, *Elf5*, *Eomes*, *Tfap2c* = ExE-like cells). **I** Heatmap showing expression of top 50 differentially expressed genes of VE-like cluster, Epi-like cluster, and ExE-like cluster. Genes are represented in rows and cells in columns. **J** GO term enrichment analysis of top 100 differentially expressed genes (log-fold change 1.5; FDR $p < 0.05$). Statistical test: GO terms were selected from the top sorting by adjusted P-value (p adjusted < 0.05, one-tailed hypergeometric test with Benjamini–Hochberg correction). Bars depict fold enrichment for terms with $p < 0.05$. **K** AUCell-based enrichment scores (AUC scores) showing similarity of gene expression signatures of the three clusters compared to their respective natural counterparts as assessed by Cheng et al., **L** Transcription factor enrichment analysis showing enrichment score of key transcription factors for VE-like, Epi-like, and ExE-like clusters. (Modified from Langkabel and Horne et al. 2021).

The next step was classifying the developmental stages reflected by each induced tissue. ScRNA-seq data of RtL-embryoids were compared to datasets derived from cells of murine embryos up to E7.5 (Posfai et al., 2021; Posfai et al., 2017; Chen et al., 2016a; Mohammed et al., 2017; Pijuan-Sala et al., 2019) (**Figure 10A, B**). VE-like cells showed high similarity with transcriptional signatures of PE cells and did not show progression for a VE-like identity. This finding was surprising because of the previous evidence for a VE-like tissue identity. Epi-like cells were mapped onto the murine embryo dataset, and a clustering divided between the E4.5 and E5.5 EPI cells was observed. This finding aligns with the rosette and lumen formation of the natural murine embryo during this period (Neagu et al., 2020). ExE-like cells revealed the most significant overlap with cells derived from ExE and a smaller overlap with the trophectoderm. Again, this finding indicates a development progression within the trophectoderm lineage. The remaining ExE-like cells clustered to EPI E5.5 cells. It was hypothesized that the cell population exhibited an incomplete reprogramming from ESC to iTSC fate. These cells have implemented an ExE-

like transcriptional profile but carry a transcriptional footprint of the starting ESC population from which they were derived.

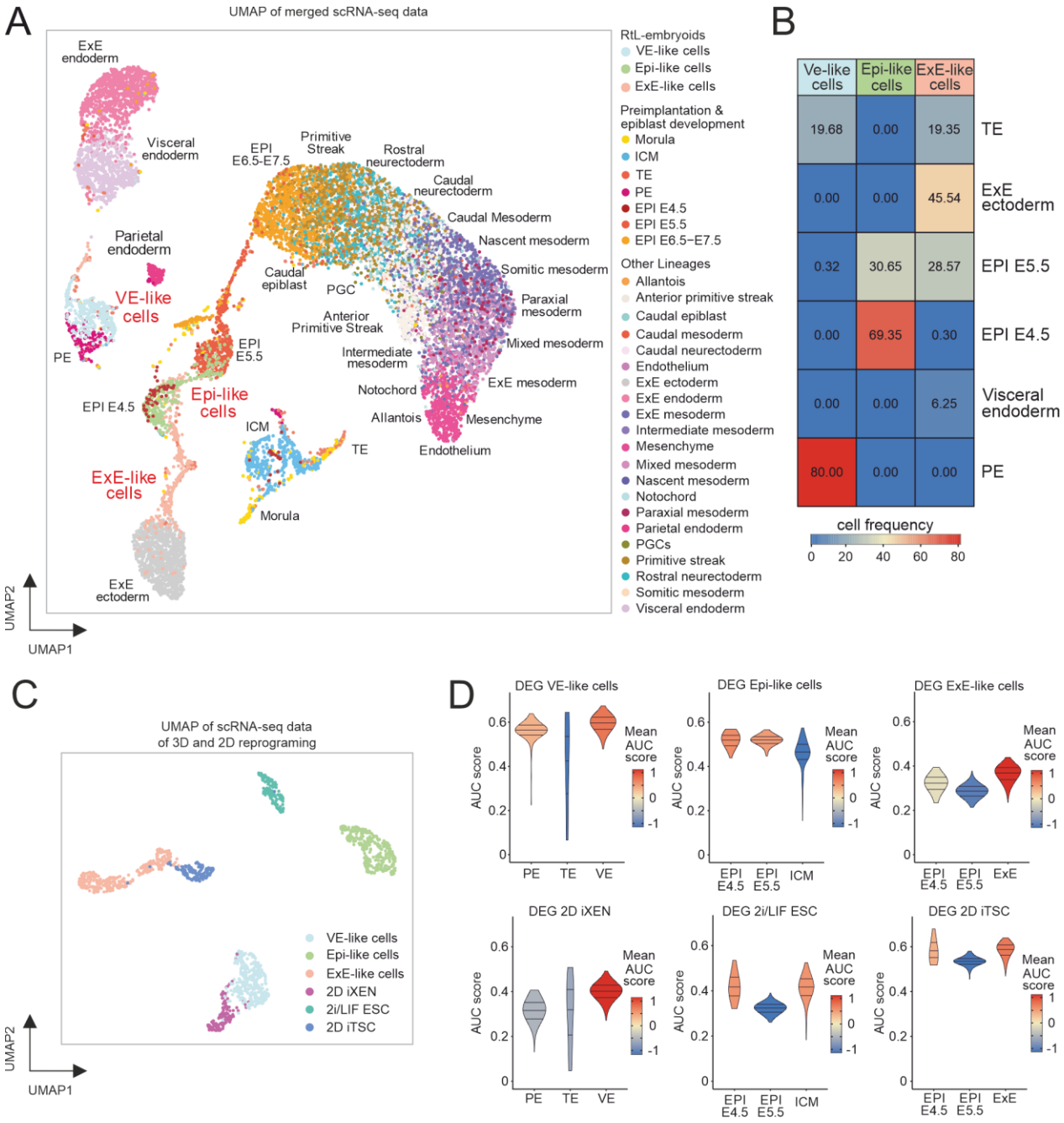

Figure 10. RtL-embryoid scRNA-seq data integration and 2D mono-culture to 3D co-culture comparison

A UMAP of four integrated reference datasets tracking cells during developmental stages from morula to E7.5 gastrulation in murine embryonic and extraembryonic lineages compared to RtL-embryoid VE-, Epi-, and ExE-like cells. **B** Heatmap of cell percentages from RtL-embryoid clusters mapped to the respective cell populations in the reference dataset of Fig.10A. **C** UMAP of scRNA-seq data of 3D and 2D reprogramming. **D** AUCell-based enrichment scores comparing gene signatures of 2D mono-culture and 3D co-culture induced ESCs, TSCs, and XEN cells to natural murine embryo cell clusters from Fig. 10A. (Modified from Langkabel and Horne et al. 2021).

4.1.4 Comparison of 2D mono-culture with 3D co-culture reprogramming

To assess whether these 3D co-culture-induced VE-like and ExE-like cells vary from their 2D mono-culture-induced counterparts, ESC-to-iXEN and ESC-to-iTSC conversions were performed in individual 2D cultures, either serum-based XEN cell- or TSC-medium supplemented with FGF4 and Heparin, correspondingly. After three days of DOX-mediated transgene expression and reprogramming, an additional 24h w/o DOX cells were harvested and subjected to the same experimental procedure as cells obtained from reprogramming in 3D co-culture (**Figure 9A**). ScRNA-seq showed that Epi-like cells obtained from 3D co-culture in RtL-embryoids and their counterparts in 2D mono-culture in 2i/LIF supplemented ESC medium varied significantly in their transcriptional state, encouraging the presumed progression in developmental stages (**Figure 10C**) (see method section for detailed filtering steps 3.2.13). XEN- and TSC-like cells revealed close but not overlapping clustering of transcriptional profiles with their 3D equivalents. Furthermore, the DEGs were specified between the 3D co-culture-induced cells and their 2D mono-culture-induced counterparts. Next, DEG signatures were compared with the datasets derived from cells of murine embryos via signature enrichment analysis. (**Figure 10A**). It could be shown that the VE-like cells enriched higher in the VE and PE signatures of murine embryos than XEN cells induced in 2D mono-culture (**Figure 10D**). The same was true for Epi-like cells, which showed enrichment in the signatures of Epi E4.5 and E5.5. The 2i/LIF ESCs signature was enriched in the EPI E4.5 and ICM and decreased overall compared to the Epi-like cells. The ExE-like cells showed a clear enrichment in the ExE signature of murine embryos but also displayed weak enrichment in the signature of

E4.5 EPI cells. 2D iTSC signature exhibited a higher enrichment in the murine ExE signature and a higher enrichment in the Epi E4.5 cluster than their 3D induced equivalents (**Figure 10D**), which can be understood as an indication of an even deeper footprint of the ESC origin. Taken together, scRNA-seq analysis supported the transcriptional reprogramming of ESCs into distinct cells within the VE-, Epi-, and ExE-like compartmented structures. Furthermore, the scRNA-seq analysis revealed close but not overlapping transcriptional profiles of 2D mono- and 3D co-culture induced XEN- and TSC-like cells, indicating that the cells in 3D cultures reprogram and differentiate further, presumably along with the induced cell fate.

4.1.5 DVE/AVE specification in the VE-like compartment of RtL-Embryoids

The iGATA6-ESCs are reprogrammed into iXEN cells organized into a VE-like sphere that envelops the two inner compartments (**Figure 6A, C**). As a next step, VE-like cells of the Smart-seq2 dataset were subclustered. The VE-like cluster exhibited two subclusters similar to an ExVE or an EmVE in previously introduced marker gene expression profiles (**Figure 11A, E**). Next, a published EmVE-signature (Cheng et al., 2019) was used to test for enrichment in the VE-like clusters, clearly showing that this signature is enriched in cluster 2, termed the EmVE-like cluster (**Figure 11B**). In the next phase, RtL-embryoids were characterized for further indications of a spatiotemporal organization like DVE and AVE formation.

To initiate this process, a specialized subpopulation of cells within the DVE is needed to express the T-box TF Eomesodermin (EOMES) (Nowotschin et al., 2013). In addition, it plays a crucial role in recruiting and activating other AVE factors, for example, Wnt and Nodal signaling antagonists *Lefty1*, *Dkk1,* and *Cerl* (Kimura-Yoshida et al., 2005; Takaoka et al., 2006) as well as *Otx2*, *Lhx1*, and *Hhex* (Perea-Gomez et al., 2001) (**Figure 11C**).

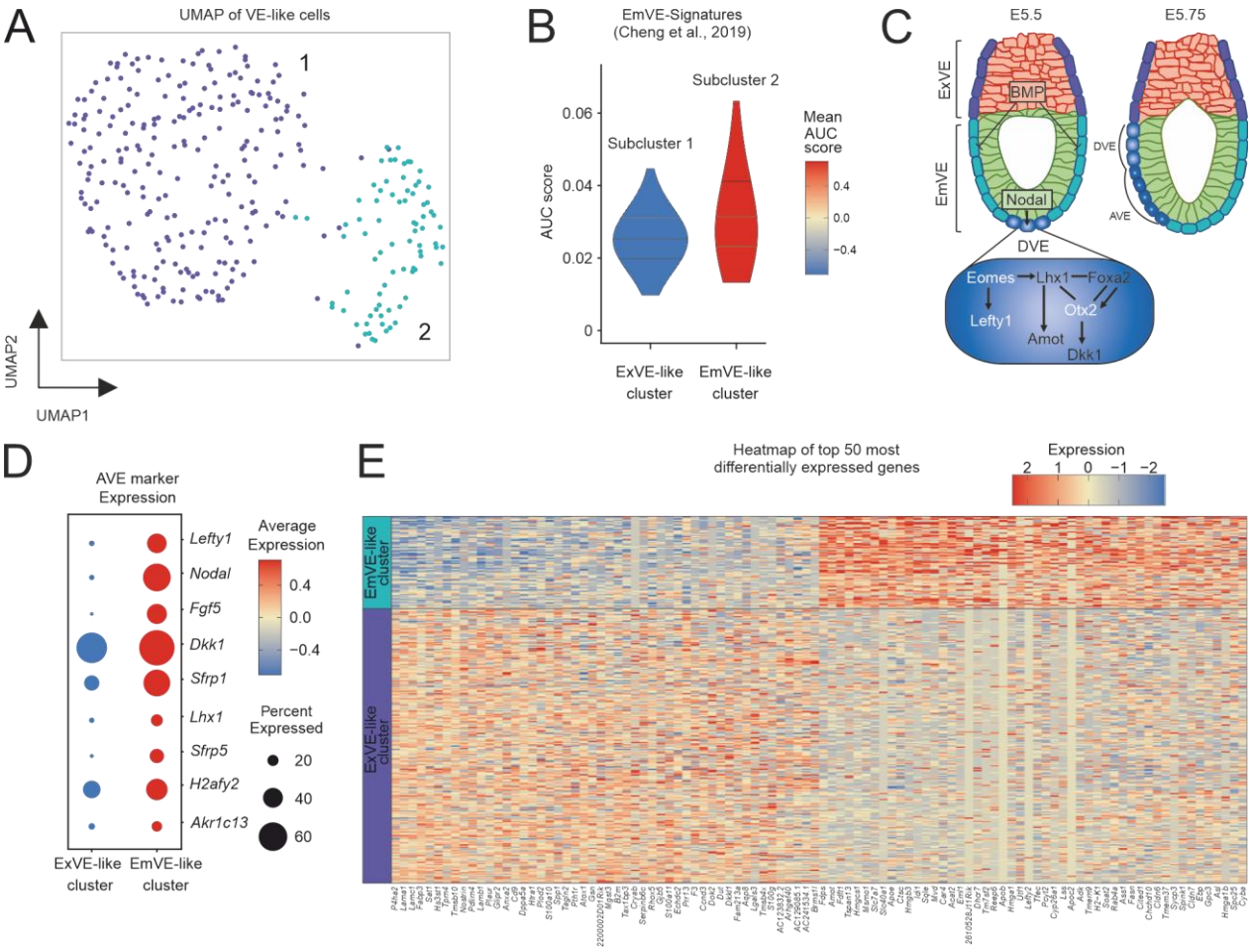

Figure 11. Formation of EmVE / ExVE -like population in VE-like compartment

A UMAP representation of VE-like cluster revealing two subclusters diverging in their transcriptional profile. **B** Comparison of EmVE-like cluster with the published scRNA-Seq dataset for EmVE of natural murine embryos revealing high AUCell-based enrichment score and mean expression levels of EmVE genes within EmVE-like cluster. **C** Schematic representation of DVE and AVE formation in murine embryos between E5.5 and E5.75. **D** Analysis of AVE marker expression in VE-like subclusters displays a higher expression of AVE marker gens inside the EmVE-like cell cluster. **E** Heatmap of variable genes of VE-like subclusters. Heatmap displays the top 50 differentially expressed genes for cells of the ExVE-like cluster and EmVE-like cluster. (Modified from Langkabel and Horne et al. 2021).

This specialized subpopulation of DVE cells migrates to one side of the Epi/ExE junction, localizing next to a second emerging signaling center, the AVE. DVE and AVE constantly

secrete Wnt and Nodal inhibitory proteins, establishing an anterior-posterior axis in the embryo. In RtL-embryoids, AVE marker genes, like Lefty1, Nodal, and Fgf5, were more expressed in EmVE-like cells compared to ExVE-like cells (**Figure 11D**) (Kumar et al., 2015). The enrichment of an AVE signature in the EmVE-like cluster further supported this model (**Figure 12A**) (Cheng et al., 2019). As AVE formation initiates anterior-posterior axis formation in a spatially confined manner, RtL-embryoids were immunohistochemistry stained against EOMES, OTX2, and LEFTY1 to visualize this process (**Figure 12B, C**). Successfully, co-expression of EOMES and OTX2 was observed in cells of the EmVE, correlating with LEFTY1 expression in these EOMES^{+}/OTX2^{+} cells (**Figure 12 B, C, D**).

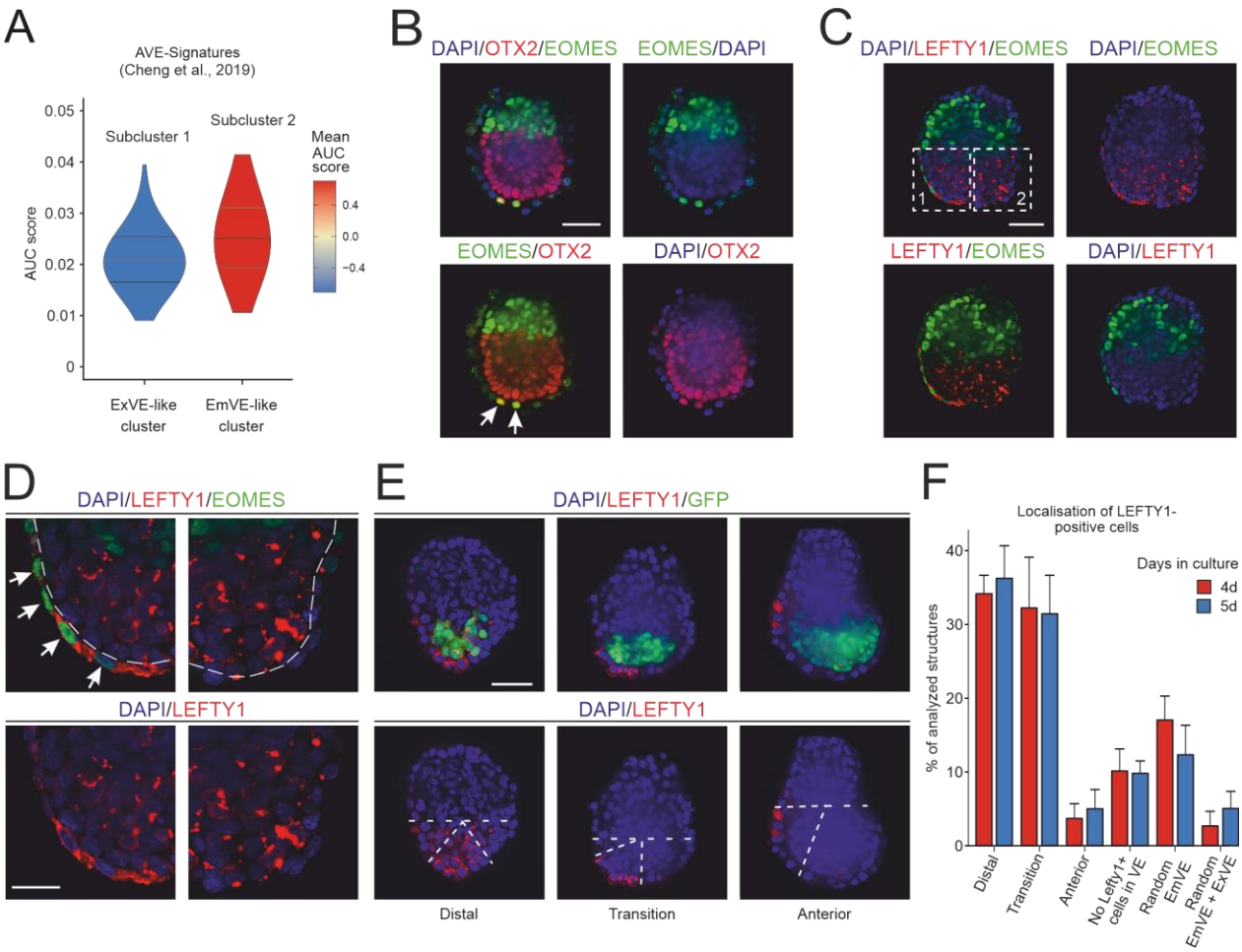

Figure 12. Formation of DVE/AVE-like population in VE-like compartment

A Comparison of published AVE-signatures showing high AUCell-based enrichment score and high mean expression for cells of the EmVE-like cluster, in contrast to a lower AUC score and mean expression levels in cells of the ExVE-like cluster. **B** Expression of DVE/AVE markers EOMES and OTX2 was detected to colocalize in cells of the EmVE-compartment in RtL-embryoids, indicated by white arrows. OTX2, red; EOMES, green; DAPI, blue. Scale bar = 50 µm. **C** DVE/AVE marker LEFTY1 was found colocalizing with $EOMES^+$ cells, which was restricted to one side of the EmVE-like compartment in RtL-embryoids (white squares are magnified in D). Scale bar = 25 µm. **D** Magnification of the EmVE-like compartment is indicated by the white, dotted squares in C. LEFTY1, red; EOMES, green; DAPI, blue. Scale bar = 20 µm. White arrows indicate $EOMES^+$ / $LEFTY1^+$ cells. **E** $LEFTY1^+$ cells were detected in distal, transition, or anterior positions in RtL-embryoids. LEFTY1, red; GFP, green; DAPI, blue. Scale bar = 50 µm. **F** Quantification of $LEFTY1^+$ cell location in RtL-embryoids on day 4 (4d) and day 5 (5d) into the protocol. The majority of RtL-embryoids displayed $LEFTY1^+$ cells in either distal or transition positions, with few RtL-embryoids showing localization of $LEFTY1^+$ in an anterior position, relative to the Epi-like compartments, both 4d (red bars) and 5d (blue bars) into the protocol. Total n = 375 for both conditions 4d and 5d. Data are presented as mean values ± SD. Experiments were repeated independently at least three times with similar results. (Modified from Langkabel and Horne et al. 2021).

Evaluation of localization of LEFTY1 positive cells revealed that the majority of RtL-embryoids showed LEFTY1 positive cells in either a distal or transition position, while LEFTY1 positive cells were only rarely detected at an anterior position within the EmVE (**Figure 12E, F**). It was also interesting that the localization of LEFTY1 positive cells was similar between day 4 and day 5, indicating a restricted/delayed migratory potential after the induction of DVE/AVE-like cell population. Another interesting observation was the nonrestricted LEFTY1 expression to the DVE in aggregates that displayed weak contribution of ExE-like tissue, most likely due to the absence of inhibitory BMP signaling from the ExE-like compartment that would be needed to restrict DVE specification to the distal tip of the VE (**Figure 13 and Figure 11C**). Collectively, the co-expression of EOMES, OTX2, LEFTY1, and AVE signature enrichment supports the concept of DVE/AVE formation in RtL-embryoids. However, the development of the anterior-posterior axis is limited, and further developmental steps might require adjustment in the culture conditions or the overall setup of the RtL-embryoid generation.

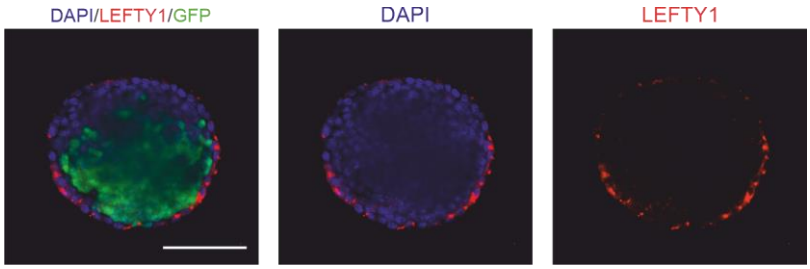

Figure 13. RtL-Embryoids with a weak contribution of ExE-like tissue

LEFTY1 expression throughout, but predominantly restricted to the EmVE in aggregates with a weak contribution of ExE-like tissue. GFP, green; LEFTY1, red; DAPI, blue. Scale bars = 100 µm. (Modified from Langkabel and Horne et al. 2021).

4.1.6 Cells of the Epi-like cluster show signs of core- to primed-pluripotency

Next, single-cell transcriptomes of the ESC-derived Epi-like cells were analyzed, showing three transcriptionally diverging subclusters (**Figure 14A**). Among the top 30 DEGs describing the Epi-like cluster, *Tdgf1* (alias: *Cripto)*, *Gdf3*, *Nanog,* and *Pou5f1* (alias: *Oct3/4*) were identified, which are well-described EPI marker genes (Chen et al., 2006; Fiorenzano et al., 2016; Mitsui et al., 2003; Mulas et al., 2018; Nichols and Smith, 2009; Rosner et al., 1990; Schöler et al., 1990) (**Figure 9I**). As the VE-like compartment exhibited a formation of AVE-like cells, gene expression for markers of anterior, transition, and posterior epiblast states was assessed in the Epi-like cluster (Cheng et al., 2019). Cells within the Epi-like cluster displayed strong signature enrichments with the published anterior EPI signature (Cheng et al., 2019) (**Figure 14B**). The absence of posterior-marker gene expression and the low levels of transition markers further supported this comparably strong enrichment. In addition to that, a strong expression of anterior marker genes were measured in the Epi-like cells (**Figure 14C**). In addition, GOEA for the Epi-like cell marker genes was assessed, and ‘embryonic pattern specification’, ‘embryonic axis specification’, and ‘anterior-posterior pattern specification’ were observed (Langkabel and Horne et al. 2021). These findings and the discussed DVE/AVE formation within the

VE-like compartment suggest that RtL-embryoids are in the phase of anterior-posterior axis formation. However, another possibility could be that RtL-embryoids face a developmental border and fail to complete anterior-posterior axis formation.

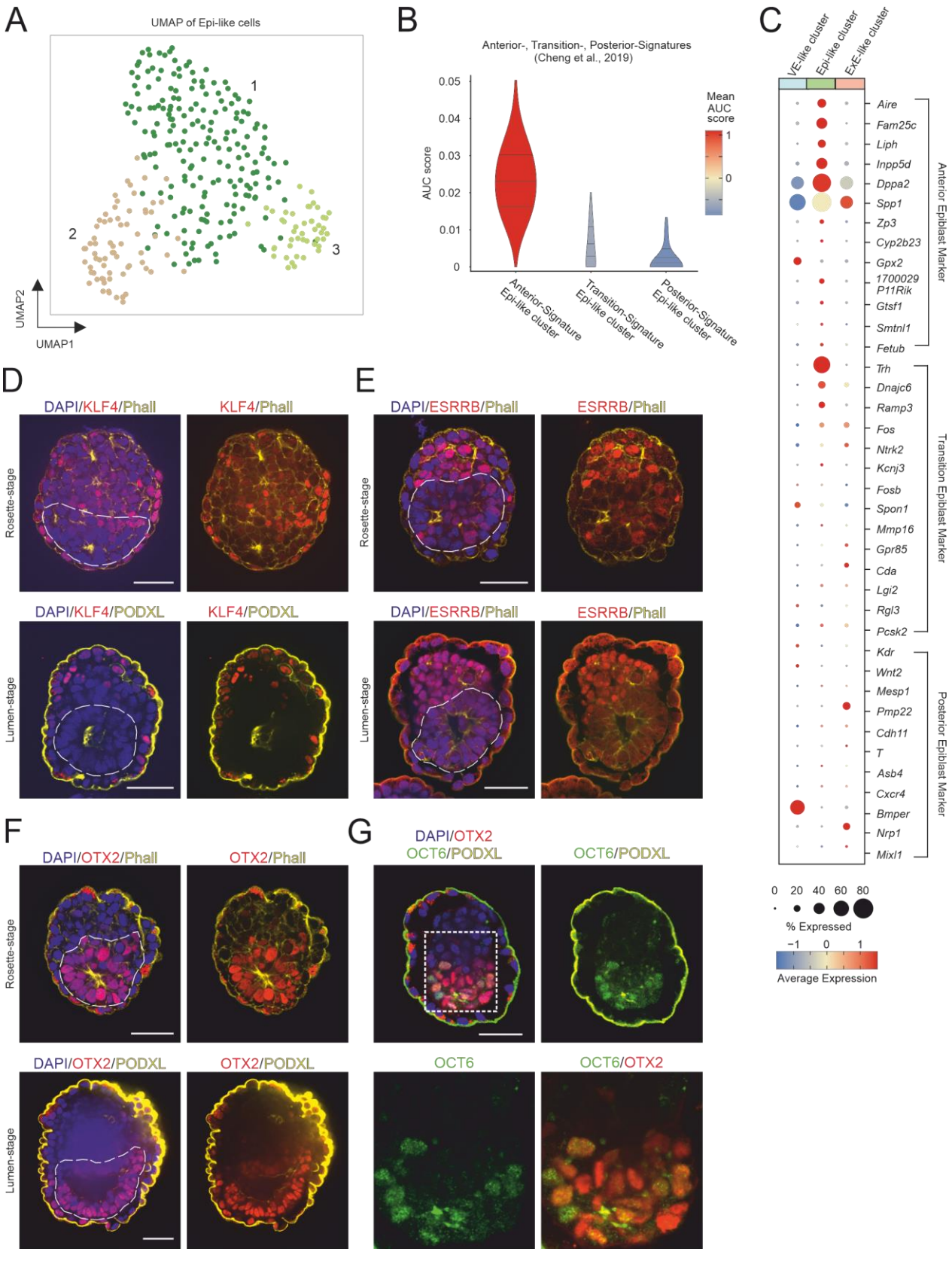
A
UMAP of Epi-like cells
1
2
3
UMAP2
UMAP1
B
Anterior-, Transition-, Posterior-Signatures
(Cheng et al., 2019)
AUC score
0.05
0.04
0.03
0.02
0.01
0
Mean AUC score
1
0
Anterior-Signature Epi-like cluster
Transition-Signature Epi-like cluster
Posterior-Signature Epi-like cluster
C
VE-like cluster
Epi-like cluster
ExE-like cluster
Aire
Fam25c
Liph
Inpp5d
Dppa2
Spp1
Zp3
Cyp2b23
Gpx2
1700029 P11Rik
Gtsf1
Smtnl1
Fetub
Trh
Dnajc6
Ramp3
Fos
Ntrk2
Kcnj3
Fosb
Spon1
Mmp16
Gpr85
Cda
Lgi2
Rgl3
Pcsk2
Kdr
Wnt2
Mesp1
Pmp22
Cdh11
T
Asb4
Cxcr4
Bmper
Nrp1
Mixl1
Anterior Epiblast Marker
Transition Epiblast Marker
Posterior Epiblast Marker
0 20 40 60 80
% Expressed
−1 0 1
Average Expression
D
DAPI/KLF4/Phall
KLF4/Phall
DAPI/KLF4/PODXL
KLF4/PODXL
Rosette-stage
Lumen-stage
E
DAPI/ESRRB/Phall
ESRRB/Phall
F
DAPI/OTX2/Phall
OTX2/Phall
DAPI/OTX2/PODXL
OTX2/PODXL
G
DAPI/OTX2
OCT6/PODXL
OCT6/PODXL
OCT6
OCT6/OTX2

Figure 14. Progression from naïve- to primed-pluripotency in EPI-like compartment

A The Epi-like compartment of RtL-embryoids shows three transcriptionally diverging subpopulations, assessed in UMAP representation. **B** Comparison to Anterior-, Transition-, and Posterior-Epiblast signatures published by Cheng et al. revealed the highest transcriptional similarity with anterior-epiblast cells. **C** Marker gene expression for Anterior-, Transition-, and Posterior-marker genes. **D** - **F** IF staining against pluripotency markers during progression from rosette- to lumen stage. The Epi-like compartment of RtLembryoids (indicated by dotted lines) displays downregulation of naïve-pluripotency markers KLF4 and ESRRB during progression from rosette to lumen stage. Expression of OTX2 was detected at both rosette and lumen stages. Scale bars = 50 µm. KLF4/ESRRB/OTX2, red; Phalloidin (Phall)/ PODXL, yellow; DAPI, blue. **G** Primed-pluripotency marker OCT6 was weakly expressed in some $OTX2^+$ cells at the lumen stage; Lower Panel shows the magnification of the area indicated above. Scale bars = 50 µm. OTX2, red; OCT6, green; PODXL, yellow; DAPI, blue. Experiments were repeated independently at least three times with similar results (**D**-**G**). (Modified from Langkabel and Horne et al. 2021).

In RtL-embryoids, lumenogenesis and rosette-formation were observed, occurring approximately at the same time as Epi-like cell progression from naïve- to primed-pluripotency (E5.0 and E5.5) (Neagu et al., 2020). The naïve pluripotency state is described by the expression of KLF4, NANOG, ESRRB, OTX2, and the absence of POU3F1 (alias: OCT6), whereas in primes pluripotency, OTX2, OCT6 expression was found and KLF4, NANOG, ESRRB were absent (Neagu et al., 2020). Nevertheless, TF expression is altered in the naïve pluripotency exit. This development is accompanied by pulses of phosphorylated ERK (pERK) in single cells within the EPI compartment (Neagu et al., 2020). In RtL-embryoids, a relative change of TF expression was observed, as downregulation of KLF4 and ESRRB during rosette to lumen stage progression was detected. In contrast, OTX2 was expressed at both stages (**Figure 14D - F**). Of note, KLF4 expression was also observed in cells of ExE- and VE-like compartments. Co-Expression of OCT6 and OTX2 was observed via confocal microscopy in Epi-like cells at the lumen stage, suggesting these cells of the RtL-embryoids model show the progression of EPI cells from a naïve- to primed-pluripotency state (**Figure 14G**). In contrast to this co-expression, NANOG expression in Epi-like cells throughout the rosette and lumen stage was detected, suggesting a delayed progression from naïve- to primed-pluripotency

state. This is supported by single pERK-positive Epi-like cells, exclusively observed in RtL-embryoids at the lumen stage. This observation was rare and not found throughout all RtL-embryoids (**Figure15B**). Our single-cell dataset evaluated transcript levels of known core-, naïve- and primed-pluripotency factors (Boroviak et al., 2014; Mohammed et al., 2017) exhibited a strong marker expression in two subclusters of either naïve- or primed-pluripotent states (**Figure 14A and Figure 15C**). High expression levels of primed-pluripotency factors (Nodal, Lef1, Fgf5, *Pou3f1,* and *Otx2*) were restricted to the Epi-like subcluster 2, while naïve -pluripotency factors (*Nanog, Tbx3, Tfcp2l1, Fbxo15, Esrrb, Zfp42, Dppa3, Klf2, Klf4,* and *Klf5*) was low expressed. However, these genes are upregulated in Epi-like subcluster 1, and the core-pluripotency factors (*Fgf4, Utf1, Gdf3, Tdgf1, Pou5f1,* and *Sox2*) were expressed throughout all Epi-like subclusters. The expression of primed pluripotency factors *Foxa2, Cer1,* and *T* was only detected in a few cells of the Epi-like cluster, providing additional indications for the presumed delay in development from naïve- to primed-pluripotency (**Figure 15C**).

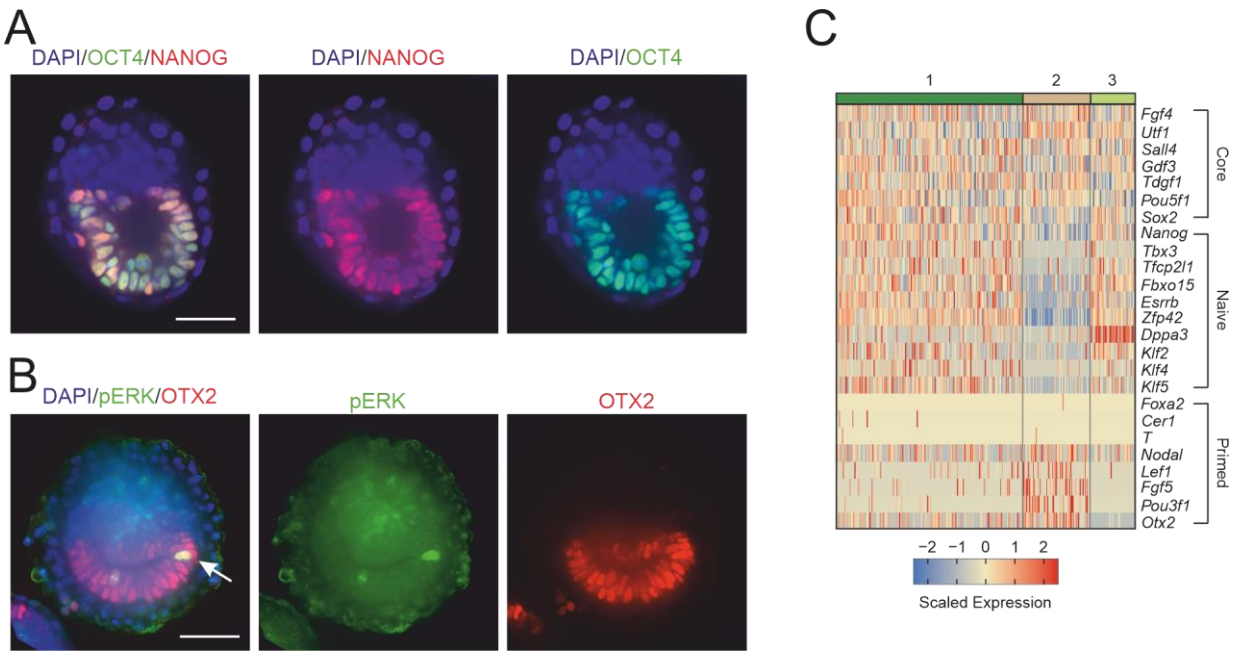

Figure 15. Expression of OCT4, NANOG and pERK; single-cell heatmap of core-, naïve-, and primed -pluripotency

A Expression of OCT4 and NANOG was detected in RtL-embryoids throughout the culture period. Scale bars = 50 µm. OCT4, green; NANOG, red; DAPI, blue. **B** pERK pulses were

detected in single Epi-like cells of RtL-embryoids at the lumen stage and a diffuse and weak pERK activity in the ExE-like compartment. Scale bars = 50 µm. OTX2, red; pERK, green; DAPI, blue. The white arrow indicates $pERK^+$ Epi-like cells. **C** Single-cell heatmap of core-, naïve-, and primed-pluripotency markers among cells of the Epi-like Subclusters, revealing predominantly naïve-pluripotency factor expression in subcluster 1, while subcluster 2 displayed downregulation of naïve- and upregulation of primed-pluripotency factor in subcluster 2. Subcluster 3 displayed a PGC-like character. Experiments were repeated independently at least three times with similar results (A, B). (Modified from Langkabel and Horne et al. 2021).

4.1.7 A subpopulation of Epi-like cells shows signs of primordial germ cell specification

After classifying Epi-like subcluster 1 and Epi-like subcluster 2, Epi-like subcluster 3 showed signs of primordial germ cell (PGC) specification. This differentiation depends on BMP4 and BMP8b secretion from cells of the ExE directly adjacent to the EPI and BMP2 produced by the VE (Lawson et al., 1999; Ying et al., 2000; Ewen-Campen et al., 2010; Ying and Zhao, 2001). These signals combined induce the expression of *Prdm1* (alias: *Blimp1)* and *Prdm14*, regulating the expression of germ cell development-specific genes *Tfap2c*, *Dppa3* (alias: *Stella)*, *Nanos3*, and *Kit* (Kwiatkowska and Cislo, 1975; MINTZ and RUSSELL, 1957; Payer et al., 2003; Weber et al., 2010; Werling and Schorle, 2002) (**Figure 16B**). In addition, it was possible to detect exclusive Bmp2 expression in cells of the VE-like cluster, while *Bmp4* and *Bmp8b* expression was restricted to the ExE-like compartment (**Figure 16C**). Target genes downstream of this signalling proteins like *Nanos3*, *Kit*, *Stella*, and *Tfap2c* were expressed within a subpopulation of the Epi-like cluster 3, with an expression of Nanos3 exclusive to this subcluster (**Figure 16D**). These findings indicate that the spatial organization of RtL-embryoids reflects proper embryonic architecture resulting in BMP-producing cells in their primordial compartments and creating an environment pushing cells of the epi-like compartment into PGC-like differentiation (**Figure15C**).

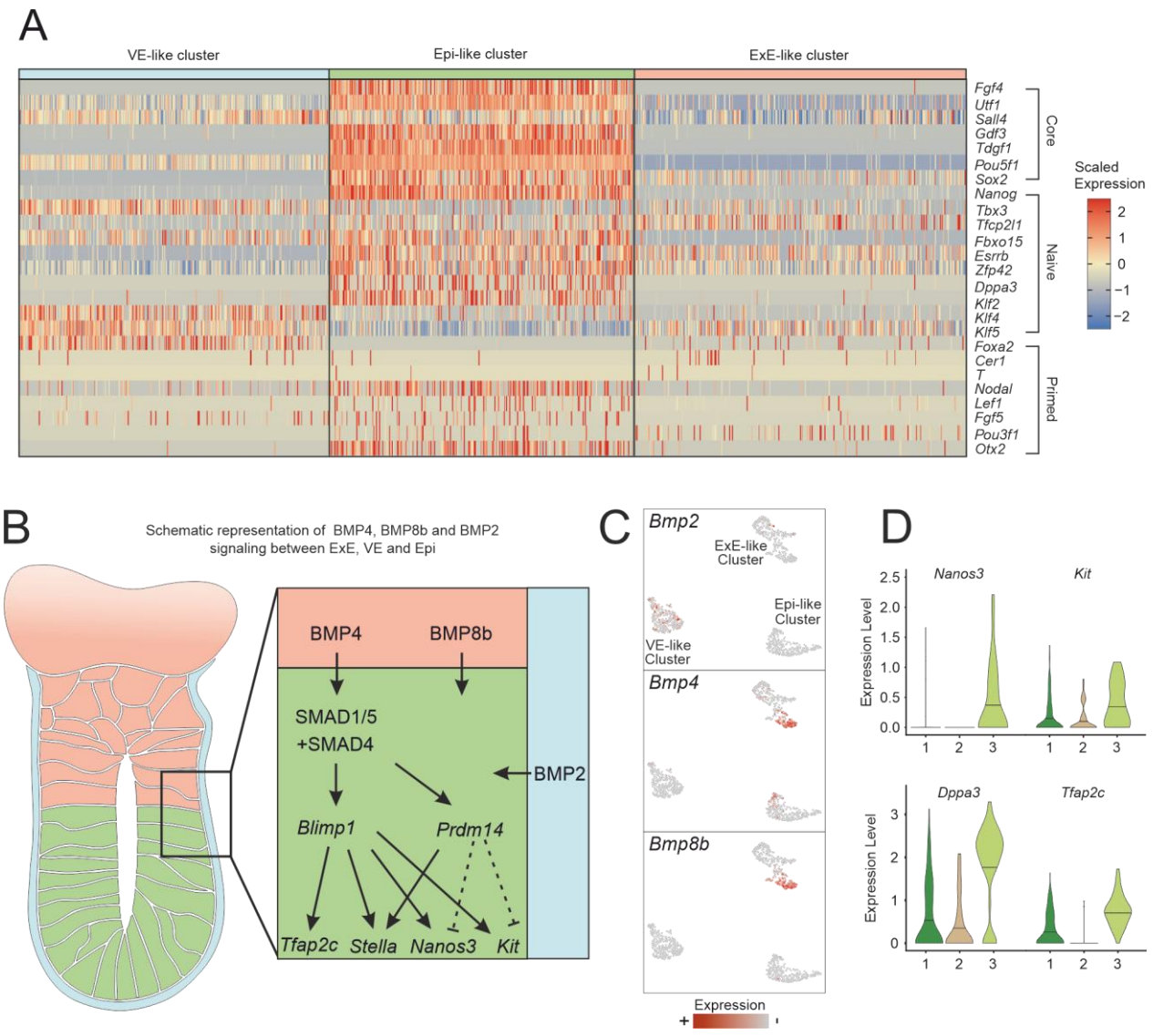

Figure 16. RtL-embryoids show indications for the induction of the molecular signaling cascade responsible for PGC specification

A Heatmap showing expression of core-, naïve-, and primed-pluripotency factors across cells of all three compartments comprising RtL-embryoids. **B** Schematic representation of signaling events leading to primordial germ cell (PGC) specification in the epiblast of murine embryos starting between E4.5 – E5.5 with the secretion of BMP4, BMP8b from the ExE, and BMP2 from the VE. **C** Feature plots mapping expression of Bmp2 in cells of the VE-like cluster and Bmp4 and Bmp8b in cells of the ExE-like cluster. **D** Violin plots showing a distinct subpopulation of cells expressing marker genes of PGC specification

Nanos3, *Kit*, *Dppa3* (*Stella*), and *Tfap2c*, identifying Epi-like subcluster 3 as cells displaying PGC-like cell fate. (Modified from Langkabel and Horne et al. 2021).

4.1.8 Two distinct subpopulations within the ExE-like cluster

The ExE-like cluster exhibited two transcriptionally diverging subpopulations (**Figure 17A, C**). Id2 and Igf2 are well-described trophoblast-/placenta-fate marker genes (Sibley et al., 2004; Selesniemi et al., 2016), and were expressed all over the ExE-like cluster, in contrast to the essential marker genes Eomes, Tfap2c, Bmp4, Bmp8b, Hand1, Plet1, and Elf5 which were predominantly found in cells of ExE-like Subcluster 1 (**Figure 17B**). DEG of diverging ExE-Subcluster 1 and 2 were called to further predict the subclusters' respective biological functions. They formed the basis for a GO Term analysis of respective cluster marker genes. For ExE-like Subcluster 1, the highest enrichment scores were described for ’ribonucleoprotein complex biogenesis’, ‘placenta development’, ‘ribosome biogenesis’, ‘embryonic placenta development’, ‘embryonic placenta morphogenesis’, and ‘reproductive system development’. In contrast, ExE-like Subcluster 2 showed the highest enrichment scores for ‘negative regulation of neurogenesis’, ‘negative regulation of cell development’, ‘negative regulation of nervous system development’, ‘ossification’, and ‘regulation of actin-filament-based process’ (**Figure 18A**).

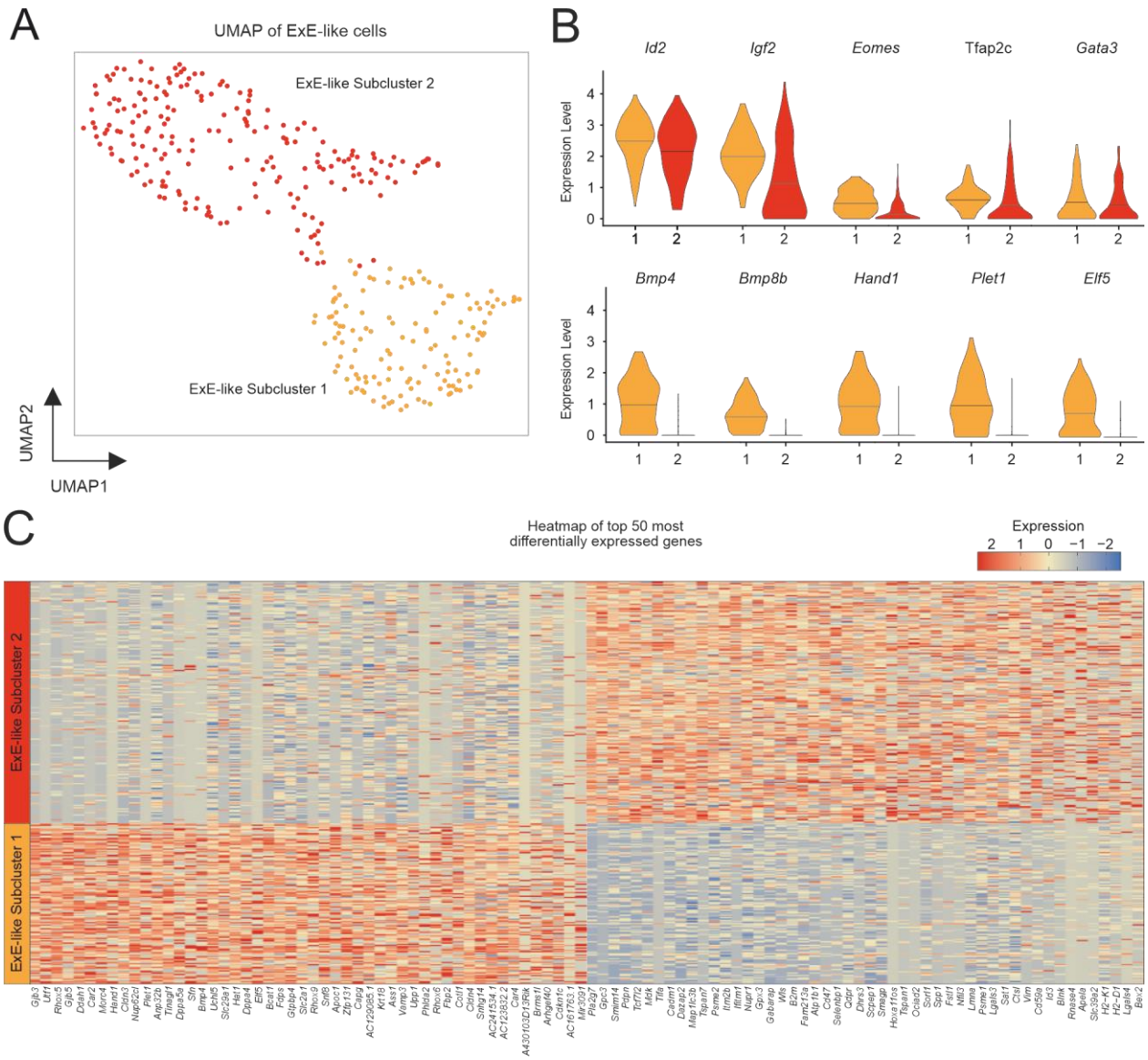

Figure 17. Bipartite transcriptional character of cells comprising the ExE-like cluster

A UMAP representation reveals two transcriptionally diverging subclusters for the ExE-like cluster. **B** Violin plots show expression of trophoblast marker genes. The plots display cells with an expression >0 (line represents the mean of cells). **C** Heatmap depicts the top 50 differentially expressed genes of the two ExE-Subclusters. (Modified from Langkabel and Horne et al. 2021).

These two different enrichment results suggest two diverging biological characteristics and have been proposed in early murine embryos that gradually diversify according to

their position within the ExE (Donnison et al., 2015). The ExE cells close to the EPI are therefore referred to as proximal ExE (PrExE), while ExE cells lining the ectoplacental cone are termed distal EXE (DiExE) (Donnison et al., 2015). To explore this subdivision of the ExE-like compartment of RtL-embryoids, the expression patterns of possible signaling proteins of the Epi-like cells were analysed, possibly affecting the development of the ExE-like compartments. For example, FGF signaling is well described to be essential for the proliferation of TSCs and FGF ligands, and receptor expression is highly tissue-specific within developing embryos (Wen et al., 2017; Feldman et al., 1995; Niswander and Martin, 1992; Tanaka et al., 1998). As a prime example of embryonic development and tissue ligand interaction, the embryonic FGF signaling cascade in RtL-embryoids was evaluated (**Figure 18B and Figure 19C**). The expression of *Fgf4* was restricted to the Epi-like cluster, while the expression of corresponding receptor Fgfr2 was primarily observed in Subcluster 1 of the ExE-like cluster. TSC genes downstream of FGFR2, like *Cdx2*, *Eomes*, *Esrrb*, and *Elf5*, were also observed to be expressed within Subcluster 1 of the ExE-like compartment, with an expression of *Eomes* and *Elf5* being primarily restricted to this subcluster, thereby again mirroring the situation in murine embryonic development (Ciruna and Rossant, 1999) (**Figure 18C**). In murine embryogenesis, *Fgfr2* and *Eomes* are expressed in the ExE-cells close to the EPI and downregulated in the direction of the ectoplacental cone (Ciruna and Rossant, 1999; Haffner-Krausz et al., 1999). Thus, the ExE-Subcluster 1 might be the stem cell niche inside the ExE-like compartment adjacent to the Epi-like compartment (PrExE-like cluster). At the same time, ExE-Subcluster 2 represents more differentiated cell fates, resembling DiExE of the RtL-embryoids.

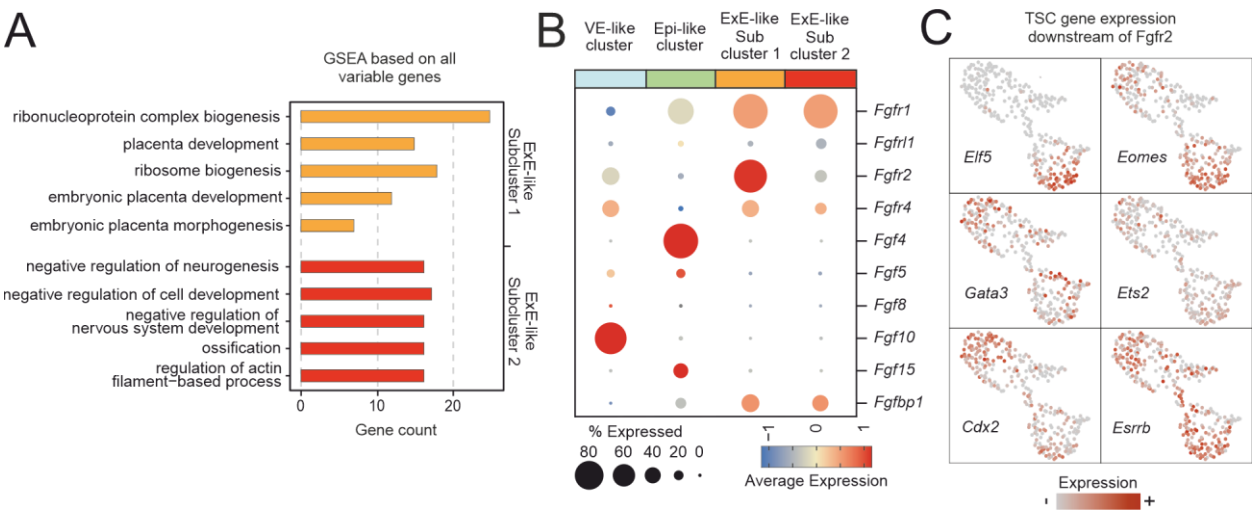

Figure 18. FGF4 expression and downstream target expression in the ExE-like clusters

A GO Term analysis based on all variable genes of ExE-like subclusters revealed diverging biological functions of the two subclusters. **B** Dotplot displaying FGF-receptor and ligand expressing cells throughout VE-, Epi-, and ExE-like (Sub)clusters. **C** Feature plots depict the expression of FGF4 downstream signaling targets within the ExE-like cluster. (Modified from Langkabel and Horne et al. 2021).

To elucidate the stem cell character of ExE-Subcluster 1, the well-described proliferation-associated transcripts and cell cycle stage conditions of cells in the ExE-like subclusters were analysed. The proliferation-associated transcripts *Pcna*, *Top2a*, *Mcm6*, and *Mki67*, were highly expressed within most of the cells in the ExE-like cluster 1, in direct comparison with the low expression of these transcripts in subcluster 2 (**Figure 19D**). Additionally, highly comparable expression patterns with the iTSCs in FGF4/Heparin medium for each proliferation marker were observed, stressing the stem cell characteristics of the ExE-like cluster1. In contrast, ExE-Subcluster 2 displayed a wider distribution of proliferation-associated transcripts, ranging from cells expressing proliferation markers *Pcna*, *Top2a*, *Mcm6*, and *Mki67* were not detectable cells showing comparable expression levels as ExE-like Subcluster 1 (**Figure 19D**). Seurat's cell-cycle scoring and regression method was used to dig deeper into the cell cycle stage distribution. Cells within ExE-Subcluster 2 were observed in the G1 (46.04 %) phase, and fewer cells in the S- (25.24 %) and G2M- (28.71 %) phases, revealing the reduced self-

renewal capacity and expanded differentiation state (**Figure 19E**) (Butler et al., 2018; Nestorowa et al., 2016). This stem cell niche and differentiation hypothesis of ExE-like subcluster 1 and ExE-like subcluster 2 are supported by the expression of *Id2*, which is an essential regulator of placental differentiation. Furthermore, it is found to be expressed in both ExE-like Subclusters, even though at higher levels in most of the cells in ExE-Subcluster 1, as is the case for proliferative TSCs, and lower levels in ExE-Subcluster 2, as expected for cells undergoing differentiation into lineage-specific trophoblast subtypes (Selesniemi et al., 2016) (**Figure 17B**). The natural ExE compartment is spatiotemporally organized via the RAS-MAPK pathway. Therefore the phosphorylation state of the ERK was analyzed because pERK can be used as an indicator of an active RAS-MAPK pathway (Corson et al., 2003). At E5.5, pERK can be found throughout the ExE and the distally developing ectoplacental cone and then become constrained to a ring in the proximal region of the ExE from E6.5 to E7.5 (Corson et al., 2003). At this stage, RAS-MAPK signaling is initiated either FGFR dependent (in the PrExE lining the Epi) or FGFR independent (in the DiExE and the developing ectoplacental cone) (Corson et al., 2003). IF staining selective for phosphorylated ERK showed the presumed gradient of differentiation, as the most active phosphorylated ERK was observed in the most distal region of the ExE-like compartment in RtL-embryoids, which reminds us of FGFR independent RAS-MAPK signaling in the ectoplacental cone developing from the DiExE at E6.0 (Corson et al., 2003; Lin et al., 2016) (**Figure 19B**). Also, pERK was observed in ExE-like cells adjacent to the epi-like compartment. This situation is comparable to the FGFR-related RAS-MAPK signaling in the PreExE (**Figure 19B**). In principle, MAPK phosphorylation within the ExE-like compartment showed a pattern with a clear pERK signal at the most distal position within the ExE-like compartment and weaker activity in the ExE-like cells adjacent to the Epi-like compartment (**Figure 19B**) or a more diffuse distribution spanning the whole ExE-like compartment (**Figure 15B**).

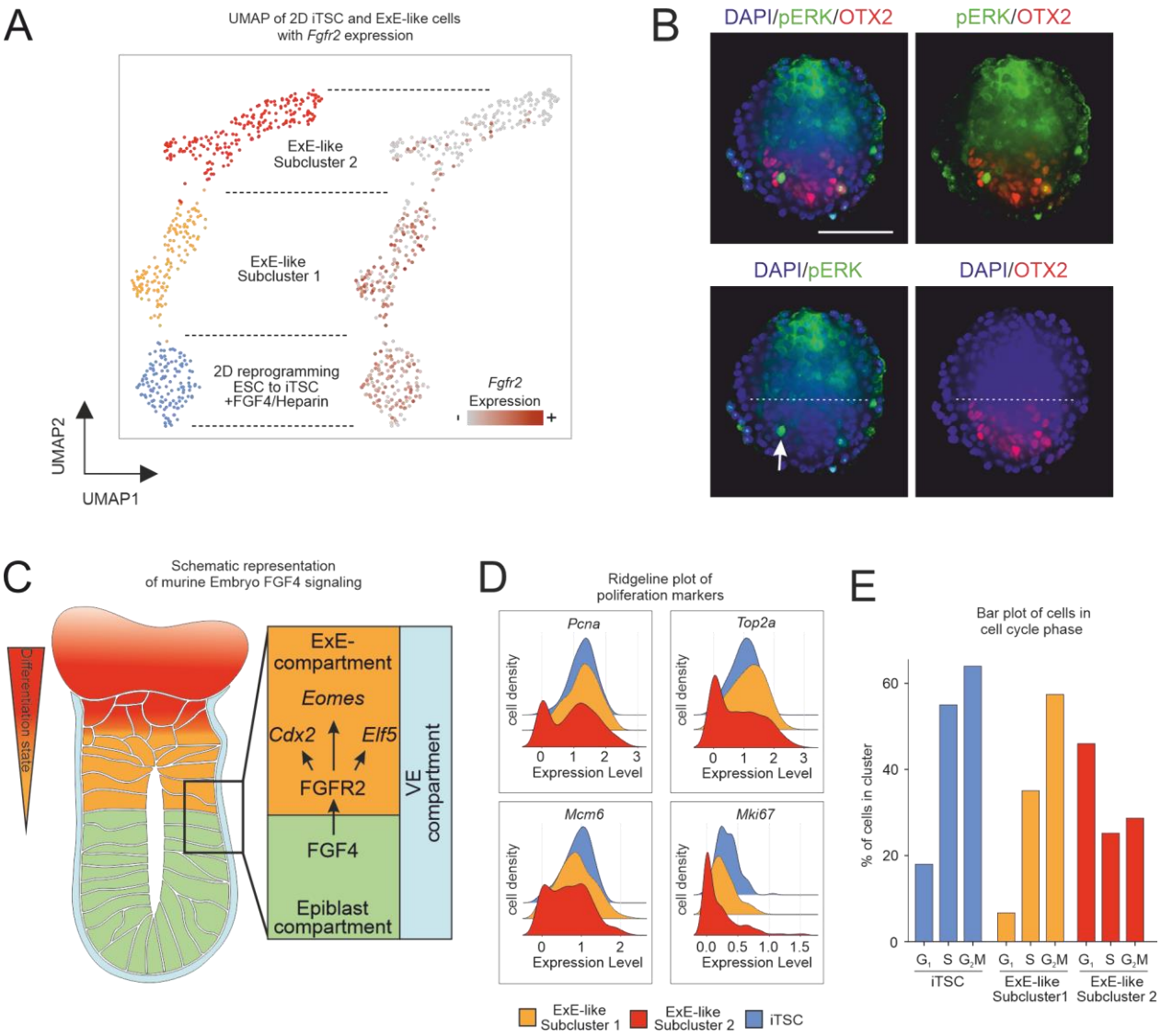

Figure 19. FGF4 signalling and early ExE-like cluster differentiation

A UMAP representation of iTSCs obtained from reprogramming in FGF4/Heparin, supplemented 2D mono-culture, shows close clustering of iTSCs, and ExE-like Subcluster 1 displays a high expression of the FGF4 receptor *Fgfr2*. **B** IF staining against pERK showed the most intense pERK activity in the distal part of the ExE-like compartment. Scale bar = 100 µm; White arrow indicates pERK^{+} cell in Epi-like compartment; Dotted lines represent the border of Epi- and ExE-like compartments. OTX2, red; pERK, green; DAPI, blue. **C** Schematic representation of FGF4 signaling and downstream targets in ExE compartment in murine embryos ~E5.5. **D** Ridgeline plots of proliferation marker gene expression in the two ExE-like Subcluster and iTSCs obtained from FGF4/Heparin supplemented reprogramming in 2D mono-culture, highlighting the stem cell character

ExE-like Subcluster 1. **E** Bar plots displaying the distribution of cell cycle phases in ExE-like Subcluster 1, 2, and iTSCs, as assessed by Nestorowa et al., confirming stem cell characteristics of ExE-like Subcluster 1 and differentiating character of ExE-like Subcluster 2. Experiments were repeated independently at least three times with similar results (B). (Modified from Langkabel and Horne et al. 2021).

Consequently, spatiotemporal patterns of RAS-MAPK signalling in the ExE-like compartment are comparable to RAS-MAPK signalling patterns in murine embryos between E5.5 and E6.5. To further describe the two ExE-like subclusters, the transcriptional profiles were compared with the 2D mono-culture induced iTSC derived under FGF4/Heparin supplementation. The comparison revealed close clustering of 2D iTSCs with ExE-like Subcluster 1 in the UMAP, which displayed high expression of *Fgfr2* (**Figure 19A**). Additionally, 2D iTSCs and cells of ExE-like Subcluster 1 displayed similar distributions of cell cycle phases, highlighting the stem cell character of this subcluster (**Figure 19D, E**).

4.1.9 Nichnet predicted ligand-receptor interactions in RtL-embryoids

The Next step was to identify the signalling interactions between the three main compartments of RtL-embryoids after FGF4 signalling was observed, indicating a complex signalling interaction. The NicheNet algorithm was used to predict ligand-receptor interactions and the subsequent gene expression by merging annotated scRNA-seq data with current knowledge on signaling and gene regulation (**Figure 20**). The top 6 ligands predicted to exert the highest activity within the VE-like compartment (receiver compartment) were *Bmp4*, *Bmp7*, *Itgb7*, *Nectin1*, *Col4a1*, and *Gdf3* (**Figure 20**). VE-like cells express genes encoding for central BMP4 and BMP7 receptors like *Acvr1*, *Acvr2a*, and *Bmpr2*. Our analysis also revealed that *Bmp4* and *Bmp7* are mainly expressed and possibly secreted by the ExE-like compartment, which would serve as the sender compartment (**Figure 20**). Considering the known importance of BMP signalling for induction and migration of the AVE and PGC specification, it can be assumed that Smad signaling exists and is active in RtL-embryoids. The detection of *Gdf3* among the top 6

ligands, which display the highest activity in the VE-like cluster, further supports this notion, which is a critical regulatory component controlling AVE formation.

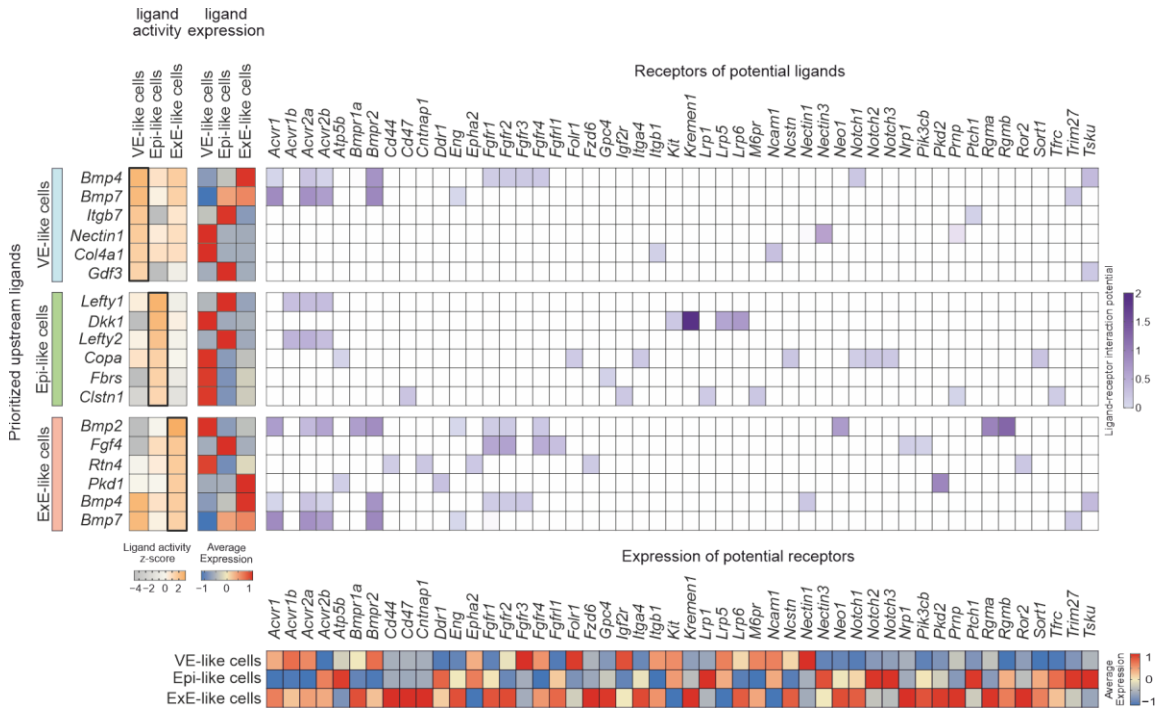

Figure 20. Ligand activity and potential receptor expression of major compartments in RtL-embryoids

Prioritized upstream ligands from all embryo-like compartments (left panel) based on the interaction with all other cells and their average expression (middle panel); In the right panel are potential receptors expressed by the corresponding compartment and (bottom) their average expression. (Modified from Langkabel and Horne et al. 2021).

Further, these data strengthen our observation of PGC specification within cells of the Epi-like cluster, as BMP signaling mediated by *Acvr1* (ALK2) in the VE is known to be essential for the differentiation of PGCs in mouse embryos. In a second phase, the target genes for the top 6 ligands in the individual compartments were predicted (**Figure 21**). This prediction underlined the critical intersection in the VE-like cells between BMP-induced and potential GDF3-induced target genes like *Dkk1*, *Elf3*, and *Gata4*.

The top 6 predicted ligands for the Epi-like compartment were *Lefty1, Dkk1, Lefty2, Copa, Fbrs,* and *Clstn1* (**Figure 20**). LEFTY1 and LEFTY2 inhibit Nodal activity in the EPI by indirect interaction with the Nodal receptors ACVR1B, ACVR2B and antagonizing EGF-CFC co-receptors (Cheng et al., 2004; Chen and Shen, 2004). In the dataset, the highest ligand-receptor interaction potential was observed by *Lefty1* and *Lefty2* with *Acvr1b, Acvr2a*, and *Acvr2b*, of which *Acvr2b* exhibited high gene expression within cells of the EPI-like cluster (**Figure 20**). Consequently, it can be expected that LEFTY1 and LEFTY2 signaling within RtL-embryoids mirrors the condition in murine embryos. DKK1 has been shown to inhibit Wnt/beta-catenin signaling by binding to and antagonizing LRP5/6, presumably by functionally cooperating with high-affinity DKK1 receptors KREMEN1 and KREMEN2 (Mao et al., 2002). Furthermore, *Dkk1* expression has been demonstrated to be initiated in the mature PE starting around E4.5 (Neagu et al., 2020; Hoshino et al., 2015) and was proposed to indicate the completion of PrE maturation, repressing WNT signaling and allowing for Otx2 induction, rosette formation, and pluripotency progression (Neagu et al., 2020). Within RtL-embryoids, it was possible to identify *Dkk1* (originating from the VE-like cluster) as the second most active ligand in cells of the Epi-like cluster, showing high interaction potential with receptors *Lrp5 and Lrp6* and very high interaction potential with *Kremen1*. *Lrp5* was expressed in the EPI-like cluster, while the expression of Kremen1, encoding for its receptor, was identified as well at low rates. These results reveal that the DKK1-mediated Wnt/beta-catenin inhibiting cascade is present in RtL-embryoids, as described for natural murine embryos. Among the predicted target genes under the control of *Lefty1*, *Dkk1* and *Lefty2* are Pou5f1 and Sox2, which are crucially involved in the self-renewal and pluripotency, of ICM and EPI (**Figure 21**). The ligands display the highest activity scores within the ExE-like cluster, including *Bmp2, Bmp4, and Bmp7*. *Bmp2 and Bmp4* have been shown to participate in placental development (Goldman et al., 2009), as BMP7 functions predominantly as a heterodimer with BMP2 or BMP4 during mammalian embryogenesis (Kim et al., 2019). In RtL-embryoids, these signaling pathways seem to be present as well. Additionally, the gene encoding for their receptor, *Bmpr1a*, is highly expressed in cells of the ExE-like cluster (**Figure 20**) (Miyazono et al., 2005). NicheNet analysis also uncovered *Pkd1* as one of the highly active ligands acting on the ExE-like cluster, while the gene encoding for its receptor Pkd2

was also highly expressed in cells of the ExE-like cluster. The interaction of PKD1 and its receptor PKD2 is necessary for placental morphogenesis (Garcia-Gonzalez et al., 2010). This signaling cascade of mammalian embryogenesis is represented in RtL-embryoids. Additionally, it was shown that among the downstream targets of the ExE-like cluster are *Cdx2* and *Gata3*, which are essential for TSCs and placental development (**Figure 21**). To sum up, NicheNet analysis highlighted that the communication between the three primary embryonic clusters in RtL-embryoids resembles major pathways previously defined to be involved in natural murine embryo development.

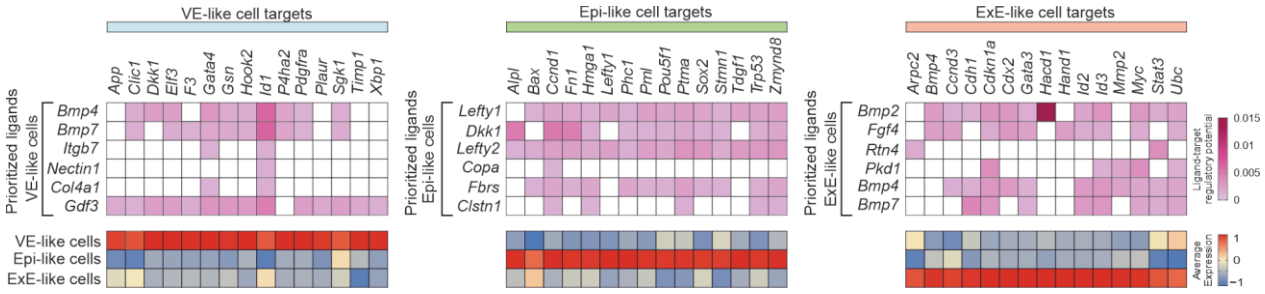

Figure 21. Prioritized ligands and their potential target genes in RtL-embryoids

Potential target genes of the prioritized upstream ligands and their average expression on the bottom panel are in the top panel. (Modified from Langkabel and Horne et al. 2021).

4.2 Result section of scRNA-seq analysis for the G6PI-induced arthritis

The following section used SCO to characterise sparse cell types in the joint under pathophysiological conditions with the G6PI T-reg depletion model (Bockermann et al., 2005; Frey et al., 2010). As a result, it was possible to identify single cells in homeostasis and their individual activation states. Further, transcriptional and spatial gradients were observed in homeostasis, acute inflammation, chronification, and remission.

4.2.1 The shift from acute into chronic inflammation in G6PI-induced arthritis

The aetiology of RA is different regarding genetic and environmental determinants of the disease (Kaartinen et al., 1999). T-cells are thought to cause effector cells to mediate a synovitis response and damage cartilage and bone. These effector cells consist of B-cells, monocyte/macrophages, mesenchymal cells, neutrophils, and mast cells. Furthermore, these cells introduce and sustain a network of cytokines and proinflammatory mediators. Studies reported that arthritis-susceptible wild-type mouse strains develop severe peripheral symmetrical polyarthritis with a high incidence (>95%) after immunization with G6PI (Schumacher et al., 1999; Bockermann et al., 2005; Bruns et al., 2009).

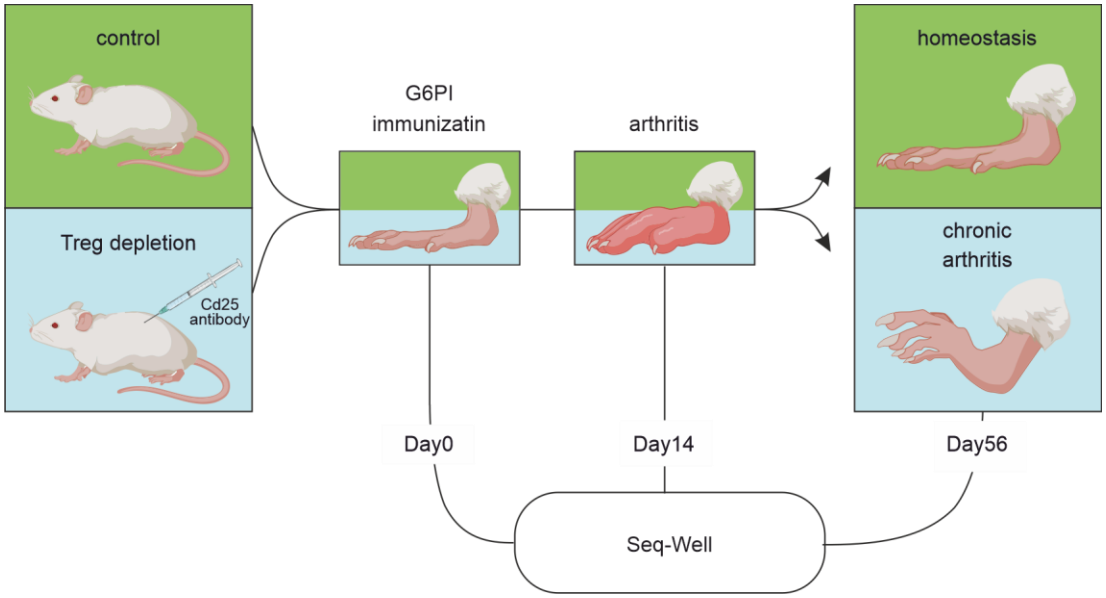

Figure 22. G6PI-T-reg depletion model to perform Seq-Well at three different time points

The initial samples were collected before the injection of G6PI. The following sampling time point was 14 days after immunization, which marked the peak of arthritic inflammation in both groups of the model. The final time point was 56 days after immunization, which was the endpoint of the experiment. By day 56, mice in the group that received only G6PI had entered complete remission, while mice in the group that received G6PI-T-reg depletion showed chronic arthritic symptoms. Synovial joint cells were isolated and loaded onto Seq-Well on day 0, day 14, and day 56.

The experiment was designed with two groups: one group underwent Cd25 T-reg depletion while the other did not. hen T-regs were depleted, severe arthritis persisted. However, in the mice of the G6PI exclusive model, arthritis started to resolve three weeks after immunization (Frey et al., 2010; Schubert et al., 2004) (**Figure 22**). Sampling started right before G6PI immunization (day 0). The following sampling time point was 14 days post-immunization, marking the peak of ArInf in both models. The last time point was 56 days post-immunization, indicating the experiment's endpoint. On day 56, the mice without injection of the Cd25 antibody went into total remission. In contrast, mice with the Cd25 injection 8 days before immunization with G6PI showed chronification of the arthritic symptoms. Samples from the G6PI-T-reg depletion models were analyzed using scRNA-seq (Seq-Well) to gain insights into the dynamic changes in cellular components during inflammation, as well as during remission (in the G6PI group) and chronification (in the Treg depletion group).

4.2.2 Clustering and cell-type annotation of G6PI-induced arthritis dataset

After the Seq-Well protocol, library preparation, and sequencing, the resulting sequencing data were de-multiplexed (bcl2fastq2, v2.20) and then aligned using STAR aligner (v1.6.2), and 1,536,148 cellular barcodes were detected (see method section for detailed Seq-Well protocol, library preparation, sequencing, and raw data processing). Applying stringent quality criteria (see method section for detailed filtering steps 3.3.7), a total of 33.636 cells were identified. The resulting single-cell data was LogNormalized (Seurat

function), and genes with the highest cell-to-cell variability were determined (FindVariableFeatures). Data were scaled (ScaleData, function), and the dimensionality was reduced to 10 PCs for calculating the UMAP (RunUMAP function). The UMAP uncovered six distinct cell clusters (**Figure 23A**).

Next, a comparable number of genes per cell, uniquely aligned genetic reads, and mitochondrial gene fractions were detected between the cell clusters (**Figure 23B - D**). Cell type annotation was performed via marker gene expression for every cellular cluster. Mesenchymal cells in (cluster 1) expressed high levels of marker genes for cells with mesenchymal origin in joints like SFs and CCs (*Gsn*, *Dcn*, *Prg4*, *Apod*, *Comp*) (Aidinis et al., 2005; Dodge et al., 1998; Wei et al., 2020; Tew et al., 2007; Hedbom et al., 1992) (**Figure 23E**). Cluster 2 showed very high expression of Lyz2, Cd74, and H2-Ab1, which classified them as macrophages (Faust et al., 2000). Endothelial cells (cluster 3) were characterized by high expression of Sele, Fabp4, Selp, and Pecam1 (Harjes et al., 2017; Liu et al., 2015; Leeuwenberg et al., 1992). Cluster 4 was characterized by the expression of (*Ngp*, *Elane*, *Camp*, *S100a9*, and *S100a8*) indicating that these cells are neutrophils (Garg et al., 2020; Gombart et al., 2003; Nizet et al., 2001). Various keratins and keratin-associated proteins (*Krt10*, *Lgals7*, *Krtdap*, *Krt2*, and *Krt1*) were expressed in epithelial cells (cluster 5) (Bazzi et al., 2007). Mast cells (cluster 6) expressed high levels of *Cma1*, *Cpa3*, and *Mcpt4,* which are previously described marker genes for these cells (Akula et al., 2020). Lower cell numbers at the later time points within this experiment were observed in both experimental conditions and could be explained by variances in cell numbers loaded on the Seq-Well (**Figure 23F**). The relative increase in macrophages, endothelial, and granulocyte fractions on day 14 after G6PI immunization in both experimental conditions is consistent with previous findings in other arthritis animal models (Asquith et al., 2009; Komatsu and Takayanagi, 2012; Trentham et al., 1978). Infiltration of myeloid cells at day 56 in the T-reg-depleted condition was not observable at day 56 in the G6PI exclusive group, which hints toward a chronification after T-reg depletion (Frey et al., 2010). The UMAP was split by experimental sampling timepoint and condition, showing a shift in the Macrophage cluster (cluster 2) and Mesenchymal cells (cluster 1), indicating transcriptional variation within the clusters. The most distinct shift was observed between day 0 and 14, independent of T-reg depletion. However, the

mesenchymal cell cluster (cluster 1) showed the same shift between the T-reg-depleted groups on day 56 as on day 14, which was not observed in G6PI exclusive group (**Figure 23G**).

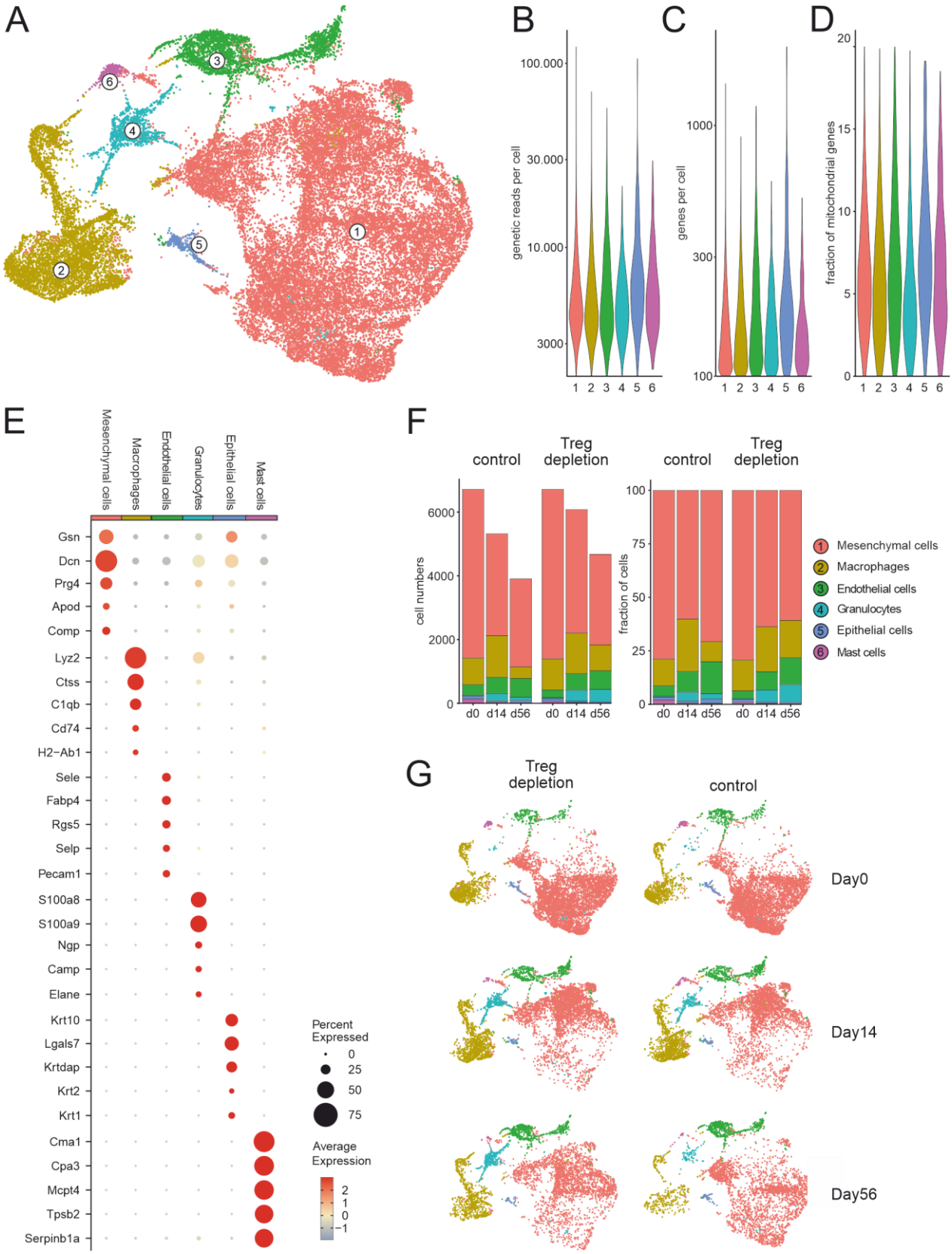
A
B
C
D
genetic reads per cell
genes per cell
fraction of mitochondrial genes
E
Mesenchymal cells
Macrophages
Endothelial cells
Granulocytes
Epithelial cells
Mast cells
Gsn
Dcn
Prg4
Apod
Comp
Lyz2
Ctss
C1qb
Cd74
H2−Ab1
Sele
Fabp4
Rgs5
Selp
Pecam1
S100a8
S100a9
Ngp
Camp
Elane
Krt10
Lgals7
Krtdap
Krt2
Krt1
Cma1
Cpa3
Mcpt4
Tpsb2
Serpinb1a
Percent Expressed
Average Expression
F
control
Treg depletion
cell numbers
fraction of cells
d0 d14 d56
G
Treg depletion
control
Day0
Day14
Day56

Figure 23. Seq-Well scRNA-seq dataset of G6PI-T-reg depletion model

A UMAP representation of scRNA-seq results showing 6 distinct transcriptomic clusters. **B - D** Genetic reads per cell-, genes per cell-, fraction of mitochondrial genes resolved according to cellular clusters. **E** Dot Plot showing expression of top 5 most differentially expressed genes per cluster in the G6PI induced arthritic dataset. **F** Cell numbers and Fraction of cells resolved according to cell clusters. **G** UMAP representation of scRNA-seq results resolved according to sampling time point and T-reg-depleted condition.

4.2.3 Mesenchymal subcluster identification

After the sub-clustering of the mesenchymal cells, 4 different cell clusters were identified (**Figure 24A**). To identify the resulting groups of cells, signatures from Friščić et al. were utilized for a signature enrichment analysis (Friščić et al., 2021). As a result, clear enrichment for the CC signature in cluster 1 was observed, the SLFs signature enriched comparable high in cluster 2 and 3, and the LLFs enriched in cluster 4 (**Figure 24B**). Therefore, the cell clusters were named according to the highest enrichment.

The 5 most significant genes were plotted in each cluster (**Figure 24C**), and *Angptl7*, *Fmod*, *Clu*, *Chad*, and *Spp1* were the most significant in the CC cluster. *Angptl7* is involved in the formation and organization of the ECM, acts as a negative regulator of angiogenesis in the cornea, and plays a significant role in maintaining corneal avascularity (Comes et al., 2011; Toyono et al., 2015). Both functions are needed in healthy cartilaginous tissue. Fmod codes for the protein Fibromodulin organizing the ECM and regulating collagen fibrillogenesis (Chen et al., 2010). Clusterin encoded by Clu functions as an extracellular chaperone that prevents the aggregation of non-native proteins in tissue (Greene et al., 2011). Chondroadherin promotes the attachment of CCs, fibroblasts, and osteoblasts. This binding is mediated (at least for CCs and fibroblasts) by the integrin α2β1. It may play an essential role in regulating CC growth and proliferation, and its transcript *Chad* is one of the most significant genes among CCs. The last of the 5 most significant genes in CCs was *Spp1,* coding for the significant non-collagenous bone protein Osteopontin that binds tightly to hydroxyapatite (major bone mineral). It appears

to form an integral part of the mineralized matrix (Kaartinen et al., 1999). However, it is known that CCs of the deep zone cartilage express osteopontin to ensure the connection between the bone tissue and cartilage (Pullig et al., 2000). The Synovial sublining layer fibroblast clusters 1 and 2 highly express *Apod* and *Mmp13*, common markers for sublining layer cells (Croft et al., 2019; Friščić et al., 2021; Mizoguchi et al., 2018). The last cell cluster expresses common LLFs markers like *Prg4*, *Htra1*, and *Clic5* (Croft et al., 2019; Zhang et al., 2019a; Stephenson et al., 2018). These findings revealed that the mesenchymal cells contain all connective tissue and ECM-producing cell types of the joint.

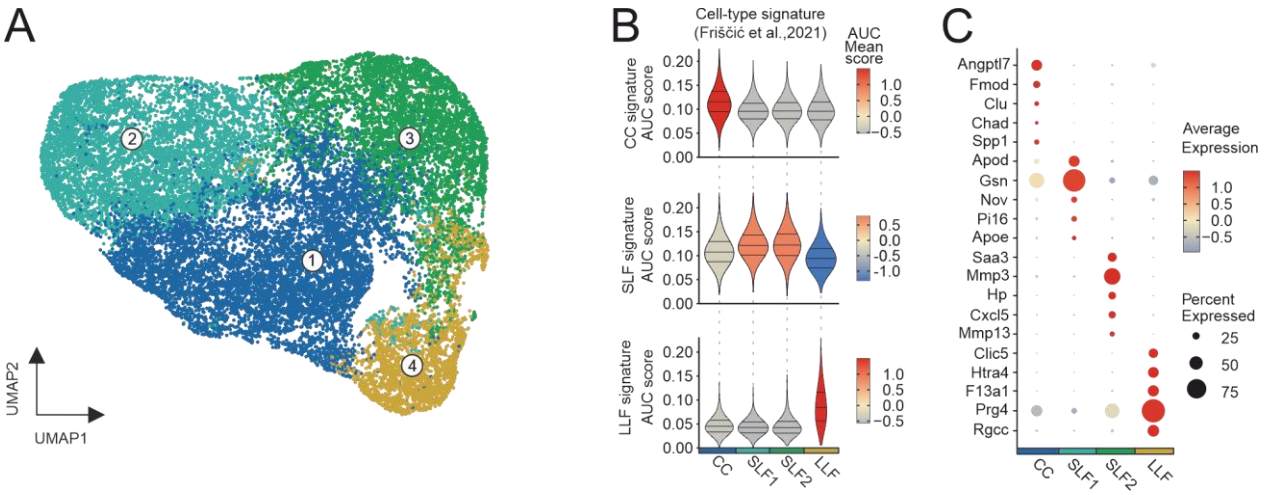

Figure 24. Mesenchymal sub-cluster identification

A UMAP representation reveals 4 transcriptionally diverging subclusters for the mesenchymal cells (chondrocytes (CC), sublining layer fibroblasts 1 (SLF1), sublining layer fibroblast (SLF2), lining layer fibroblasts (LLF)). **B** AUCell-based enrichment scores (AUC scores) show a similarity of gene expression signatures of CC, healthy SLF, activated SLF, and LLF clusters compared to scRNA-seq signatures published by Friščić et al., **C** Dot Plot showing expression of the top 5 most differentially expressed genes per cluster in the mesenchymal cells sub-cluster (log-fold change 1.5; FDR $p < 0.05$).

4.2.4 Acute inflammatory states of mesenchymal cells

After classifying mesenchymal subclusters, the cell cluster was split by time and T-reg depletion (**Figure 25A**). In the separated UMAP, no significant differences were observed on day 0 between the control and T-reg-depleted condition. However, it was interesting that the SLFs at day 0 consist nearly exclusively of SLF1. Also, on day 14, no significant difference between control and T-reg-depleted condition was detected, representing the highest acute inflammation. Nevertheless, the key difference compared to day 0 is again the synovial sublining layer cells which nearly exclusively includes cells of the SLF2.

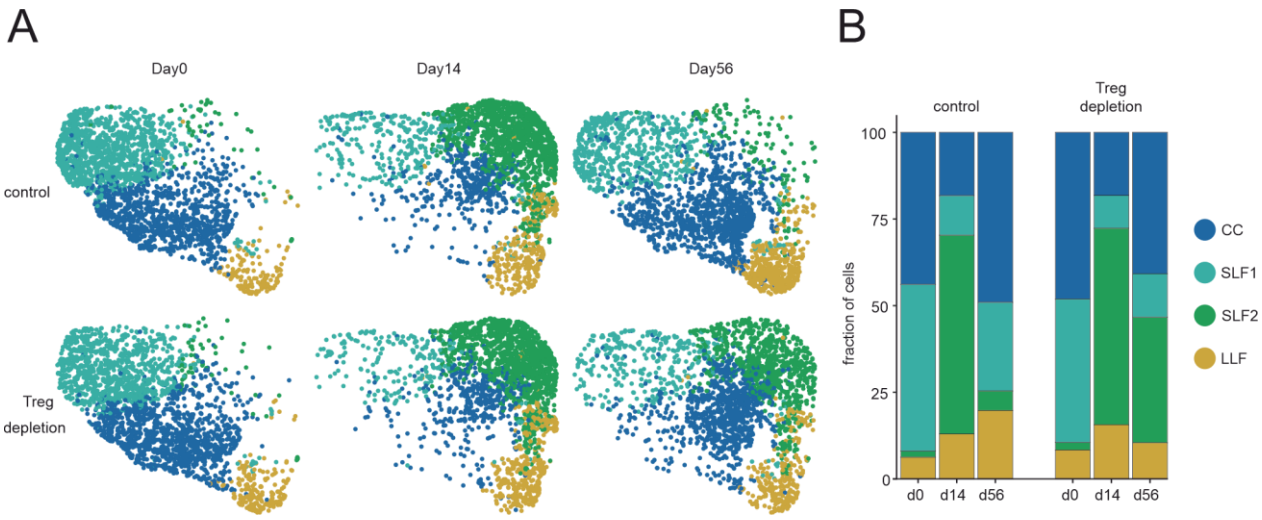

Figure 25. Mesenchymal sub-cluster in acute and chronic arthritic inflammation

A UMAP representation of mesenchymal cells (chondrocytes (CC), sublining layer fibroblasts (SLF1), sublining layer fibroblast (SLF2), lining layer fibroblasts (LLF)) resolved according to sampling time point, and T-reg-depleted condition. **B** Fraction of mesenchymal cells resolved according to cellular clusters (Figure legend in B applies to the entire figure).

Additionally, a substantial shift in the CC and LLF compartment was observed. On day 56, the most significant difference between the control and the T-reg-depleted condition was seen. The control cells of the mesenchymal subcluster at day 56 exhibited a tendency towards the day 0 state, which represents the homeostasis of cells within the murine joint.

However, this was not observed in the T-reg-depleted condition on day 56. These cells showed a comparable cluster formation and cell distribution as observed on day 14, indicating that the depletion of T-reg cells disrupted the normal cellular homeostasis within the joint. This indicates a chronification of the inflammatory response in the cells of the Treg-depleted conditions. This finding is in line with studies that used this experimental arthritis model (Frey et al., 2010; Schubert et al., 2004). This inflammatory and chronification response was also observed in the cellular fractions of mesenchymal cells. On day 0, the SLFs compartment consists exclusively of the SLF1 subcluster in both conditions (**Figure 25B**). This SLF subcluster distribution is reversed on day 14, where SLF2 cells are the primary cell type in the SLF compartment. With this specific association of SLF1 and SLF2 to the inflammatory state of the synovium, therefore SLF1 were termed healthy SLFs (hSLFs), and SLF2 activated SLFs (aSLFs).

Additionally, over time, a substantial reduction in CCs and an increased LLF fraction were observed. These changes from day 0 to day 14 were partially restored at day 56 in the control condition, except for the LLF fraction, which remained overrepresented compared to day 0 and day 15. Again, the T-reg-depleted condition at day 56 showed an equal fraction distribution to day 14, indicating that the depletion of T-reg cells leads to a chronic inflammatory response in the joint, as the cellular distribution and fraction remain unchanged.

To get insights into the acute inflammatory state for CCs, SLFs, and LLFs, the DEGs for each cell type between day 0 as a ground state and day 14 as the day of highest acute inflammation were called (**Figure 26**). When the top 20 DEGs were plotted for each mesenchymal cell type for all time points, the first noticeable pattern observed was that the acute-gene signatures were cleared in the control state but persisted in the chronic state. This observation suggests that the chronic inflammatory response is characterized by the sustained activation of genes associated with acute inflammation. This finding is in line with the previous studies (Frey et al., 2010; Schubert et al., 2004). The acute inflammatory response gene signature exhibited a variety of collagens (*Col1a1*, *Col1a2*, *Col3a1*, *Col5a2*, *Col5a3*, and *Col12a1*) and matrix metalloproteases (MMP) (*Timp1*, *Mmp3*, *Mmp13*, and *Mmp14*) expressed in the Mesenchymal cell clusters. Collagens and MMPs have antagonistic functions in tissues, while collagens like COL1A1 and COL1A2

are one of the key components of the ECM. MMPs are calcium-dependent zinc-containing endopeptidases capable of degrading various ECM proteins (Nagase et al., 2006). The expression of MMPs in SFs is well described in the literature (Kumkumian et al., 1989; Lotz and Guerne, 1991). Also, the expression of MMPs in human has been previously studied (Bell et al., 1999; Cawston et al., 1998; Li and Zafarullah, 1998). However, this study's robust upregulation of collagens in acute and chronic arthritis responses is underrepresented in the literature.

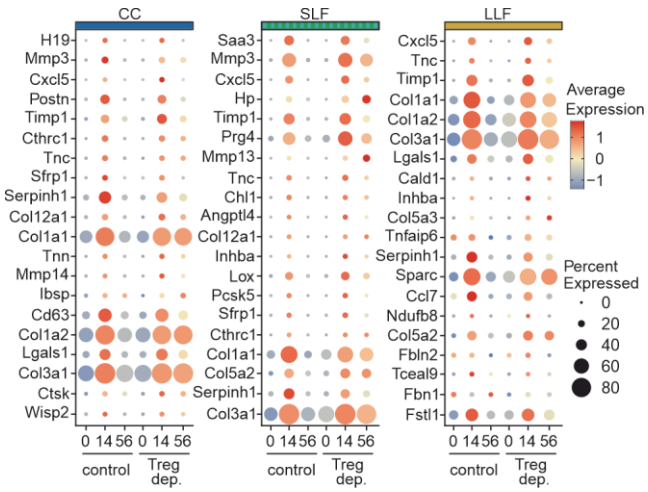

Figure 26. Acute arthritic signatures of mesenchymal cells

Dot Plot showing expression of top 20 most differentially expressed genes in acute arthritic inflammation per cell type in the mesenchymal sub-cluster (chondrocytes (CC), sublining layer fibroblast (SLF), lining layer fibroblasts (LLF)) (log-fold change 1.5; FDR $p < 0.05$).

Further, the chemokine *Cxcl5* is highly expressed in the acute signatures. *Cxcl5* is known for its chemoattraction for neutrophils and angiogenic properties in RA (Koch et al., 2001; Koch et al., 1995; Walz et al., 1991). Functional analysis of the acute inflammatory signatures by GOEA revealed that the CC cluster enriches in the ECM-associated- and CC-specific terms (**Figure 27**). In the GOEA for the acute inflammatory response of the SLFs, ECM-associated terms were observed, and terms associated with cell chemotaxis. In the LLFs, a more diverse set of terms like ‘protein exit from ER’, ‘response to ER stress’, ‘retrograde protein transport’, and ‘ERAD pathway’ were shown, which are all linked to

unfolded protein response (UPR), a complex reaction of cells to stress subsequent of an accumulation of proteins with imperfect folding in the ER. However, the term ‘response to TGF-β’ and ‘cellular response to TGF-β beta stimulus’ were also identified, which implies an essential role of TGF- β in the LLF compartment. ECM-associated terms were also observed in the LLFs.

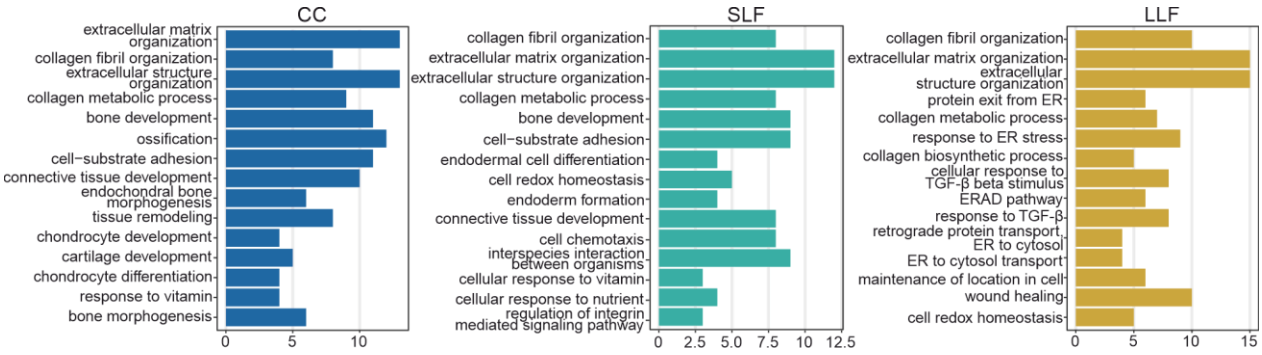

Figure 27. GSEA of acute arthritic signatures

GO term enrichment analysis of all differentially expressed genes (log-fold change 1.5; FDR $p < 0.05$). Statistical test: GO terms were selected from the top sorting by adjusted P-value (p adjusted < 0.05, one-tailed hypergeometric test with Benjamini–Hochberg correction). Bars depict fold enrichment for terms with $p < 0.05$.

4.2.5 Chronic inflammatory states of Fibroblast-like synoviocytes

Homeostatic SFs underwent phenotypic changes in the chronic inflammatory condition, resulting in an aggressive, hyperplastic phenotype. These changes eventually led to pannus formation, which is an abnormal layer of fibrovascular or granulation tissue (O'Neil and Kaplan, 2019). Although long-term drug-free remission indicates that articular immune homeostasis can be reestablished (Alivernini et al., 2017). However, remission mechanisms are poorly characterized. This knowledge has formed in understanding RA's biology due to a lack of sampling from healthy and remission synovium. (Zhang et al., 2019a; Kuo et al., 2019).

The chronic signature for CCs, SLFs, and LLFs was generated by calling the DEGs for each cell cluster between control cells as a ground state and T-reg-depleted condition at day 56 (**Figure 28A**). CCs, SLFs, and LLFs expressed a variety of collagens (*Col1a1*, *Col1a2*, *Col3a1*, *Col5a2*, *Col5a3*, and *Col12a1*) that have a comparable expression pattern as in in the acute inflammatory signature. This upregulation of type I-, type III-, and type V collagens might be a rescue response to the strong MMP expression that cleaves ECM molecules at particular peptide sequences to generate large cavities for the cell to pass through (Lu et al., 2011). Further, MMPs (*Timp1*, *Mmp3*, *Mmp13*, and *Mmp14*) and the chemokine *Cxcl5* in the chronic inflammatory signature were also identified. These findings indicate that the acute- and chronic inflammatory signatures were comparable in the most significantly regulated genes.

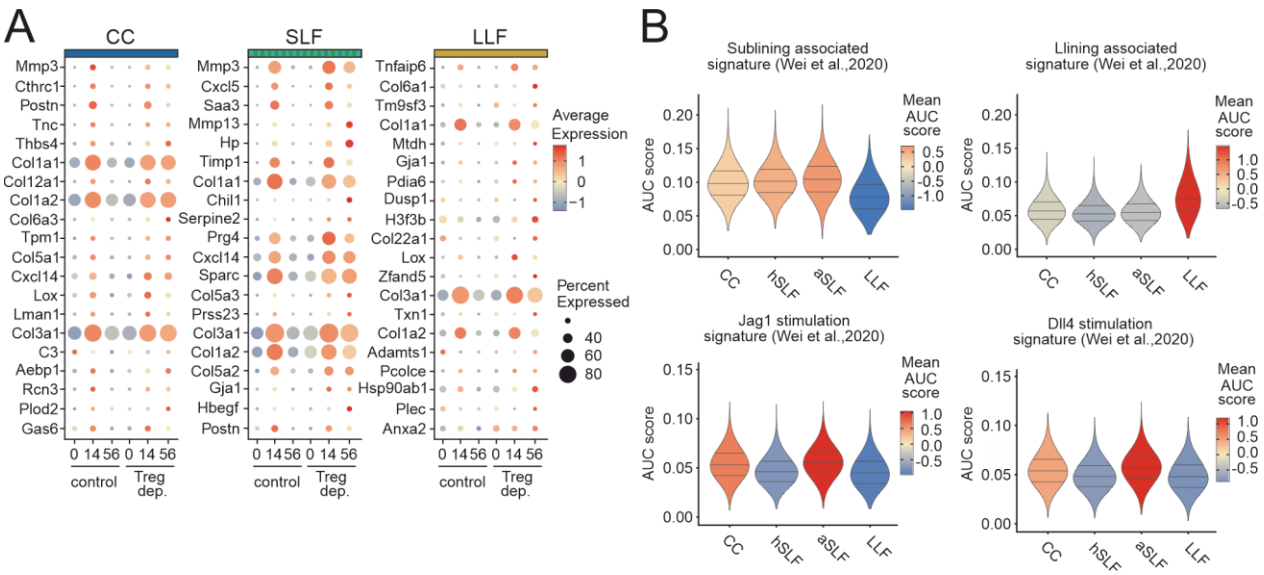

Figure 28. Chronic arthritic signatures mesenchymal cells

A Dot Plot showing expression of the top 20 most differentially expressed genes in chronic arthritic inflammation per cell type in the mesenchymal sub-cluster (chondrocytes (CC), sublining layer fibroblast (SLF), lining layer fibroblasts (LLF)) (log-fold change 1.5; FDR $p < 0.05$). **B** AUCell-based enrichment scores (AUC scores) show a similarity in gene expression signatures of CCs, hSLFs, aSLFs, and LLFs clusters compared to scRNA-seq signatures published by Wei et al. (Jag1-, Dll-, sublining-, lining signature).

It has been recently discovered that the expansion of SLFs is closely linked to the activity of RA disease (Wei et al., 2020). To show this characteristic of SLFs, a sublining- and lining layer signature enrichment analysis was performed to confirm their positional identity combined with a Notch ligand (Jag1 and Dll4) signature enrichment, which is the central regulator of SF identity and stromal crosstalk in the ArInf (Wei et al., 2020). While the sublining signature was enriched in the aSLFs and hSLFs, the lining layer signature was uniquely enriched in the LLFs. However, this result indicates a clear positional identity in the chronic response and a Notch-dependent inflammation (**Figure 28B**) (Wei et al., 2020).

TF-prediction analysis was performed to identify the TFs driving the chronic inflammatory signature in the mesenchymal cells (**Figure 29**). *Atf3* was identified as the most interconnected TF in CCs. ATF3 is known to mature CCs, induces cell cycle exit and terminal differentiation of CCs (James et al., 2006), and modulate the gene expression of MMPs in human CCs (Chan et al., 2017). This finding is consistent with the observation that the CC cluster has a lower cell number and increased expression of MMPs during the acute inflammatory response (**Figure 25B and Figure 26**). The *Creb3* family was also observed in our analysis (*Creb3*, *Creb3l1*, *Creb3l2*). *Creb3* family members control the expression of various genes according to their tissue-specific expression. There are described as endoplasmic reticulum (ER) stress transducers and share sequence similarity with ATF6 (Lu et al., 1997; Kondo et al., 2005; Saito et al., 2009). *Creb3l2* is known for its function in developing cartilage and controlling the secretion of cartilage matrix proteins (Saito et al., 2014; Hino et al., 2014). Our analysis also finds the canonical ER stress TFs *Xbp1* in CCs and SLFs responsible for several developmental processes in professional secretory cells (Glimcher, 2010). In CCs, it controls the mineralization

during endochondral ossification(Cameron et al., 2015). In cultured human synovial fibroblast, the active spliced variant of *XBP1* was overexpressed in RA.

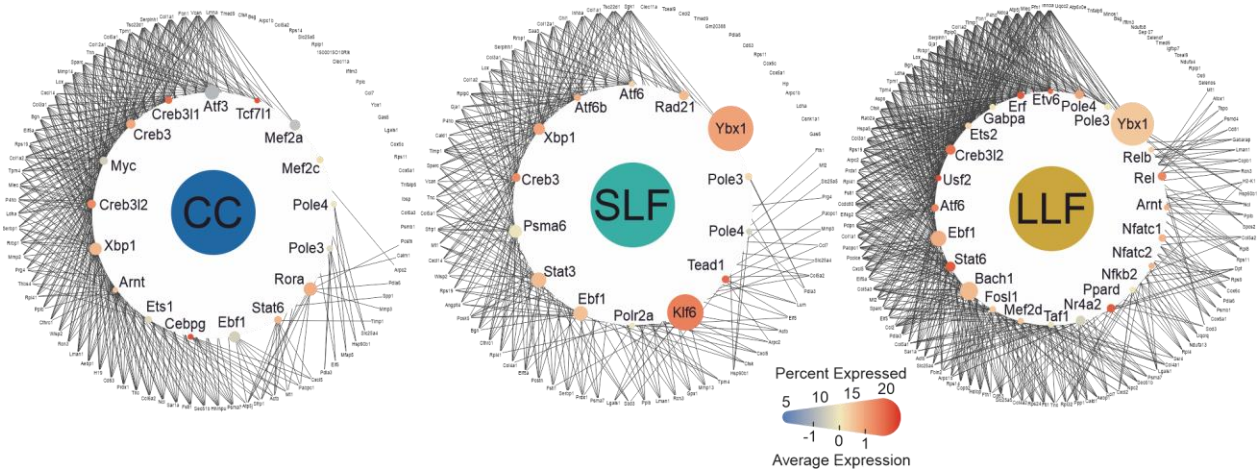

Figure 29. iRegulon transcription factor prediction analysis

Network representation of chronic arthritic signatures and predicted upstream transcriptional regulators for chondrocytes (CC), sublining layer fibroblast (SLF), and lining layer fibroblasts (LLF). Edges: predicted transcriptional regulation. Transcription factors (TFs, inner circle) and predicted target genes (outer circle) are represented as nodes sized and colored according to the scaled expression level across all clusters. Selected TFs and genes are sorted for connectivity counterclockwise.

Additionally, spliced XBP1 is induced in synovial fibroblast upon TNF autocrine stimulation, a potential feedback loop for sustained SF activation in chronic RA (Savic et al., 2014). Next, Stat6 was found upstream of CC and LLF chronic activation signature associated with Il-4 signaling and CC mechanotransduction (Salter et al., 2001). In synovial tissue biopsy specimens from patients with RA, STAT6 expression was relatively heterogeneous compared to control, indicating a homeostatic role in addition to anti-inflammatory effects (Walker et al., 2006). In SLFs, Stat3 works as an upstream regulator that plays an essential role in mediating inflammatory functions (Garbers et al., 2015) in a positive feedback loop that drives the expression of inflammatory cytokines and RANKL, which leads to joint destruction (Mori et al., 2011). In SLFs and LLFs, Atf6 was found, another canonical UPR TF, upstream of the chronic inflammatory signature. ATF6 is an

ER membrane-bound TF, which translocates to the Golgi apparatus upon ER stress, where it is cleaved to its active form by site-1 and site-2 membrane proteases (Kaufman, 1999; Ye et al., 2000). Previous research has linked Atf6 to activating inflammatory mediators, consistent with its role in the chronic inflammatory response (Yoo et al., 2012). Cleaved ATF6 gains in transcriptional activity and raises the expression of Xbp1, which is also upstream of the acute response in SLFs. Another activation TF observed in LLFs is Usf2. This TF is in human SFs described as an essential signaling mediator of TNF activation and controls the expression of receptor tyrosine phosphatase sigma, which is expressed in synovial LLFs and a potential therapeutic target for RA (Svensson et al., 2020)

In summary, within the highly complex network of chronic activation signatures, Creb3 was identified as a potential key regulator in CCs, SLFs, and LLFs. Other pathway-specific TFs, such as ATF3, Atf6, Xbp1, Stat3, and Stat6, were also involved as potential regulators in these cells.

4.2.6 Notch signalling in SFs in acute and chronic ArInf

In RA, Notch target genes were upregulated in SFs upon Notch3 signaling, and the knockout of Notch3 or an unfunctional NOTCH3 signaling pathway reduces inflammation and avoids joint damage in inflammatory arthritis (Wei et al., 2020). A public fibroblast-specific Notch gene signature (Wei et al., 2020) was used to define ligand activation with Jag1 and Dll4 to assess Notch activation in mesenchymal cells at homeostasis, acute and chronic inflammation. The Jag1 and Dll4 gene signatures were enriched in acute inflammatory CCs and SLFs and persisted in the chronification in CCs and LLFs (**Figure 30**). However, the enrichment in LLFs was weaker compared to SLFs. Wei et al. described the importance of Notch3 in the SLF compartment and its central role in disease and revealed that SFs show a positional identity shaped by endothelium-derived Notch signalling (Wei et al., 2020). Therefore, surprisingly, the Notch activation signatures enriched even stronger in acute and chronic inflamed CCs. This finding suggests a similar role of Notch signaling in CCs and expands the finding of Wei et al. that the knockout of

Notch3 or unfunctional NOTCH3 signaling prevents joint damage in inflammatory arthritis not only by the effect on SFs but also on CCs.

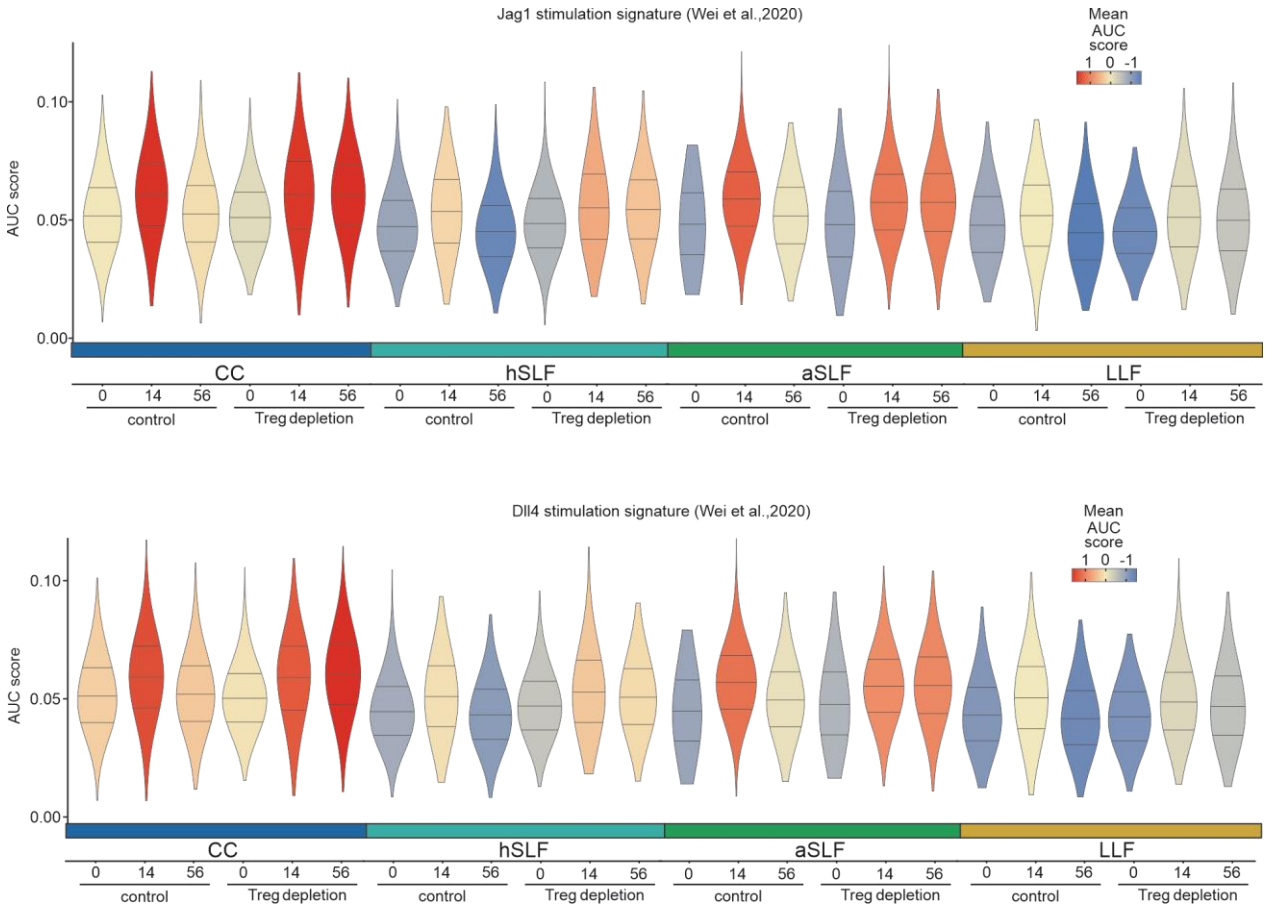

Figure 30. Notch ligands JAG1 and DLL4 signature enrichment in mesenchymal sub-cluster

The AUCell-based enrichment scores (AUC scores) indicate that the gene expression signature enrichment of JAG1 and DLL4 is present in CC, hSLF, aSLF, and LLF. This enrichment was determined by comparing the gene expression signatures to those published by Wei et al. The analysis used samples taken at different time points and under T-reg-depleted conditions.

4.2.7 The bipolar character of the synovial subcluster in chronification and remission

As a next step, the characteristics of the chronic inflammatory reaction were determined. Therefore, the SFs were subsetted at day 56 to isolate the chronic and remission cells of the synovium (**Figure 31**). In the chronification condition, a strong activation pattern of SLFs was observed. However, in our scRNA-seq dataset, the three populations of LLFs, aSLFs, and hSLFs were not separated into distinct clusters but instead appeared to be connected, suggesting the presence of transitional subpopulations. While the intermediate states between hSLFs and aSLFs were part of the activation and inflammation process, the SLF continuum towards LLFs is based on morphological and positional gradients regulated by endothelium-derived Notch signalling (Wei et al., 2020). Notch signaling drives SLF identity and is upregulated in the acute and chronic inflammatory response in CCs and SLFs (**Figure 30**). To show the morphological character of the subsetted SF, a sublining- and lining-layer signature enrichment analysis was performed and displayed the bipolar character of the SFs (**Figure 32A**) (Wei et al., 2020). While the sublining signature was enriched in the aSLFs and hSLFs, the lining layer signature was uniquely enriched in the LLFs. This result indicates a clear positional identity of the SFs, which can be observed in chronic and remission subsets.

Figure 31. Synovial fibroblast in chronification and remission of the arthritic inflammation

UMAP representation of synovial fibroblast healthy sublining layer fibroblasts (hSLF), activated sublining layer fibroblast (aSLF), lining layer fibroblasts (LLF)). resolved according to T-reg depletion.

Additionally, the Dll-activated fibroblast signature was used (Wei et al., 2020) to observe the Notch activation pattern in remission and chronification of the ArInf. A clear enrichment of the Dll signature was observed in the aSLFs, primarily found in chronification at day 56 (**Figure 32A**). This result indicates that decreasing Notch signaling is essential in the remission of ArInf. Next, the expression of the canonical marker *Prg4* was used, which is known to gradually change its expression towards the synovial membrane lining the inner surface of the joint capsule (Wei et al., 2020). *Prg4* encodes proteoglycan 4 (alias: lubricin). Proteoglycan 4 is a major compound in synovial fluid and on the articular cartilage surface and therefore performs an essential role in joint lubrication and synovial homeostasis (Mizoguchi et al., 2018; Svensson et al., 2020). Two different gradients of *Prg4* expressions were observed, with the maximum *Prg4* expression in the center of the LLF cluster (**Figure 32A, B**). A significant difference was observed in the formation of this gradient towards the SLF compartments. The aSLFs, primarily found in the chronic synovium, exhibited a *Prg4* gradient reaching deep into the aSLF cluster, whereas the *Prg4* gradient towards the hSLFs sharply drops at the edge of the hSLF cluster. This finding indicates a fundamental difference in the expression pattern of the critical marker gene *Prg4* in the chronification and remission of arthritis. To further analyze the different gradients of *Prg4* expression, the co-expression of an abundant and significant marker for aSLFs (*Cxcl14*) and hSLFs (*Gsn*) with *Prg4* was observed (**Figure 32B**). In the chronification of the ArInf, a strong co-expression of Cxcl14 and *Prg4* was observed. This co-expression with *Prg4* was not observed for the hSLF marker gene Gsn. This result underlines the altered expression pattern of *Prg4* in the two pathological states of this model and suggests a restricted *Prg4* expression to the LLFs in the remission of the arthritis response and an upregulation of the *Prg4* expression in the SLF compartment in chronic arthritis. This observation is supported by the presence of *Prg4* in the acute and chronic inflammatory signature of SLF (**Figure 26 and Figure 28A**).

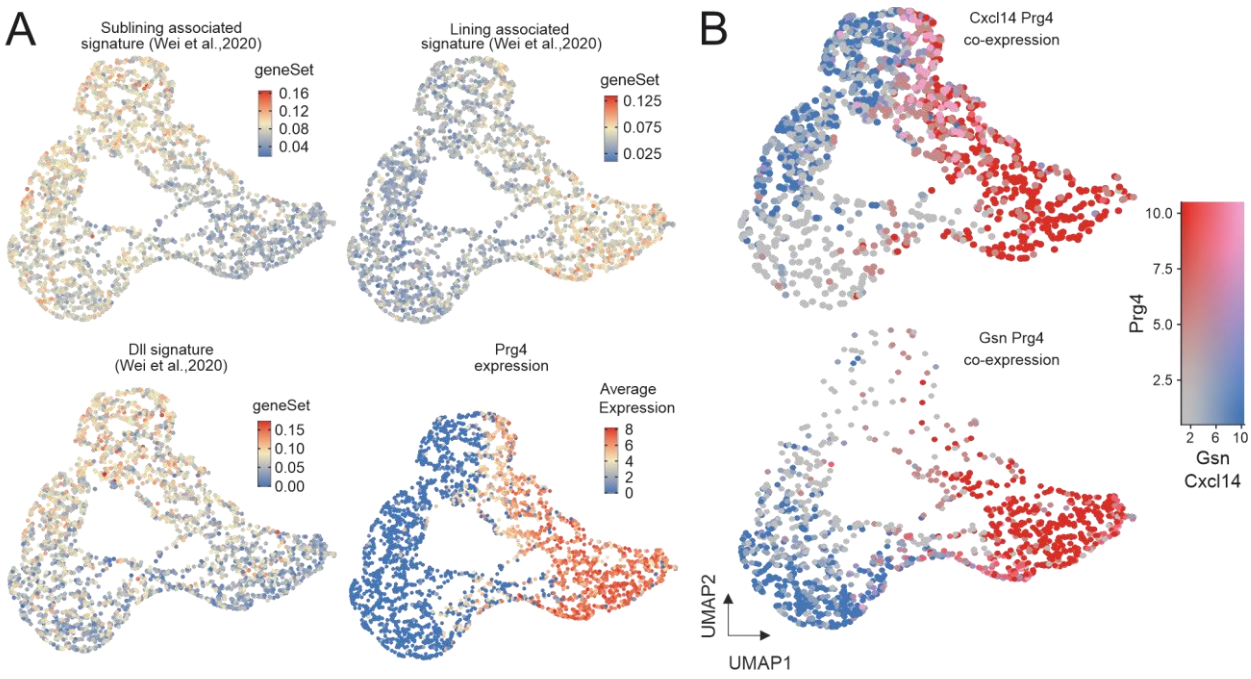

Figure 32. Polar character of synovial fibroblasts in chronification and remission of arthritic inflammation

A UMAP visualization showing AUCell-based enrichment scores (AUC scores) of sublining associated- and lining-associated signature published by Wei et al., overlaid on synovial fibroblast at day 56 (upper row). Dll signature published by Wei et al. overlaid on synovial fibroblast at day 56 and *Prg4* expression (lower row). **B** UMAP visualization showing the co-expression (violet) of Cxcl14 (marker for aSLF, upper plot, in blue) and Gsn (marker for hSLF, lower plot, blue) with *Prg4* (in red).

An increase in Notch signaling in the aSLFs was observed compared to the hSLFs. Wei et al. recently described this finding and showed that NOTCH3 signaling drives both transcriptional and spatial gradients originating from vascular endothelial cells. In addition, an increasing *Prg4* expression gradient was added to this model, which underlies inflammation and pathology in inflammatory arthritis.

4.2.8 *Prg4* expression pattern in the healthy, acute- and chronic inflammatory synovium

A subset of the mesenchymal cell cluster was created to investigate the Prg4 expression in the different states of the ArInfs (**Figure 33A**). This subset of SFs was normalized to a cell number of 1407 cells in each condition. This randomly selected cell subset allows us to compare the numbers of Prg4-expressing cells among ArInfs. Next, the expression levels of *Prg4* were plotted for all conditions and exhibited a restriction to the LLFs compartment and a small portion of the hSLFs in the control and the T-reg-depleted group at day 0 (**Figure 33B**). This exclusive expression is lost on day 14 in the control and the T-reg-depleted groups. Finally, in **Figure 33C**, only the cells expressing *Prg4* were extracted to show the changes in *Prg4* expression in cluster specificity and quantity.

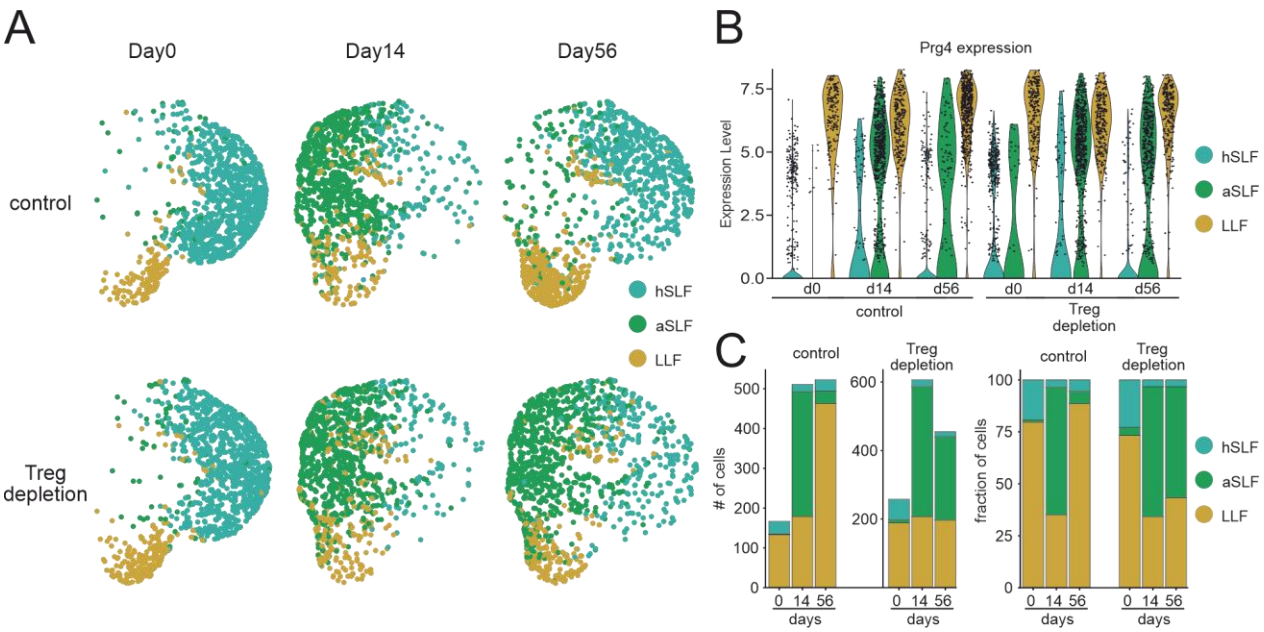

Figure 33. *Prg4* expression in synovial fibroblasts in health and arthritic inflammation

A UMAP representation of cell number normalized healthy sublining layer fibroblasts (hSLF), activated sublining layer fibroblast (aSLF), lining layer fibroblasts (LLF)). resolved according to sampling time point and T-reg-depleted condition. **B** Violin plots showing *Prg4* expression in hSLFs, aSLFs, and LLF resolved according to sampling time point and

T-reg-depleted condition. **C** Cell numbers and fractions of synovial fibroblasts expressing *Prg4*.

In the T-reg-depleted condition, a mild decrease of the *Prg4* expressing SLFs at day 56 compared to day 14 was observed, indicating a chronification of the ArInf. Interestingly, the remission of ArInf significantly increased the number of LLFs expressing Prg4. A Light-sheet microscopy study previously showed that lining macrophages, but not interstitial sublining macrophages, specifically express Cx3Cr1 and form dense membrane-like barriers between the synovial cavity and tissue (Culemann et al., 2019b). These results highlight the critical role of this membrane-like barrier, and its disruption may lead to joint inflammation. The expression pattern of *Prg4* is believed to be closely linked to the integrity of the synovial membrane's barrier.
Moreover, with an intact membrane-like barrier of LLFs and SLMs, *Prg4* expression is tightly restricted to the lining layer of the synovium. This condition is represented by the day 0 samples in the control and the T-reg-depleted group (**Figure 33B, C**). A loss of barrier function can cause signaling molecules to penetrate the synovial membrane and impact gene expression, such as *Prg4*. The barrier and misguided signaling disruption mentioned above are reflected in the altered Prg4 expression of SLFs during both acute and chronic inflammatory responses (**Figure 33B, C**). However, the specific signal responsible for the upregulation of *Prg4* in SLFs during the acute inflammatory response remains unknown.

4.2.9 *PRG4* expression is regulated via a TGFb-CREB5 axis

The loss of barrier function in the synovial lining layer results in an increase in *Prg4* expression in SLFs, likely due to signaling originating from the synovial cavity. This signaling is prevented by the protective barrier function of the synovial lining layer, which is disrupted in the context of RA. *Prg4* expression is controlled by the transcription factor CREB5 and requires signaling via TGF-β and EGFR (Zhang et al., 2021). In articular cartilage, *Prg4* expression is limited to the superficial layer and is not found in deeper

layers of the tissue (Marcelino et al., 1999; Schumacher et al., 1999; Rhee et al., 2005). This finding shows that cells lining the inner synovial space produce *Prg4* through a spatially controlled transcription program. As observed by Zhang et al., the co-localization of *Creb5* with *Prg4* expression in CC is also seen in cells expressing *Prg4* in the synovial membrane (**Figure 34A**), suggesting a similar mechanism. In addition, macrophages show the highest average expression of Tgfb1, providing a constant source of TGF-β1 for consistent *Prg4* expression in the synovial lining layer (**Figure 34B**). Previously described *Prg4* competence in articular cartilage via CREB5 is not exclusive to CCs in this specific niche. *Prg4* expression can also be observed in the LLFs of the synovium.

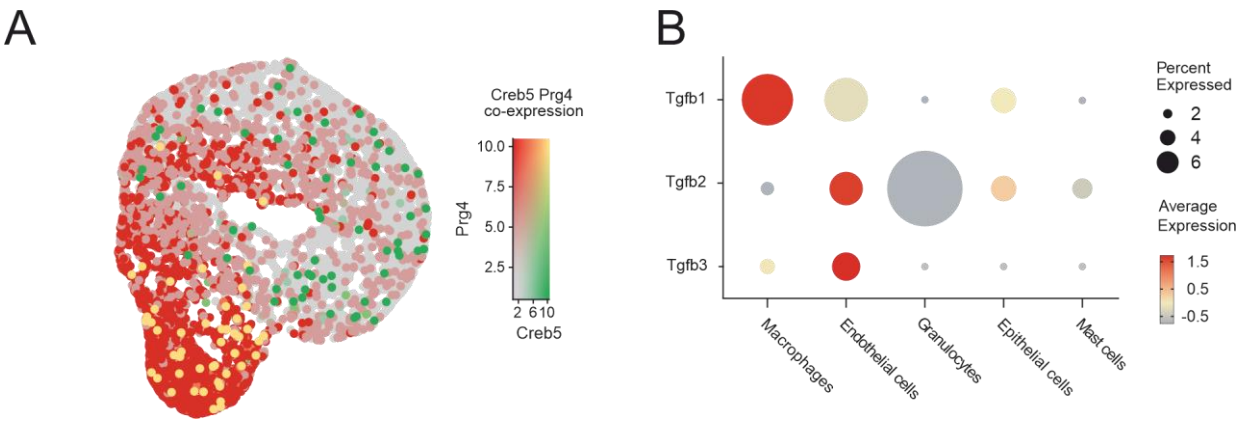

Figure 34. *Creb5* and *Prg4* expression in the synovial lining layer

A UMAP visualisation showing the co-expression of the *Creb5* transcription factor with *Prg4*. **B** Dot Plot showing expression of the murine Tgfb genes in macrophages, endothelial cells, granulocytes, Epithelial cells, and mast cells.

4.2.10 SLMs express *Tgfb1* and reduce in number during ArInf

To investigate the macrophage cluster in the different states of ArInf, myeloid cells were subsetted in **Figure 35A**. In this subset, SLM/interstitial macrophages (*Cx3cr1*$^{+}$, *Pf4*$^{+}$), infiltrating macrophages (*Arg1*$^{+}$, *Spp1*$^{+}$), and MHCII^{high} DCs were identified via marker gene expression (Culemann et al., 2019b). Two clusters also exhibited markers of myeloid

cells together with either Endothelial cell or SF markers (**Figure 35B**, marker genes of doublet cells not shown). SLMs create an inner immune barrier at the synovial lining and help maintain their numbers by exhibiting characteristics of epithelial cells, such as tight junctions and polarity. They also proliferate locally to maintain their numbers (Culemann et al., 2019b). The macrophage subset showed a decrease in the fraction of lining/interstitial macrophages and an increase in infiltrating macrophages during acute arthritis inflammation, with the trend continuing in chronification and reversing in remission **(Figure 35C, D**). Loss of SLMs is associated with a barrier instability of the synovium. Inflammation-associated barrier breakdown occurred together with the infiltration of monocyte-derived macrophages. The fraction of infiltrating expanded drastically in the acute inflammatory response and chronification of arthritis (**Figure 35C, D**).

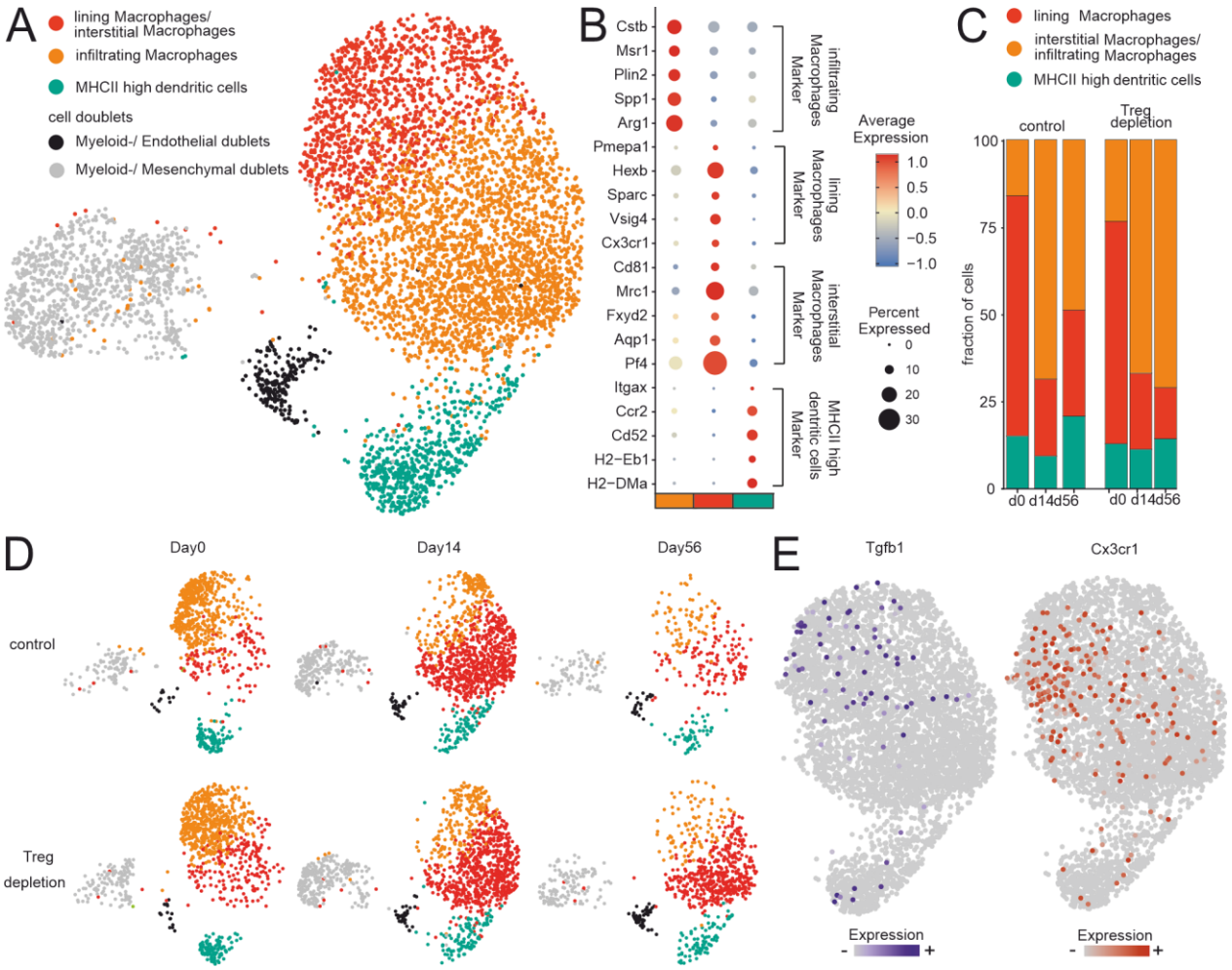

Figure 35. Macrophage sub-cluster in acute and chronic arthritic inflammation

A UMAP representation of macrophage subsets. **B** Dot Plots showing expression of specific marker genes (Cstb, Msr1, Plin2, Spp1, Arg1 = infiltrating macrophages; Pmepa1, Hexb, Sparc, Visg4, Cx3cr1 = lining macrophages; Cd81, Mrc1, Fxyd2, Aqp1, Pf4 = interstitial macrophages; Itgax, Ccr2, Cd52, Cd52, H2-Eb1, H2-DMa = MHCII high dendritic cells). **C** Fraction of myeloid cells resolved according to cellular clusters. **D** UMAP representation of macrophage scRNA-seq results resolved according to sampling time point and T-reg-depleted condition. **E** Feature plots depicting expression of Tgfb1 and Cx3cr1. The color scheme in **A** applies to the entire Figure 35.

Tgfb1 expression was primarily abundant in the SLM/interstitial macrophage cluster (**Figure 35E**). Due to the niche-related physical proximity of SLMs to the LLFs and the

crucial TGFB1 stimulation for their *Prg4* expression, it can be assumed that the SLMs are the primary source of TGFB1 in the synovial niche.

Our data show changes in the macrophage subset during different stages of arthritis inflammation, with a decrease in lining/interstitial macrophages and an increase in infiltrating macrophages. In addition, the presence of TGFB1 in the SLM/interstitial macrophage cluster highlights the critical role of synovial macrophages as a source of TGFB1 in the synovial niche.

5 Discussion

5.1 Generation and analysis of RtL-embryoids

In this thesis, a new method to generate embryo-like structures was presented, termed RtL-embryoids, based exclusively on ESCs. This technique combines reprogramming paradigms through TFs with 3D co-cultures. It was demonstrated that the induction of five TFs associated with TSC-fate in one ESC line and one TF associated with XEN cell fate in a second ESC line, when cultured with a third, unaltered ESC line, results in the generation of structures resembling natural murine embryonic structures at E4.5-E5.5. Additionally, the need for multiple individual stem cell cultures and complex cell culture reagents was abolished. Previous studies demonstrated that structures that resemble embryos could be generated by the spontaneous self-assembly of ESCs, TSCs, and XEN cells derived from blastocysts (Sozen et al., 2018; Zhang et al., 2019b; Rivron et al., 2018). Each cell line needs complex cell culture reagents and handling processes, which must be performed in parallel. The TF-mediated reprogramming of ESCs towards iTSCs and iXENs combined with co-culture conditions of these ESC-derived cell types have demonstrated that exclusively ESCs can be used as a starting population to generate embryo-like structures. Furthermore, it was previously shown that TF-mediated reprogramming allows for the generation of iTSC and iXEN cells from murine ESC (Rivron et al., 2018; Niwa et al., 2005; Niakan et al., 2013; Wamaitha et al., 2015), which is the primary step allowing the generation of RtL-embryoids.

Our findings demonstrate that reprogramming iTSC- or iXEN-like cells into a 3D co-culture environment results in the induction of the respective cell lineage and compartmentalized embryo-like structures. Thus, it was hypothesized that the reprogramming of cells in a 3D environment would lead to crosstalk between cells undergoing cell-fate conversion, ultimately providing a method to produce multicellular, complex embryonic, and extraembryonic tissues.

5.1.1 Interaction potential of VE-like and Epi-like compartments

It has been described that XEN cells undergo VE differentiation in response to BMP signaling (Paca et al., 2012). A subpopulation of cells within the ExE-like cells of the RtL-embryoids expressed Bmp4 and Bmp8b, like the expression patterns observed in murine embryogenesis. We, therefore, hypothesized that overexpression of Gata6 in murine ESC, along with BMP4 signaling from the compartments expressing Gata6, induces a cellular reprogramming towards an iXEN identity, which forces the converting cells to have an induced VE-like fate. Additionally, to the VE-like fate, highly specialized VE-lineages were formed, such as the DVE/AVE, all of which indicate VE-like subpopulations. Although the DVE/AVE-like population of cells did not exhibit much migration capability, some aggregates showed positioning in a truly anterior location relative to the Epi-like compartment. Accordingly, an anterior-Epi gene signature enrichment was observed within epi-like cells but no enrichment in the transition or posterior Epi gene signatures. Assessment of pluripotency states within Epi-like cells indicates a progression from naïve- to primed-pluripotency, comparable to published roadmaps of pluripotency development during rosette to lumen maturation (Neagu et al., 2020). Based on the lack of downregulation of Nanog and the absence of expression of T, Cer1, and Foxa2, it was concluded that the Epi-like compartment of RtL-embryoid cells could not reach a state of full primed pluripotency.

5.1.2 Signaling in RtL-Embryoids resembles embryo tissue interactions

Some of the Epi-like cluster cells showed signs of PGC formation. In mice, PGCs are specialized through BMP2/4 signaling, which leads to their differentiation into specialized cells. However, the transcriptional signatures of PGC obtained from murine embryos did not show any population overlaps with cells of the EPI-like cluster in the integrated reference dataset (**Figure 10A, B**). Therefore, the upregulation of PGC marker genes observed here is expected to follow a different pathway of transcriptional induction. In response to exposure to BMP and WNT, it has previously been demonstrated that PGC-

like cells could be derived from Epi-like cells (Hayashi et al., 2011). It is, therefore, most likely that the PGC specification observed here is a consequence of signaling cascades facilitated by BMP4 and BMP8b secretion from the ExE-like compartment adjacent to the Epi-like compartment rather than the natural route of PGC specification (Lawson et al., 1999; Ying et al., 2000; Ewen-Campen et al., 2010; Ying et al., 2000; Hayashi et al., 2011). Another example of instructive interaction between Epi-like and ExE-like compartments is an ExE-like stem cell niche, which was stimulated to proliferate and develop through an FGF4-producing Epi-like compartment. FGF4 signaling from the Epi is essential for the proliferation of the TSC compartment within the ExE (Tanaka et al., 1998; Niswander and Martin, 1992; Feldman et al., 1995; Wen et al., 2017).

Furthermore, RtL-embryoids display a closely related signaling pathway to natural murine embryos, as *Fgf4* is expressed in the Epi-like compartment. It appears that a subpopulation of cells within the ExE cluster expressed the necessary receptor *Fgfr2* for FGF4 signaling and its downstream targets simultaneously. In support of this observation, a pERK activation pattern was shown within the ExE-like compartment, similar to the ExE of natural embryos between the E5.5 and E6.5 (Corson et al., 2003).

5.1.3 Possible applications and advantages of RtL-embryoids

According to these findings, the crosstalk between the compartments of RtL-embryoids results in a more complex conversion of cell fate and TF-mediated reprogramming into iTSC and iXEN cell fates. A potential benefit of the system presented here is its potential use as a tool for enriching and isolating rare stem cell types such as DVE, AVE, and PGC-like cells. Furthermore, in the simplified approach outlined above, using an ESC-based population of cells as a starting population diminishes the need for costly, individual cell culture reagents, which are usually required for maintaining and propagating each stem cell line (ESC, TSC, and XEN). Moreover, using the 3D mold techniques, it is possible to produce >700 correctly assembled RtL-embryos in a single 12-well plate.

The RtL-embryoids develop an early embryo architecture of inner- embryonic and extraembryonic compartments, displaying rosette formation and progression to the lumen

in Epi-like and ExE compartments. In particular, they can model the development and interactions of the EPI, the VE, and the ExE of murine embryos at E4.5 and E5.5. Embryonic processes in this developmental time range can be investigated in more detail using RtL-embryoids without sacrificing murine embryos or the need for animal facilities.

5.1.4 Classification of RtL-embryoids into the cell-based embryo models

Recently, a scheme was introduced to distinguish between cell-based embryo models that simulate the underlying morphology and models that mimic selective morphogenetic events (Rossant and Tam, 2021). Consequently, models such as gastruloids that can emulate selective events should be considered non-integrated stem-cell-based embryo models. Therefore, it is reasonable to consider that models in this study, such as blastoids, ETX-, and RtL-embryoids, are integrated stem-cell-based embryo models since they model multiple interacting tissues of the conceptus (Rossant and Tam, 2021). As stem-cell-based embryo models gain popularity, several terms, such as artificial and synthetic, are currently used to describe the structures generated. For such synthetic embryo models to be considered synthetic, new genetic switches or synthetic pathways would need to be preprogrammed into the originating cell population before the model can be considered (Rossant and Tam, 2021). The RtL-embryoids described are based on the use of cells with conditional genetic switches that can be activated depending on the experimental requirements. The RtL-embryoid system is therefore considered a synthetic embryo model. Collectively, RtL-embryoids serve as a synthetic and integrated stem cell-based model for investigating the spatiotemporal control of gene expression and cellular communication during the early phases of murine embryonic development.

5.2 Analysis of the G6PI-induced arthritis Seq-Well dataset

RA is a severe systemic autoimmune disease predominantly described by an inflammation of the joints (Smolen et al., 2018; McInnes and Schett, 2011), creating a substantial burden on individuals and society with an increasing prevalence (Annika Steffen et al., 2017). A current treatment strategy uses small molecule inhibitors to target immune cells, secretory products, or specific signaling pathways (Schett et al., 2008; Yap et al., 2018; Guo et al., 2018). Unfortunately, despite advances in treatment, many patients do not respond to current therapies, regardless of the drug's mechanism of action (Di Liu et al., 2017). Therefore, understanding the cellular mechanisms that allow joint inflammation to persist within the synovial microenvironment is crucial for identifying therapeutic targets and translating them into successful clinical trials. In the present study, the G6PI-induced arthritis model was utilized to investigate the synovial tissue-resident cells such as SFs and macrophages. These cell types form the basis of the joint microenvironment, ensuring tissue homeostasis and regulating local inflammatory responses (Buckley, 2011; Buckley and McGettrick, 2018; Filer et al., 2017; Mosser et al., 2021; Parsonage et al., 2005). To better characterize G6PI-induced arthritis, the portable Seq-Well scRNA-seq system was used to identify the major cell types and cellular states in the synovium. The analysis of the dataset was focused on mesenchymal cells, and it identified three types of cells: SLFs, LLFs, and CCs. In addition, defined cellular states were revealed in homeostasis, acute and chronic inflammation. The inflammatory activation of SLFs and LLFs was associated with endothelial-derived Notch signalling, which induces pathogenic activation in the aSLFs and CC compartments. I propose a model connecting dysregulated *Prg4* expression in the aSLFs, resulting from CREB5-mediated TGF-β signaling (Zhang et al., 2021), to a breakdown of the synovial barrier of the most likely involving *Cx3cr1*$^{+}$ SMs. The expression of *Prg4* in the synovium is maintained under homeostasis exclusively by the LLFs.

5.2.1 Inflammatory kinetics of mesenchymal cells in the G6PI-induced arthritis

Mesenchymal cells are essential for the formation and functioning of the microenvironment in tissues (Parsonage et al., 2005; Buckley, 2011). This study sheds light on the role of SFs, which take part in inflammation and tissue damage and drive multiple aspects of the pathology in Arthritis. The scRNA-seq data revealed various pathological aspects of SFs, involving the expression of chemokines, cytokines, and proteases that affect the recruitment, retention, and differentiation of infiltrating monocytes and neutrophils. These aspects of arthritis have been reported in several studies before (Bartok and Firestein, 2010; Konttinen et al., 1999; Turner and Filer, 2015; Friščić et al., 2021; Liu et al., 2020). Historically, the synovial fibroblast heterogeneity in RA has been studied primarily in positionality, protein expression, and defining the lining and sublining layers of the synovium as distinct anatomical regions (Ramirez-Montagut et al., 2004; Middleton et al., 2005; Fassbender, 1983). However, recent scRNAseq studies have defined cellular diversity at the transcriptional level (Croft et al., 2019; Mizoguchi et al., 2018; Stephenson et al., 2018; Zhang et al., 2019a). Furthermore, support the identification of two transcriptionally distinct fibroblast clusters known as SLFs and LLFs through scRNA-seq signatures from Friščić et al., 2021. The present work could contribute the first inflammatory signatures for these subclasses of SFs in the context of ArInf. This observation was in line with an expansion of pathological fibroblast subsets in the sublining synovial tissue, which was also demonstrated by others (Croft et al., 2019; Mizoguchi et al., 2018; Zhang et al., 2019a). One limitation of our dataset is that the usual marker for SLFs, *Thy1*, which typically displays a transcriptional gradient with high expression at outer vascular locations and low expression near the synovial lining (Wei et al., 2020), was found in only a limited number of cells in our scRNA-seq data. Further, a CC cluster was described with a clear activation pattern in acute and chronic inflammation and a drastic reduction in cell fractions compared to healthy conditions. The study also compared gene expression profiles between aSLFs, LLFs, and CCs in acute and chronic inflammation. The results revealed a concordance in gene expression between acute and chronic inflammation, but with reduced expression of inflammatory mediators in ArInf during chronic inflammation.

5.2.2 ArInf remodels the healthy synovial microanatomy

The phenotypic characteristics of SFs are closely linked to the joint microenvironment, as they are susceptible to molecular changes in this environment (Wei et al., 2020). For example, it was recently shown that the canonical markers THY1 and PRG4, which are indicative of SLFs and LLFs respectively, are expressed in a transcriptional gradient in synovial tissue. *Thy1* expression is highest in the sublining layer, while *Prg4* is predominantly expressed in the inner lining layer. This inverse expression gradient is crucial for shaping the microenvironment and determining the function of synovial fluid cells based on their localization within the synovium. Furthermore, the sublining identity is regulated by constant endothelium-derived Notch signaling (Wei et al., 2020).

Additionally, the present work documented elevated levels of Notch activation signature in CCs, which was even stronger than in aSLFs. This observation is of significance because Notch signaling has been shown to play a complex role in cartilage homeostasis. The expression of Notch signaling components, including NOTCH1, JAG1, and HES5, is abundant in OA biopsies and has been shown to be highly activated in both human and mouse joint tissues in post-traumatic OA (Karlsson et al., 2008). Therefore, elevated levels of Notch activation signature in CC and aSLFs observed in the present study highlight the need for a better understanding of Notch signaling in cartilage homeostasis and joint integrity.

However, the underlying stimuli of *Prg4* expression in the lining layer remain unknown. Our study demonstrates a shift in the *Prg4* expression gradient towards the sublining pole in ArInf compared to the healthy condition, suggesting alterations in synovial microenvironment signaling. Further experimentation and research are necessary to clarify the precise mechanisms behind these changes.

SFs exhibit significant plasticity in response to local signals within the synovial microenvironment, resulting in transcriptionally distinct phenotypes based on their location within the synovium. These positional cues orchestrate the formation of synovial tissue niches favorable for the invasion of inflammatory cells and the production of inflammatory

mediators. Therefore, it will be necessary to identify and target critical regulatory pathways that sustain pathogenic fibroblast states in the ArInf.

5.2.3 TGF-β signaling drives *Prg4* expression in SLFs and destabilises synovial tissue integrity

The dysregulated *Prg4* expression in acute and chronic arthritis and its restricted expression to the LLFs in homeostasis and remission of the ArInf let us assume that there must be a driver of *Prg4* expression and LLF identity. The most likely cellular candidate providing such molecular signaling in the synovial microanatomy is a layer of CX3CR1^{+} tissue-resident macrophages because they form an epithelial-like cell layer lining the synovium and shield the lining- and the sublining layer from the synovial cavity (Culemann et al., 2019b).

The activation process of *Prg4* expression in SFs was investigated to support this hypothesis. Our analysis, which utilized a cell number-normalized subset of the fibroblast cluster, revealed the *Prg4* expression pattern during homeostasis, acute and chronic inflammation, and the remission phase of arthritis. In homeostasis and remission, *Prg4* expression was found to be highly specific to LLFs. However, during both acute and chronic inflammation, a majority of *Prg4*-expressing cells were identified as SLFs.

It was recently demonstrated that CREB5 establishes the competence for *Prg4* expression in CCs in response to TGF-β and EGF signaling (Zhang et al., 2021). Thus, this signaling and transcriptional activation mechanism may also be conserved in fibroblasts within the synovium. Both LLFs and SLFs express Creb5. However, the co-expression of Creb5 and Prg4 was primarily observed in LLFs. This result can be explained by the dependency of Prg4 expression on other TFs in addition to CREB5, which may not be present in SLFs. Zhang et al. recently published fluorescent images of murine joints in which *Creb5* and *Prg4* are co-expressed in the articular cartilage; upon closer inspection, this co-expression can also be observed at the synovial lining layer, which is in line with our observations. It was also possible to identify the SMs as the primary source of *Tgfb1* in the synovium, supporting the hypothesis that the SM shapes the identity of LLFs. Others also showed *Tgfb* expression of synovial macrophages (Munter et al., 2017). A paracrine stimulation of the LLFs by the SMs may involve not only

Tgfb1 but also a variety of growth factors secreted by the SMs (van Lent et al., 2004; Takano et al., 2016). LLFs and SLMs enclose the joint cavity at resting conditions, creating a tight immunological barrier (Culemann et al., 2019a). As a result of serum transfer-induced arthritis, Culemann et al. demonstrated immune complex-mediated synovial lining barrier breakdown (Culemann et al., 2019a). G6PI-induced arthritis also shows the breakdown of this barrier, as demonstrated by the loss of macrophages from the synovial lining layer in acute and chronic arthritis.

This change in microanatomy of the synovium goes along with dysregulation of *Prg4* expression, leading to a strong upregulation in the sublining layer. Therefore, this dysregulation of a functional protein restricted to the synovial cavity could be one possible aspect of pannus formation in chronic arthritis. However, it is debatable if the Tgfb expression of the SLMs is the primary source for the downstream *Prg4* expression in the sublining layer. Especially because the *Cx3cr1*$^{+}$ macrophages exhibited a reduction in cell number in acute and chronic inflammation, infiltrating neutrophils could be an additional source of TGFB or EGF, which are known to invade the joints in ArInf. Another possible source could be the synovial fluid which functions as a reservoir for growth factors (Schlaak et al., 1996; Fava et al., 1989; Garbers et al., 2015), which diffuse into the synovium after losing the synovial barrier function. The results of an exciting study, in which the synovial lining layer was depleted, and TGF-β1 was overexpressed in murine knee joints, demonstrated that TGF-β1 caused dramatic histopathological changes that were not observed in knee joints with a functional synovial lining layer (Bakker et al., 2001). While these results show the importance of synovial barrier integrity in connection with TGF-β1 signalling, they were not linked to changes in gene expression.

The acute and chronic inflammation of the joints goes along with a loss of healthy tissue structure of the synovium. Therefore, SLMs are a potential upstream signal provider for changes in *Prg4* gene expression in LLFs. Under homeostatic conditions, this regulation is restricted to the synovial lining layer but dysregulated in acute and chronic arthritis, which leads to *Prg4* expression in the sublining layer of the synovium.

5.2.4 Increased bidirectional TGF-β and Notch signaling in arthritis-induced synovial barrier dysfunction

The synovial microenvironment of the healthy joint follows a clear tissue organization with an inner lining layer covering the synovial cavity and an outer sublining layer. This microanatomic structure is found only in healthy joints and is lost in ArInf (**Figure 36**). The synovial joint microenvironment may play a significant and continuous role in preventing spontaneous inflammation responses and subsequent inflammation-associated tissue damage in a steady state. One significant cell type for maintaining synovial homeostasis are SMs. However, the precise role and the development of these cells were elusive until recently. Studies showed that synovial macrophages of healthy individuals display an elevated expression of the scavenger receptor CD163 and an increased phagocytic capacity within the layer of SLMs (Tak and Bresnihan, 2000; Kurowska-Stolarska and Alivernini, 2017). Considering these observations, these cells contribute to removing bone debris and cartilage from the synovial fluid and may assist in joint function.

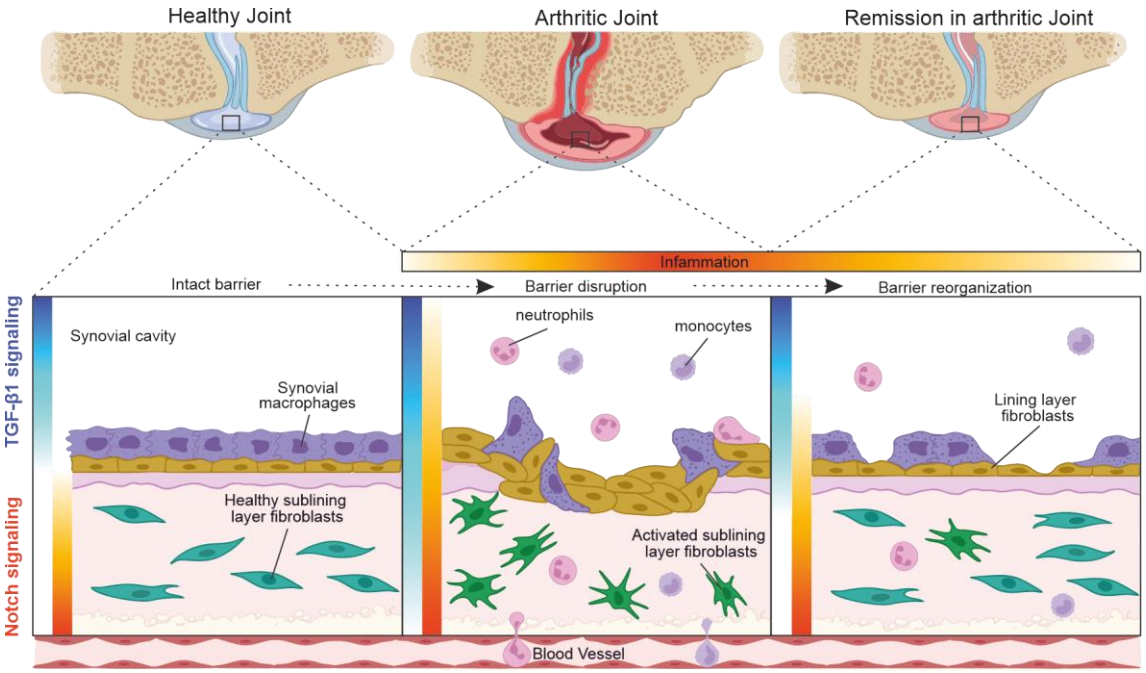

Figure 36. Schematic summary

Lining macrophages and lining layer fibroblasts form a protective barrier that degenerates during arthritic inflammation, enabling the infiltration of inflammatory myeloid cells into the synovial cavity. This synovial barrier is reorganized during the resolved inflammatory response. This barrier integrity is inverse proportional to endothelial-derived Notch- and lining layer macrophage-derived TGF-β1 signaling.

The use of new approaches, including scRNA-seq and fate mapping, has recently provided valuable insights into the functional heterogeneity and origin of synovial monocytes and macrophages during inflammation and RA (Culemann et al., 2019b; Zhang et al., 2019a). ScRNA-seq, fate mapping and three-dimensional light-sheet microscopy provided critical insights into synovial macrophage subsets spatiotemporal composition, origin, and biology. Macrophages within the synovial lining, but not within the interstitial sublining, selectively expressed the chemokine receptor CX3CR1. These tight-junction-mediated barriers isolate the synovial capillary network from the synovial cavity (Culemann et al., 2019b). This endothelial-like layer of cells controls joint inflammation since autoantibody-containing immune complexes activate this macrophage subset and result in the disintegration of tight junctions, resulting in arthritis and the infiltration of myeloid cells inside inner joints. Therapeutic stabilization of tight junctions prevents the onset of arthritis and depleting *Cx3cr1*-expressing macrophage subset resulted in impairment of barrier function, spontaneous arthritis formation, and an accelerated onset of K/BxN serum transfer arthritis (Culemann et al., 2019b). These observations are in line with the G6PI-induced arthritis model in which the loss of *Cx3cr1*-expressing macrophages is also observed in acute and chronic ArInf.

A further scRNA-seq study described endothelium-derived Notch signalling that drives SLFs identity and arthritis pathology (Wei et al., 2020). ScRNA-seq signatures exhibited increased Notch signalling in the acute and chronic ArInf and a weakening Notch signalling during remission, resembling homeostatic Notch signalling.

Taking these observations and our findings over time into account, a model evolves that would suggest a link between increased Notch signaling and loss of barrier integrity. In CCs, a similar increase in Notch signaling was observed in acute and chronic arthritis, which has not been described in the literature.

Besides the Notch signaling derived from the endothelium, counteractive signaling has been proposed to impact fibroblast identity and LLF protein expression. The LLF marker,

Prg4 (Rhee et al., 2005), exhibits a disease-specific expression pattern and appears to counteract Notch signaling in G6PI-induced arthritis. In the healthy Synovium, *Prg4* expression is limited to the LLFs, but it increases in the inflamed sublining layer of the synovium (**Figure 36**). Recent studies also reveal the expression of the transcription factor Creb5 in various synovial tissues, including the articular perichondrium and synovial fluid, establishing its role in regulating Prg4 expression in articular cartilage (Zhang et al., 2021). Furthermore, it was demonstrated that CREB5 binds to two *Prg4* promoters upon TGF-β stimulation. The *Prg4* locus displays an open chromatin conformation in superficial zone articular CCs and acts together with a more distal regulatory element to cause *Prg4* induction. This mechanism of Prg4 regulation could be conserved in both articular cartilage and synovial joint tissue, as these tissues are derived from progenitor cells expressing Gdf5 in the murine embryo (Koyama et al., 2008; Rountree et al., 2004; Shwartz et al., 2016). In healthy synovium, SLMs are most likely the exclusive signaling provider due to their positional niche inside the synovium. Therefore, *Tgfb* expression in SLMs was shown and described as a potential activator of *Prg4* expression in the LLFs. Since SLMs are in direct contact with LLFs, these macrophages may act as the most prominent source of TGF-β1.

In acute ArInf, the barrier of LLFs and SLMs is disrupted, and the niche necessary for healthy synovial homeostasis is lost (Culemann et al., 2019b; Culemann et al., 2019a). In our scRNA-seq dataset *Cx3cr1*-expressing, synovial lining macrophage numbers decrease drastically during acute and chronic arthritis with a substantial increase of cells expressing *Prg4* in the synovium, which raises the question of which cell types could provide the signalling for *Prg4* expression in acute and chronic arthritis. *Tgfb1* is highly expressed in HLA-DRA^{+} cells and cartilage cells in human osteoarthritic knees (Chou et al., 2020), indicating a potential role as a source of cytokines and growth factors in the synovial fluid. CCs can produce high concentrations (10-40 ng/mL) of TGF-β in the synovial fluid (Albro et al., 2013). However, CC numbers also decrease significantly during acute and chronic arthritis. A further source of TGF-β in the synovial tissue, especially during inflammation, could be infiltrating immune cells like monocytes and neutrophils, which were observed in acute and chronic arthritis. In addition, monocytes and neutrophils

secrete TGF-β as a component of wound healing and the pathogenesis of fibrotic diseases (Grotendorst et al., 1989).

Combining our findings and previous reports, we suggest the following model for the role of TGF-β. In healthy synovial tissue, TGF-β expression is tightly controlled (**Figure 36**), secreted into the synovial fluid, and stimulates the superficial zone articular CCs and SLMs. This myeloid cell layer acts as a physical barrier and prevents uncontrolled TGF-β signaling toward underlying cell layers. When this barrier is disrupted, TGF-β signaling can diffuse into the synovial sublining layer and induces disease-specific gene expression in SLFs. This activation includes our dataset ECM protein deposition, fibroblast proliferation, expression of protease inhibitors such as Timp1, and myofibroblast differentiation (not shown). These activation responses are signs of a fibrotic phenotype associated with TGF-β signals (Biernacka et al., 2011). In a study by Bakker et al., overexpression of TGF-β1 in the knee joint of mice results in a fibrotic response upon depletion of the synovial lining. However, a strong fibrotic response was not observed without the depletion of the synovial lining, suggesting the importance of the synovial lining to control TGF-β1 signalling (Bakker et al., 2001).

Our model shows a coordinated relationship between the Notch signaling originating from the endothelium and the TGF-β1 signaling derived from synovial lining macrophages, which is strictly maintained between the sublining and lining layers in healthy conditions. In cases of ArInf, the disruption of the lining layer barrier may result in a loss of this separation and increased penetration into the synovial sublining. Notch target genes are noticeably elevated in ArInf, and the signaling exhibits a similar spatial gradient, starting from the vascular endothelial cells and extending outwards (Wei et al., 2020). In healthy synovium, these two signaling pathways are mainly separated and show only limited overlap in signaling. However, the disruption of the synovial barrier and the upregulation of Notch signaling due to angiogenic processes may result in most SFs receiving both signals. There is evidence of interaction between the two signaling pathways, which can contribute to the transcriptional regulation of Notch target genes and inhibit myogenic differentiation and endothelial cell migration (Blokzijl et al., 2003; Dahlqvist et al., 2003; Itoh et al., 2004). However, they do not have a dependent relationship in the signaling cascade. Both signaling pathways can contribute to the transcriptional regulation of Notch

target genes and inhibit myogenic differentiation and endothelial cell migration (Blokzijl et al., 2003; Dahlqvist et al., 2003; Itoh et al., 2004). In addition, TGF-β induces several Notch receptor ligands, such as Jagged1 (Aidinis et al., 2005). The exact mechanism of this interaction inside the synovial tissue has to be studied further.

5.2.5 Future perspectives

Due to the spatial and temporal heterogeneity of synovial macrophages and SFs during inflammatory arthritis, synovial tissue niches are defined by specialized cell subsets that support the pathogenic behavior of this specialized tissue. Arthritis research should therefore focus on this specialization of synovial layers and their disruption during the ArInf. Ideally, these data should be extended by human kinetic scRNA-seq data spanning the healthy joints until chronification. Another essential aspect of barrier integrity of the synovial membrane is whether the arthritic response is causing the disruption or if the disruption is an integral part of the onset of the ArInf.

Future research efforts to understand the function of synovial cells during various phases of the disease should consider combining cellular heterogeneity scRNA-seq with *in vivo* and *in vitro* functional assays. Creating an arthritic cell atlas of human joints, including spatial transcriptomics to study local cellular interactions at the site of ArInf, is also a desirable goal. Utilizing epigenetic profiling technologies such as ChIP-seq can also help in understanding the epigenetic profile of SFs and the differences in gene regulation that may contribute to their phenotypic heterogeneity and modulation during chronic inflammation. These efforts could potentially lead to identifying new treatments for RA that target fibroblasts and improve current therapeutic approaches.

6 Conclusion

In this thesis, SCO were applied to a semi-artificial cell system, the RtL-embryoids, and sparse cell types in the joint under pathophysiological conditions with the G6PI T-reg depletion model.

ScRNA-seq (Smart-Seq2) reveals transcriptional profiles resembling EPI, PE, VE, and EXE of early murine embryos around E4.5–E5.5. The obtained dataset was characterised and compared with natural counterparts by mapping the single cells onto a reference dataset of murine embryos. This reference mapping made it possible to trace individual cells of the RtL-embryoid in the context of murine embryogenesis. Further, progression from naïve- to primed pluripotency was observed within Epi-like cells, together with lineage specification of PGCs. Furthermore, the anterior formation was observed as an interplay between the VE-like and Epi-like compartments. Finally, highly dynamic processes like embryonic tissue interaction were deciphered with data-driven NichNet analysis.

Further, scRNA-seq was used to map the single cells of the synovial joint under pathophysiological conditions. With this method, it was also possible to describe highly dynamic biological processes in the acute and chronic ArInf. By spanning the synovium's homeostatic, acute, and chronically inflamed conditions, it was possible to generate a dataset that allowed it to identify the inflammatory kinetics of the mesenchymal cells, which exhibited an overlap of the acute and chronic gene signatures. Additionally, the described positional identity of SFs shaped by endothelium-derived Notch signalling described by Wei et al. was confirmed in this thesis and extended by the dysregulated *Prg4* expression in the synovium. The *Prg4* expression dynamic in the ArInf was linked to the breakdown of the myeloid-synovial lining layer and increased TGF-β signaling.

In light of these results, SCO is suited to describe a semi-artificial cell system, the RtL-embryoids, and sparse cell types in the joint under pathophysiological conditions.

7 References

Aibar, Sara; González-Blas, Carmen Bravo; Moerman, Thomas; Huynh-Thu, Vân Anh; Imrichova, Hana; Hulselmans, Gert et al. (2017): SCENIC: single-cell regulatory network inference and clustering. In: *Nature methods* 14 (11), S. 1083–1086. DOI: 10.1038/nmeth.4463.

Aidinis, Vassilis; Carninci, Piero; Armaka, Maria; Witke, Walter; Harokopos, Vaggelis; Pavelka, Norman et al. (2005): Cytoskeletal rearrangements in synovial fibroblasts as a novel pathophysiological determinant of modeled rheumatoid arthritis. In: *PLoS genetics* 1 (4), e48. DOI: 10.1371/journal.pgen.0010048.

Akula, Srinivas; Paivandy, Aida; Fu, Zhirong; Thorpe, Michael; Pejler, Gunnar; Hellman, Lars (2020): How Relevant Are Bone Marrow-Derived Mast Cells (BMMCs) as Models for Tissue Mast Cells? A Comparative Transcriptome Analysis of BMMCs and Peritoneal Mast Cells. In: *Cells* 9 (9). DOI: 10.3390/cells9092118.

Albro, Michael B.; Nims, Robert J.; Cigan, Alexander D.; Yeroushalmi, Kevin J.; Alliston, Tamara; Hung, Clark T.; Ateshian, Gerard A. (2013): Accumulation of exogenous activated TGF-β in the superficial zone of articular cartilage. In: *Biophysical journal* 104 (8), S. 1794–1804. DOI: 10.1016/j.bpj.2013.02.052.

Alivernini, Stefano; Tolusso, Barbara; Petricca, Luca; Bui, Laura; Di Sante, Gabriele; Peluso, Giusy et al. (2017): Synovial features of patients with rheumatoid arthritis and psoriatic arthritis in clinical and ultrasound remission differ under anti-TNF therapy: a clue to interpret different chances of relapse after clinical remission? In: *Annals of the rheumatic diseases* 76 (7), S. 1228–1236. DOI: 10.1136/annrheumdis-2016-210424.

Amadei, Gianluca; Lau, Kasey Y. C.; Jonghe, Joachim de; Gantner, Carlos W.; Sozen, Berna; Chan, Christopher et al. (2021): Inducible Stem-Cell-Derived Embryos Capture Mouse Morphogenetic Events In Vitro. In: *Developmental cell* 56 (3), 366-382.e9. DOI: 10.1016/j.devcel.2020.12.004.

Annika Steffen; Jakob Holstiege; Benjamin Goffrier; Jörg Bätzing (2017): Epidemiologie der rheumatoiden Arthritis in Deutschland – eine Analyse anhand bundesweiter vertragsärztlicher Abrechnungsdaten.

Asquith, Darren L.; Miller, Ashley M.; McInnes, Iain B.; Liew, Foo Y. (2009): Animal models of rheumatoid arthritis. In: *European journal of immunology* 39 (8), S. 2040–2044. DOI: 10.1002/eji.200939578.

Bakker, A. C.; van de Loo, F. A.; van Beuningen, H. M.; Sime, P.; van Lent, P. L.; van der Kraan, P. M. et al. (2001): Overexpression of active TGF-beta-1 in the murine knee joint: evidence for synovial-layer-dependent chondro-osteophyte formation. In: *Osteoarthritis and cartilage* 9 (2), S. 128–136. DOI: 10.1053/joca.2000.0368.

Bartok, Beatrix; Firestein, Gary S. (2010): Fibroblast-like synoviocytes: key effector cells in rheumatoid arthritis. In: *Immunological reviews* 233 (1), S. 233–255. DOI: 10.1111/j.0105-2896.2009.00859.x.

Baßler, Kevin; Fujii, Wataru; Kapellos, Theodore S.; Dudkin, Erika; Reusch, Nico; Horne, Ari et al. (2022): Alveolar macrophages in early stage COPD show functional deviations with properties of impaired immune activation. In: *Frontiers in immunology* 13, S. 917232. DOI: 10.3389/fimmu.2022.917232.

Bazzi, Hisham; Fantauzzo, Katherine A.; Richardson, Gavin D.; Jahoda, Colin A. B.; Christiano, Angela M. (2007): Transcriptional profiling of developing mouse epidermis reveals novel patterns of coordinated gene expression. In: *Developmental dynamics : an official publication of the American Association of Anatomists* 236 (4), S. 961–970. DOI: 10.1002/dvdy.21099.

Bell, M. C.; Carroll, G. J.; Chapman, H. M.; Mills, J. N.; Hui, Wang (1999): Oncostatin M induces leukocyte infiltration and cartilage proteoglycan degradation in vivo in goat joints. In: *Arthritis & Rheumatism* 42 (12), S. 2543–2551. DOI: 10.1002/1529-0131(199912)42:12<2543::AID-ANR6>3.0.CO;2-W.

Biernacka, Anna; Dobaczewski, Marcin; Frangogiannis, Nikolaos G. (2011): TGF-β signaling in fibrosis. In: *Growth factors (Chur, Switzerland)* 29 (5), S. 196–202. DOI: 10.3109/08977194.2011.595714.

Blokzijl, Andries; Dahlqvist, Camilla; Reissmann, Eva; Falk, Anna; Moliner, Annalena; Lendahl, Urban; Ibáñez, Carlos F. (2003): Cross-talk between the Notch and TGF-beta signaling pathways mediated by interaction of the Notch intracellular domain with Smad3. In: *The Journal of cell biology* 163 (4), S. 723–728. DOI: 10.1083/jcb.200305112.

Bockermann, Robert; Schubert, David; Kamradt, Thomas; Holmdahl, Rikard (2005): Induction of a B-cell-dependent chronic arthritis with glucose-6-phosphate isomerase. In: *Arthritis research & therapy* 7 (6), R1316-24. DOI: 10.1186/ar1829.

Boroviak, Thorsten; Loos, Remco; Bertone, Paul; Smith, Austin; Nichols, Jennifer (2014): The ability of inner-cell-mass cells to self-renew as embryonic stem cells is acquired following epiblast specification. In: *Nature cell biology* 16 (6), S. 516–528. DOI: 10.1038/ncb2965.

Bray, Nicolas L.; Pimentel, Harold; Melsted, Páll; Pachter, Lior (2016): Near-optimal probabilistic RNA-seq quantification. In: *Nature biotechnology* 34 (5), S. 525–527. DOI: 10.1038/nbt.3519.

Browaeys, Robin; Saelens, Wouter; Saeys, Yvan (2020): NicheNet: modeling intercellular communication by linking ligands to target genes. In: *Nature methods* 17 (2), S. 159–162. DOI: 10.1038/s41592-019-0667-5.

Bruns, Lisa; Frey, Oliver; Morawietz, Lars; Landgraf, Christiane; Volkmer, Rudolf; Kamradt, Thomas (2009): Immunization with an immunodominant self-peptide derived from glucose-6-phosphate isomerase induces arthritis in DBA/1 mice. In: *Arthritis research & therapy* 11 (4), R117. DOI: 10.1186/ar2777.

Buckley, Christopher D. (2011): Why does chronic inflammation persist: An unexpected role for fibroblasts. In: *Immunology letters* 138 (1), S. 12–14. DOI: 10.1016/j.imlet.2011.02.010.

Buckley, Christopher D.; McGettrick, Helen M. (2018): Leukocyte trafficking between stromal compartments: lessons from rheumatoid arthritis. In: *Nature reviews. Rheumatology* 14 (8), S. 476–487. DOI: 10.1038/s41584-018-0042-4.

Buffrénil, Vivian de; Quilhac, Alexandra (2021): An Overview of the Embryonic Development of the Bony Skeleton. In: Vivian de Buffrénil, Louise Zylberberg, Armand J. de Ricqlès, Kevin Padian, Michel Laurin and Alexandra Quilhac (Hg.): Vertebrate Skeletal Histology and Paleohistology. Boca Raton: CRC Press, S. 29–38.

Butler, Andrew; Hoffman, Paul; Smibert, Peter; Papalexi, Efthymia; Satija, Rahul (2018): Integrating single-cell transcriptomic data across different conditions, technologies, and species. In: *Nature biotechnology* 36 (5), S. 411–420. DOI: 10.1038/nbt.4096.

Cameron, T. L.; Gresshoff, I. L.; Bell, K. M.; Piróg, K. A.; Sampurno, L.; Hartley, C. L. et al. (2015): Cartilage-specific ablation of XBP1 signaling in mouse results in a chondrodysplasia characterized by reduced chondrocyte proliferation and delayed cartilage maturation and mineralization. In: *Osteoarthritis and cartilage* 23 (4), S. 661–670. DOI: 10.1016/j.joca.2015.01.001.

Cawston, T. E.; Curry, V. A.; Summers, C. A.; Clark, I. M.; Riley, G. P.; Life, P. F. et al. (1998): The role of oncostatin M in animal and human connective tissue collagen turnover and its localization within the rheumatoid joint. In: *Arthritis & Rheumatism* 41 (10), S. 1760–1771. DOI: 10.1002/1529-0131(199810)41:10<1760::AID-ART8>3.0.CO;2-M.

Chan, Chun Ming; Macdonald, Christopher D.; Litherland, Gary J.; Wilkinson, David J.; Skelton, Andrew; Europe-Finner, G. Nicholas; Rowan, Andrew D. (2017): Cytokine-induced MMP13 Expression in Human Chondrocytes Is Dependent on Activating

Transcription Factor 3 (ATF3) Regulation. In: *The Journal of biological chemistry* 292 (5), S. 1625–1636. DOI: 10.1074/jbc.M116.756601.

Chazaud, Claire; Yamanaka, Yojiro; Pawson, Tony; Rossant, Janet (2006): Early lineage segregation between epiblast and primitive endoderm in mouse blastocysts through the Grb2-MAPK pathway. In: *Developmental cell* 10 (5), S. 615–624. DOI: 10.1016/j.devcel.2006.02.020.

Chen, Canhe; Shen, Michael M. (2004): Two modes by which Lefty proteins inhibit nodal signaling. In: *Current biology : CB* 14 (7), S. 618–624. DOI: 10.1016/j.cub.2004.02.042.

Chen, Canhe; Ware, Stephanie M.; Sato, Akira; Houston-Hawkins, Dianne E.; Habas, Raymond; Matzuk, Martin M. et al. (2006): The Vg1-related protein Gdf3 acts in a Nodal signaling pathway in the pre-gastrulation mouse embryo. In: *Development (Cambridge, England)* 133 (2), S. 319–329. DOI: 10.1242/dev.02210.

Chen, Edward Y.; Tan, Christopher M.; Kou, Yan; Duan, Qiaonan; Wang, Zichen; Meirelles, Gabriela Vaz et al. (2013): Enrichr: interactive and collaborative HTML5 gene list enrichment analysis tool. In: *BMC bioinformatics* 14, S. 128. DOI: 10.1186/1471-2105-14-128.

Chen, Geng; Schell, John Paul; Benitez, Julio Aguila; Petropoulos, Sophie; Yilmaz, Marlene; Reinius, Björn et al. (2016a): Single-cell analyses of X Chromosome inactivation dynamics and pluripotency during differentiation. In: *Genome research* 26 (10), S. 1342–1354. DOI: 10.1101/gr.201954.115.

Chen, Jun; Wright, Kerry; Davis, John M.; Jeraldo, Patricio; Marietta, Eric V.; Murray, Joseph et al. (2016b): An expansion of rare lineage intestinal microbes characterizes rheumatoid arthritis. In: *Genome medicine* 8 (1), S. 43. DOI: 10.1186/s13073-016-0299-7.

Chen, Shoujun; Oldberg, Ake; Chakravarti, Shukti; Birk, David E. (2010): Fibromodulin regulates collagen fibrillogenesis during peripheral corneal development. In: *Developmental dynamics : an official publication of the American Association of Anatomists* 239 (3), S. 844–854. DOI: 10.1002/dvdy.22216.

Chen, Y.; Li, X.; Eswarakumar, V. P.; Seger, R.; Lonai, P. (2000): Fibroblast growth factor (FGF) signaling through PI 3-kinase and Akt/PKB is required for embryoid body differentiation. In: *Oncogene* 19 (33), S. 3750–3756. DOI: 10.1038/sj.onc.1203726.

Cheng, Shangli; Pei, Yu; He, Liqun; Peng, Guangdun; Reinius, Björn; Tam, Patrick P. L. et al. (2019): Single-Cell RNA-Seq Reveals Cellular Heterogeneity of Pluripotency Transition and X Chromosome Dynamics during Early Mouse Development. In: *Cell reports* 26 (10), 2593-2607.e3. DOI: 10.1016/j.celrep.2019.02.031.

Cheng, Simon K.; Olale, Felix; Brivanlou, Ali H.; Schier, Alexander F. (2004): Lefty blocks a subset of TGFbeta signals by antagonizing EGF-CFC coreceptors. In: *PLoS biology* 2 (2), E30. DOI: 10.1371/journal.pbio.0020030.

Chou, Ching-Heng; Jain, Vaibhav; Gibson, Jason; Attarian, David E.; Haraden, Collin A.; Yohn, Christopher B. et al. (2020): Synovial cell cross-talk with cartilage plays a major role in the pathogenesis of osteoarthritis. In: *Scientific reports* 10 (1), S. 10868. DOI: 10.1038/s41598-020-67730-y.

Ciruna, Brian G.; Rossant, Janet (1999): Expression of the T-box gene Eomesodermin during early mouse development. In: *Mechanisms of Development* 81 (1-2), S. 199–203. DOI: 10.1016/s0925-4773(98)00243-3.

Comes, Núria; Buie, Lakisha K.; Borrás, Teresa (2011): Evidence for a role of angiopoietin-like 7 (ANGPTL7) in extracellular matrix formation of the human trabecular meshwork: implications for glaucoma. In: *Genes to cells : devoted to molecular & cellular mechanisms* 16 (2), S. 243–259. DOI: 10.1111/j.1365-2443.2010.01483.x.

Corson, Laura Beth; Yamanaka, Yojiro; Lai, Ka-Man Venus; Rossant, Janet (2003): Spatial and temporal patterns of ERK signaling during mouse embryogenesis. In: *Development (Cambridge, England)* 130 (19), S. 4527–4537. DOI: 10.1242/dev.00669.

Croft, Adam P.; Campos, Joana; Jansen, Kathrin; Turner, Jason D.; Marshall, Jennifer; Attar, Moustafa et al. (2019): Distinct fibroblast subsets drive inflammation and damage in arthritis. In: *Nature* 570 (7760), S. 246–251. DOI: 10.1038/s41586-019-1263-7.

Culemann, Stephan; Grüneboom, Anika; Krönke, Gerhard (2019a): Origin and function of synovial macrophage subsets during inflammatory joint disease. In: *Advances in immunology* 143, S. 75–98. DOI: 10.1016/bs.ai.2019.08.006.

Culemann, Stephan; Grüneboom, Anika; Nicolás-Ávila, José Ángel; Weidner, Daniela; Lämmle, Katrin Franziska; Rothe, Tobias et al. (2019b): Locally renewing resident synovial macrophages provide a protective barrier for the joint. In: *Nature* 572 (7771), S. 670–675. DOI: 10.1038/s41586-019-1471-1.

Dahlqvist, Camilla; Blokzijl, Andries; Chapman, Gavin; Falk, Anna; Dannaeus, Karin; Ibâñez, Carlos F.; Lendahl, Urban (2003): Functional Notch signaling is required for BMP4-induced inhibition of myogenic differentiation. In: *Development (Cambridge, England)* 130 (24), S. 6089–6099. DOI: 10.1242/dev.00834.

Dang, Stephen M.; Gerecht-Nir, Sharon; Chen, Jinny; Itskovitz-Eldor, Joseph; Zandstra, Peter W. (2004): Controlled, scalable embryonic stem cell differentiation culture. In: *Stem cells (Dayton, Ohio)* 22 (3), S. 275–282. DOI: 10.1634/stemcells.22-3-275.

Di Liu; Yuan, Na; Yu, Guimei; Song, Ge; Chen, Yan (2017): Can rheumatoid arthritis ever cease to exist: a review of various therapeutic modalities to maintain drug-free remission? In: *American Journal of Translational Research* 9 (8), S. 3758–3775.

Dobin, Alexander; Davis, Carrie A.; Schlesinger, Felix; Drenkow, Jorg; Zaleski, Chris; Jha, Sonali et al. (2013): STAR: ultrafast universal RNA-seq aligner. In: *Bioinformatics (Oxford, England)* 29 (1), S. 15–21. DOI: 10.1093/bioinformatics/bts635.

Dodge, George R.; Diaz, Arturo; Sanz-Rodriguez, Cesar; Reginato, Anthony M.; Jimenez, Sergio A. (1998): Effects of interferon-? and tumor necrosis factor ? on the expression of the genes encoding aggrecan, biglycan, and decorin core proteins in cultured human chondrocytes. In: *Arthritis & Rheumatism* 41 (2), S. 274–283. DOI: 10.1002/1529-0131(199802)41:2<274::AID-ART11>3.0.CO;2-Z.

Doetschman, T. C.; Eistetter, H.; Katz, M.; Schmidt, W.; Kemler, R. (1985): The in vitro development of blastocyst-derived embryonic stem cell lines: formation of visceral yolk sac, blood islands and myocardium. In: *Journal of embryology and experimental morphology* 87, S. 27–45.

Donnison, Martyn; Broadhurst, Ric; Pfeffer, Peter L. (2015): Elf5 and Ets2 maintain the mouse extraembryonic ectoderm in a dosage dependent synergistic manner. In: *Developmental biology* 397 (1), S. 77–88. DOI: 10.1016/j.ydbio.2014.10.011.

Dranoff, Glenn (2004): Cytokines in cancer pathogenesis and cancer therapy. In: *Nature reviews. Cancer* 4 (1), S. 11–22. DOI: 10.1038/nrc1252.

Durinck, Steffen; Moreau, Yves; Kasprzyk, Arek; Davis, Sean; Moor, Bart de; Brazma, Alvis; Huber, Wolfgang (2005): BioMart and Bioconductor: a powerful link between biological databases and microarray data analysis. In: *Bioinformatics (Oxford, England)* 21 (16), S. 3439–3440. DOI: 10.1093/bioinformatics/bti525.

Dvash, Tamar; Mayshar, Yoav; Darr, Henia; McElhaney, Michael; Barker, Douglas; Yanuka, Ofra et al. (2004): Temporal gene expression during differentiation of human embryonic stem cells and embryoid bodies. In: *Human reproduction (Oxford, England)* 19 (12), S. 2875–2883. DOI: 10.1093/humrep/deh529.

Esner, Milan; Pachernik, Jiri; Hampl, Ales; Dvorak, Petr (2002): Targeted disruption of fibroblast growth factor receptor-1 blocks maturation of visceral endoderm and cavitation in mouse embryoid bodies. In: *The International journal of developmental biology* 46 (6), S. 817–825.

Evans, M. J.; Kaufman, M. H. (1981): Establishment in culture of pluripotential cells from mouse embryos. In: *Nature* 292 (5819), S. 154–156. DOI: 10.1038/292154a0.

Ewen-Campen, Ben; Schwager, Evelyn E.; Extavour, Cassandra G. M. (2010): The molecular machinery of germ line specification. In: *Molecular reproduction and development* 77 (1), S. 3–18. DOI: 10.1002/mrd.21091.

Fassbender, Hans Georg (1983): Histomorphological Basis of Articular Cartilage Destruction in Rheumatoid Arthritis. In: *Collagen and Related Research* 3 (2), S. 141–155. DOI: 10.1016/S0174-173X(83)80040-5.

Faust, Nicole; Varas, Florencio; Kelly, Louise M.; Heck, Susanne; Graf, Thomas (2000): Insertion of enhanced green fluorescent protein into the lysozyme gene creates mice with green fluorescent granulocytes and macrophages. In: *Blood* 96 (2), S. 719–726. DOI: 10.1182/blood.V96.2.719.

Fava, R.; Olsen, N.; Keski-Oja, J.; Moses, H.; Pincus, T. (1989): Active and latent forms of transforming growth factor beta activity in synovial effusions. In: *The Journal of experimental medicine* 169 (1), S. 291–296. DOI: 10.1084/jem.169.1.291.

Feldman, B.; Poueymirou, W.; Papaioannou, V. E.; DeChiara, T. M.; Goldfarb, M. (1995): Requirement of FGF-4 for postimplantation mouse development. In: *Science (New York, N.Y.)* 267 (5195), S. 246–249. DOI: 10.1126/science.7809630.

Filer, Andrew; Ward, Lewis S. C.; Kemble, Samuel; Davies, Christopher S.; Munir, Hafsa; Rogers, Rebekah et al. (2017): Identification of a transitional fibroblast function in very early rheumatoid arthritis. In: *Annals of the rheumatic diseases* 76 (12), S. 2105–2112. DOI: 10.1136/annrheumdis-2017-211286.

Fiorenzano, Alessandro; Pascale, Emilia; D'Aniello, Cristina; Acampora, Dario; Bassalert, Cecilia; Russo, Francesco et al. (2016): Cripto is essential to capture mouse epiblast stem cell and human embryonic stem cell pluripotency. In: *Nature communications* 7, S. 12589. DOI: 10.1038/ncomms12589.

Frey, Oliver; Reichel, Andreas; Bonhagen, Kerstin; Morawietz, Lars; Rauchhaus, Una; Kamradt, Thomas (2010): Regulatory T cells control the transition from acute into chronic inflammation in glucose-6-phosphate isomerase-induced arthritis. In: *Annals of the rheumatic diseases* 69 (8), S. 1511–1518. DOI: 10.1136/ard.2009.123422.

Friščić, Jasna; Böttcher, Martin; Reinwald, Christiane; Bruns, Heiko; Wirth, Benjamin; Popp, Samantha-Josefine et al. (2021): The complement system drives local inflammatory tissue priming by metabolic reprogramming of synovial fibroblasts. In: *Immunity* 54 (5), 1002-1021.e10. DOI: 10.1016/j.immuni.2021.03.003.

Garbers, Christoph; Aparicio-Siegmund, Samadhi; Rose-John, Stefan (2015): The IL-6/gp130/STAT3 signaling axis: recent advances towards specific inhibition. In: *Current opinion in immunology* 34, S. 75–82. DOI: 10.1016/j.coi.2015.02.008.

Garcia-Gonzalez, Miguel A.; Outeda, Patricia; Zhou, Qin; Zhou, Fang; Menezes, Luis F.; Qian, Feng et al. (2010): Pkd1 and Pkd2 are required for normal placental development. In: *PloS one* 5 (9). DOI: 10.1371/journal.pone.0012821.

Gardner, R. L. (1983): Origin and differentiation of extraembryonic tissues in the mouse. In: *International review of experimental pathology* 24, S. 63–133.

Garg, Bhavuk; Mehta, Hrishikesh M.; Wang, Borwyn; Kamel, Ralph; Horwitz, Marshall S.; Corey, Seth J. (2020): Inducible expression of a disease-associated ELANE mutation impairs granulocytic differentiation, without eliciting an unfolded protein response. In: *The Journal of biological chemistry* 295 (21), S. 7492–7500. DOI: 10.1074/jbc.RA120.012366.

Garrido, Federico; Aptsiauri, Natalia; Doorduijn, Elien M.; Garcia Lora, Angel M.; van Hall, Thorbald (2016): The urgent need to recover MHC class I in cancers for effective immunotherapy. In: *Current opinion in immunology* 39, S. 44–51. DOI: 10.1016/j.coi.2015.12.007.

Gierahn, Todd M.; Wadsworth, Marc H.; Hughes, Travis K.; Bryson, Bryan D.; Butler, Andrew; Satija, Rahul et al. (2017): Seq-Well: portable, low-cost RNA sequencing of single cells at high throughput. In: *Nature methods* 14 (4), S. 395–398. DOI: 10.1038/nmeth.4179.

Glimcher, L. H. (2010): XBP1: the last two decades. In: *Annals of the rheumatic diseases* 69 Suppl 1, i67-71. DOI: 10.1136/ard.2009.119388.

Goldman, Devorah C.; Donley, Nathan; Christian, Jan L. (2009): Genetic interaction between Bmp2 and Bmp4 reveals shared functions during multiple aspects of mouse organogenesis. In: *Mechanisms of Development* 126 (3-4), S. 117–127. DOI: 10.1016/j.mod.2008.11.008.

Gombart, Adrian F.; Kwok, Scott H.; Anderson, Karen L.; Yamaguchi, Yuji; Torbett, Bruce E.; Koeffler, H. Phillip (2003): Regulation of neutrophil and eosinophil secondary granule gene expression by transcription factors C/EBP epsilon and PU.1. In: *Blood* 101 (8), S. 3265–3273. DOI: 10.1182/blood-2002-04-1039.

Gossler, A.; Doetschman, T.; Korn, R.; Serfling, E.; Kemler, R. (1986): Transgenesis by means of blastocyst-derived embryonic stem cell lines. In: *Proceedings of the National Academy of Sciences of the United States of America* 83 (23), S. 9065–9069. DOI: 10.1073/pnas.83.23.9065.

Greene, Michael J.; Sam, Flora; Soo Hoo, Pamela T.; Patel, Rupesh S.; Seldin, David C.; Connors, Lawreen H. (2011): Evidence for a functional role of the molecular chaperone clusterin in amyloidotic cardiomyopathy. In: *The American journal of pathology* 178 (1), S. 61–68. DOI: 10.1016/j.ajpath.2010.11.015.

Grotendorst, G. R.; Smale, G.; Pencev, D. (1989): Production of transforming growth factor beta by human peripheral blood monocytes and neutrophils. In: *Journal of cellular physiology* 140 (2), S. 396–402. DOI: 10.1002/jcp.1041400226.

Guo, Qiang; Wang, Yuxiang; Xu, Dan; Nossent, Johannes; Pavlos, Nathan J.; Xu, Jiake (2018): Rheumatoid arthritis: pathological mechanisms and modern pharmacologic therapies. In: *Bone research* 6, S. 15. DOI: 10.1038/s41413-018-0016-9.

Haffner-Krausz, Rebecca; Gorivodsky, Marat; Chen, Yali; Lonai, Peter (1999): Expression of Fgfr2 in the early mouse embryo indicates its involvement in preimplantation development. In: *Mechanisms of Development* 85 (1-2), S. 167–172. DOI: 10.1016/s0925-4773(99)00082-9.

Hansen, Ted H.; Bouvier, Marlene (2009): MHC class I antigen presentation: learning from viral evasion strategies. In: *Nature reviews. Immunology* 9 (7), S. 503–513. DOI: 10.1038/nri2575.

Harjes, U.; Bridges, E.; Gharpure, K. M.; Roxanis, I.; Sheldon, H.; Miranda, F. et al. (2017): Antiangiogenic and tumour inhibitory effects of downregulating tumour endothelial FABP4. In: *Oncogene* 36 (7), S. 912–921. DOI: 10.1038/onc.2016.256.

Hayashi, Katsuhiko; Ohta, Hiroshi; Kurimoto, Kazuki; Aramaki, Shinya; Saitou, Mitinori (2011): Reconstitution of the mouse germ cell specification pathway in culture by pluripotent stem cells. In: *Cell* 146 (4), S. 519–532. DOI: 10.1016/j.cell.2011.06.052.

Hedbom, E.; Antonsson, P.; Hjerpe, A.; Aeschlimann, D.; Paulsson, M.; Rosa-Pimentel, E. et al. (1992): Cartilage matrix proteins. An acidic oligomeric protein (COMP) detected only in cartilage. In: *Journal of Biological Chemistry* 267 (9), S. 6132–6136. DOI: 10.1016/S0021-9258(18)42671-3.

Hino, Kenta; Saito, Atsushi; Kido, Miori; Kanemoto, Soshi; Asada, Rie; Takai, Tomoko et al. (2014): Master regulator for chondrogenesis, Sox9, regulates transcriptional activation of the endoplasmic reticulum stress transducer BBF2H7/CREB3L2 in chondrocytes. In: *The Journal of biological chemistry* 289 (20), S. 13810–13820. DOI: 10.1074/jbc.m113.543322.

Hoffman, Jackson A.; Wu, Chun-I; Merrill, Bradley J. (2013): Tcf7l1 prepares epiblast cells in the gastrulating mouse embryo for lineage specification. In: *Development (Cambridge, England)* 140 (8), S. 1665–1675. DOI: 10.1242/dev.087387.

Hogan, Brigid L.M.; Cooper, Ashley R.; Kurkinen, Markku (1980): Incorporation into Reichert's membrane of laminin-like extracellular proteins synthesized by parietal endoderm cells of the mouse embryo. In: *Developmental biology* 80 (2), S. 289–300. DOI: 10.1016/0012-1606(80)90405-4.

Höglund, Petter; Brodin, Petter (2010): Current perspectives of natural killer cell education by MHC class I molecules. In: *Nature reviews. Immunology* 10 (10), S. 724–734. DOI: 10.1038/nri2835.

Hoshino, Hideharu; Shioi, Go; Aizawa, Shinichi (2015): AVE protein expression and visceral endoderm cell behavior during anterior-posterior axis formation in mouse embryos: Asymmetry in OTX2 and DKK1 expression. In: *Developmental biology* 402 (2), S. 175–191. DOI: 10.1016/j.ydbio.2015.03.023.

Hu, Zhuting; Ott, Patrick A.; Wu, Catherine J. (2018): Towards personalized, tumour-specific, therapeutic vaccines for cancer. In: *Nature reviews. Immunology* 18 (3), S. 168–182. DOI: 10.1038/nri.2017.131.

Huang, Daosheng; Guo, Guoji; Yuan, Ping; Ralston, Amy; Sun, Lingang; Huss, Mikael et al. (2017): The role of Cdx2 as a lineage specific transcriptional repressor for pluripotent network during the first developmental cell lineage segregation. In: *Scientific reports* 7 (1), S. 17156. DOI: 10.1038/s41598-017-16009-w.

Itoh, Fumiko; Itoh, Susumu; Goumans, Marie-José; Valdimarsdottir, Gudrun; Iso, Tatsuya; Dotto, G. Paolo et al. (2004): Synergy and antagonism between Notch and BMP receptor signaling pathways in endothelial cells. In: *The EMBO Journal* 23 (3), S. 541–551. DOI: 10.1038/sj.emboj.7600065.

Itskovitz-Eldor, Joseph; Schuldiner, Maya; Karsenti, Dorit; Eden, Amir; Yanuka, Ofra; Amit, Michal et al. (2000): Differentiation of Human Embryonic Stem Cells into Embryoid Bodies Comprising the Three Embryonic Germ Layers. In: *Mol Med* 6 (2), S. 88–95. DOI: 10.1007/BF03401776.

James, Claudine G.; Woods, Anita; Underhill, T. Michael; Beier, Frank (2006): The transcription factor ATF3 is upregulated during chondrocyte differentiation and represses cyclin D1 and A gene transcription. In: *BMC molecular biology* 7, S. 30. DOI: 10.1186/1471-2199-7-30.

Janky, Rekin's; Verfaillie, Annelien; Imrichová, Hana; van de Sande, Bram; Standaert, Laura; Christiaens, Valerie et al. (2014): iRegulon: from a gene list to a gene regulatory network using large motif and track collections. In: *PLoS computational biology* 10 (7), e1003731. DOI: 10.1371/journal.pcbi.1003731.

Johnson, M. (1981): The foundation of two distinct cell lineages within the mouse morula. In: *Cell* 24 (1), S. 71–80. DOI: 10.1016/0092-8674(81)90502-x.

Kaartinen, M. T.; Pirhonen, A.; Linnala-Kankkunen, A.; Mäenpää, P. H. (1999): Cross-linking of osteopontin by tissue transglutaminase increases its collagen binding properties. In: *Journal of Biological Chemistry* 274 (3), S. 1729–1735. DOI: 10.1074/jbc.274.3.1729.

Kaiser, Franziska; Kubaczka, Caroline; Graf, Monika; Langer, Nina; Langkabel, Jan; Arévalo, Lena; Schorle, Hubert (2020): Choice of factors and medium impinge on success of ESC to TSC conversion. In: *Placenta* 90, S. 128–137. DOI: 10.1016/j.placenta.2019.12.017.

Karlsson, C.; Brantsing, C.; Egell, S.; Lindahl, A. (2008): Notch1, Jagged1, and HES5 are abundantly expressed in osteoarthritis. In: *Cells, tissues, organs* 188 (3), S. 287–298. DOI: 10.1159/000121610.

Kaufman, R. J. (1999): Stress signaling from the lumen of the endoplasmic reticulum: coordination of gene transcriptional and translational controls. In: *Genes & development* 13 (10), S. 1211–1233. DOI: 10.1101/gad.13.10.1211.

Kim, Hyung-Seok; Neugebauer, Judith; McKnite, Autumn; Tilak, Anup; Christian, Jan L. (2019): BMP7 functions predominantly as a heterodimer with BMP2 or BMP4 during mammalian embryogenesis. In: *eLife* 8. DOI: 10.7554/eLife.48872.

Kimura-Yoshida, Chiharu; Nakano, Hiroshi; Okamura, Daiji; Nakao, Kazuki; Yonemura, Shigenobu; Belo, Jose A. et al. (2005): Canonical Wnt signaling and its antagonist regulate anterior-posterior axis polarization by guiding cell migration in mouse visceral endoderm. In: *Developmental cell* 9 (5), S. 639–650. DOI: 10.1016/j.devcel.2005.09.011.

Klein, Allon M.; Mazutis, Linas; Akartuna, Ilke; Tallapragada, Naren; Veres, Adrian; Li, Victor et al. (2015): Droplet barcoding for single-cell transcriptomics applied to embryonic stem cells. In: *Cell* 161 (5), S. 1187–1201. DOI: 10.1016/j.cell.2015.04.044.

Koch, A. E.; Kunkel, S. L.; Shah, M. R.; Hosaka, S.; Halloran, M. M.; Haines, G. K. et al. (1995): Growth-related gene product alpha. A chemotactic cytokine for neutrophils in rheumatoid arthritis. In: *Journal of immunology (Baltimore, Md. : 1950)* 155 (7), S. 3660–3666.

Koch, Alisa E.; Volin, Michael V.; Woods, James M.; Kunkel, Steven L.; Connors, Matthew A.; Harlow, Lisa A. et al. (2001): Regulation of angiogenesis by the C-X-C chemokines interleukin-8 and epithelial neutrophil activating peptide 78 in the rheumatoid joint. In: *Arthritis & Rheumatism* 44 (1), S. 31–40. DOI: 10.1002/1529-0131(200101)44:1<31::AID-ANR5>3.0.CO;2-4.

Komatsu, Noriko; Takayanagi, Hiroshi (2012): Inflammation and bone destruction in arthritis: synergistic activity of immune and mesenchymal cells in joints. In: *Frontiers in immunology* 3, S. 77. DOI: 10.3389/fimmu.2012.00077.

Kondo, Shinichi; Murakami, Tomohiko; Tatsumi, Kouko; Ogata, Maiko; Kanemoto, Soshi; Otori, Kumi et al. (2005): OASIS, a CREB/ATF-family member, modulates UPR signalling in astrocytes. In: *Nature cell biology* 7 (2), S. 186–194. DOI: 10.1038/ncb1213.

Konttinen, Y. T.; Ainola, M.; Valleala, H.; Ma, J.; Ida, H.; Mandelin, J. et al. (1999): Analysis of 16 different matrix metalloproteinases (MMP-1 to MMP-20) in the synovial membrane: different profiles in trauma and rheumatoid arthritis. In: *Annals of the rheumatic diseases* 58 (11), S. 691–697. DOI: 10.1136/ard.58.11.691.

Korganow, Anne-Sophie; Ji, Hong; Mangialaio, Sara; Duchatelle, Véronique; Pelanda, Roberta; Martin, Thierry et al. (1999): From Systemic T Cell Self-Reactivity to Organ-Specific Autoimmune Disease via Immunoglobulins. In: *Immunity* 10 (4), S. 451–461. DOI: 10.1016/S1074-7613(00)80045-X.

Koyama, Eiki; Shibukawa, Yoshihiro; Nagayama, Motohiko; Sugito, Hiroki; Young, Blanche; Yuasa, Takahito et al. (2008): A distinct cohort of progenitor cells participates in synovial joint and articular cartilage formation during mouse limb skeletogenesis. In: *Developmental biology* 316 (1), S. 62–73. DOI: 10.1016/j.ydbio.2008.01.012.

Kumar, Amit; Lualdi, Margaret; Lyozin, George T.; Sharma, Prashant; Loncarek, Jadranka; Fu, Xin-Yuan; Kuehn, Michael R. (2015): Nodal signaling from the visceral endoderm is required to maintain Nodal gene expression in the epiblast and drive DVE/AVE migration. In: *Developmental biology* 400 (1), S. 1–9. DOI: 10.1016/j.ydbio.2014.12.016.

Kumkumian, G. K.; Lafyatis, R.; Remmers, E. F.; Case, J. P.; Kim, S. J.; Wilder, R. L. (1989): Platelet-derived growth factor and IL-1 interactions in rheumatoid arthritis. Regulation of synoviocyte proliferation, prostaglandin production, and collagenase transcription. In: *Journal of immunology (Baltimore, Md. : 1950)* 143 (3), S. 833–837.

Kunath, Tilo; Arnaud, Danielle; Uy, Gary D.; Okamoto, Ikuhiro; Chureau, Corinne; Yamanaka, Yojiro et al. (2005): Imprinted X-inactivation in extra-embryonic endoderm cell lines from mouse blastocysts. In: *Development (Cambridge, England)* 132 (7), S. 1649–1661. DOI: 10.1242/dev.01715.

Kuo, David; Ding, Jennifer; Cohn, Ian S.; Zhang, Fan; Wei, Kevin; Rao, Deepak A. et al. (2019): HBEGF+ macrophages in rheumatoid arthritis induce fibroblast invasiveness. In: *Science translational medicine* 11 (491). DOI: 10.1126/scitranslmed.aau8587.

Kurowska-Stolarska, Mariola; Alivernini, Stefano (2017): Synovial tissue macrophages: friend or foe? In: *RMD open* 3 (2), e000527. DOI: 10.1136/rmdopen-2017-000527.

Kwiatkowska, J.; Cislo, M. (1975): Some properties of human uterine myoma phosphofructokinase. In: *Archivum immunologiae et therapiae experimentalis* 23 (5), S. 715–723.

Lachmann, Alexander; Xu, Huilei; Krishnan, Jayanth; Berger, Seth I.; Mazloom, Amin R.; Ma'ayan, Avi (2010): ChEA: transcription factor regulation inferred from integrating

genome-wide ChIP-X experiments. In: *Bioinformatics (Oxford, England)* 26 (19), S. 2438–2444. DOI: 10.1093/bioinformatics/btq466.

Langkabel, Jan; Horne, Arik; Bonaguro, Lorenzo; Holsten, Lisa; Hesse, Tatiana; Knaus, Alexej et al. (2021): Induction of Rosette-to-Lumen stage embryoids using reprogramming paradigms in ESCs. In: *Nature communications* 12 (1), S. 7322. DOI: 10.1038/s41467-021-27586-w.

Larue, L.; Antos, C.; Butz, S.; Huber, O.; Delmas, V.; Dominis, M.; Kemler, R. (1996): A role for cadherins in tissue formation. In: *Development (Cambridge, England)* 122 (10), S. 3185–3194. DOI: 10.1242/dev.122.10.3185.

Lawson, Kirstie A.; Dunn, N. Ray; Roelen, Bernard A.J.; Zeinstra, Laura M.; Davis, Angela M.; Wright, Christopher V.E. et al. (1999): Bmp4 is required for the generation of primordial germ cells in the mouse embryo. In: *Genes & development* 13 (4), S. 424–436.

Leeuwenberg, J. F.; Smeets, E. F.; Neefjes, J. J.; Shaffer, M. A.; Cinek, T.; Jeunhomme, T. M. et al. (1992): E-selectin and intercellular adhesion molecule-1 are released by activated human endothelial cells in vitro. In: *Immunology* 77 (4), S. 543–549.

Li, W. Q.; Zafarullah, M. (1998): Oncostatin M up-regulates tissue inhibitor of metalloproteinases-3 gene expression in articular chondrocytes via de novo transcription, protein synthesis, and tyrosine kinase- and mitogen-activated protein kinase-dependent mechanisms. In: *Journal of immunology (Baltimore, Md. : 1950)* 161 (9), S. 5000–5007.

Li, X.; Chen, Y.; Schéele, S.; Arman, E.; Haffner-Krausz, R.; Ekblom, P.; Lonai, P. (2001): Fibroblast growth factor signaling and basement membrane assembly are connected during epithelial morphogenesis of the embryoid body. In: *The Journal of cell biology* 153 (4), S. 811–822. DOI: 10.1083/jcb.153.4.811.

Lim, Chin Yan; Tam, Wai-Leong; Zhang, Jinqiu; Ang, Haw Siang; Jia, Hui; Lipovich, Leonard et al. (2008): Sall4 regulates distinct transcription circuitries in different blastocyst-derived stem cell lineages. In: *Cell stem cell* 3 (5), S. 543–554. DOI: 10.1016/j.stem.2008.08.004.

Lin, Jiangwei; Khan, Mona; Zapiec, Bolek; Mombaerts, Peter (2016): Efficient derivation of extraembryonic endoderm stem cell lines from mouse postimplantation embryos. In: *Scientific reports* 6, S. 39457. DOI: 10.1038/srep39457.

Liu, Fangchao; He, Jiang; Gu, Dongfeng; Rao, Dabeeru C.; Huang, Jianfeng; Hixson, James E. et al. (2015): Associations of Endothelial System Genes With Blood Pressure Changes and Hypertension Incidence: The GenSalt Study. In: *American journal of hypertension* 28 (6), S. 780–788. DOI: 10.1093/ajh/hpu223.

Liu, Hui; Zhu, Yuanli; Gao, Yutong; Qi, Dahu; Zhao, Liming; Zhao, Libo et al. (2020): NR1D1 modulates synovial inflammation and bone destruction in rheumatoid arthritis. In: *Cell death & disease* 11 (2), S. 129. DOI: 10.1038/s41419-020-2314-6.

Lotz, M.; Guerne, P. A. (1991): Interleukin-6 induces the synthesis of tissue inhibitor of metalloproteinases-1/erythroid potentiating activity (TIMP-1/EPA). In: *Journal of Biological Chemistry* 266 (4), S. 2017–2020.

Lu, Pengfei; Takai, Ken; Weaver, Valerie M.; Werb, Zena (2011): Extracellular matrix degradation and remodeling in development and disease. In: *Cold Spring Harbor perspectives in biology* 3 (12). DOI: 10.1101/cshperspect.a005058.

Lu, R.; Yang, P.; O'Hare, P.; Misra, V. (1997): Luman, a new member of the CREB/ATF family, binds to herpes simplex virus VP16-associated host cellular factor. In: *Molecular and cellular biology* 17 (9), S. 5117–5126. DOI: 10.1128/MCB.17.9.5117.

Lun, Aaron T. L.; McCarthy, Davis J.; Marioni, John C. (2016): A step-by-step workflow for low-level analysis of single-cell RNA-seq data with Bioconductor. In: *F1000Research* 5, S. 2122. DOI: 10.12688/f1000research.9501.2.

Macosko, Evan Z.; Basu, Anindita; Satija, Rahul; Nemesh, James; Shekhar, Karthik; Goldman, Melissa et al. (2015): Highly Parallel Genome-wide Expression Profiling of Individual Cells Using Nanoliter Droplets. In: *Cell* 161 (5), S. 1202–1214. DOI: 10.1016/j.cell.2015.05.002.

Malleshaiah, Mohan; Padi, Megha; Rué, Pau; Quackenbush, John; Martinez-Arias, Alfonso; Gunawardena, Jeremy (2016): Nac1 Coordinates a Sub-network of Pluripotency Factors to Regulate Embryonic Stem Cell Differentiation. In: *Cell reports* 14 (5), S. 1181–1194. DOI: 10.1016/j.celrep.2015.12.101.

Mao, Bingyu; Wu, Wei; Davidson, Gary; Marhold, Joachim; Li, Mingfa; Mechler, Bernard M. et al. (2002): Kremen proteins are Dickkopf receptors that regulate Wnt/beta-catenin signalling. In: *Nature* 417 (6889), S. 664–667. DOI: 10.1038/nature756.

Marcelino, J.; Carpten, J. D.; Suwairi, W. M.; Gutierrez, O. M.; Schwartz, S.; Robbins, C. et al. (1999): CACP, encoding a secreted proteoglycan, is mutated in camptodactyly-arthropathy-coxa vara-pericarditis syndrome. In: *Nature genetics* 23 (3), S. 319–322. DOI: 10.1038/15496.

Martin, G. R. (1981): Isolation of a pluripotent cell line from early mouse embryos cultured in medium conditioned by teratocarcinoma stem cells. In: *Proceedings of the National Academy of Sciences of the United States of America* 78 (12), S. 7634–7638. DOI: 10.1073/pnas.78.12.7634.

Matsumoto, I.; Staub, A.; Benoist, C.; Mathis, D. (1999): Arthritis provoked by linked T and B cell recognition of a glycolytic enzyme. In: *Science (New York, N.Y.)* 286 (5445), S. 1732–1735. DOI: 10.1126/science.286.5445.1732.

Maurer, Jochen; Nelson, Brandon; Ceceña, Grace; Bajpai, Ruchi; Mercola, Mark; Terskikh, Alexey; Oshima, Robert G. (2008): Contrasting expression of keratins in mouse and human embryonic stem cells. In: *PloS one* 3 (10), e3451. DOI: 10.1371/journal.pone.0003451#:~:text=October%2020%2C%202008-.

McInnes, Iain B.; Schett, Georg (2011): The pathogenesis of rheumatoid arthritis. In: *The New England journal of medicine* 365 (23), S. 2205–2219. DOI: 10.1056/NEJMra1004965.

Medzhitov, R.; Janeway, C. (2000): Innate immune recognition: mechanisms and pathways. In: *Immunological reviews* 173, S. 89–97. DOI: 10.1034/j.1600-065x.2000.917309.x.

Middleton, Jim; Americh, Laure; Gayon, Regis; Julien, Denis; Mansat, Michel; Mansat, Pierre et al. (2005): A comparative study of endothelial cell markers expressed in chronically inflamed human tissues: MECA-79, Duffy antigen receptor for chemokines, von Willebrand factor, CD31, CD34, CD105 and CD146. In: *The Journal of pathology* 206 (3), S. 260–268. DOI: 10.1002/path.1788.

MINTZ, B.; RUSSELL, E. S. (1957): Gene-induced embryological modifications of primordial germ cells in the mouse. In: *The Journal of experimental zoology* 134 (2), S. 207–237. DOI: 10.1002/jez.1401340202.

Mitsui, Kaoru; Tokuzawa, Yoshimi; Itoh, Hiroaki; Segawa, Kohichi; Murakami, Mirei; Takahashi, Kazutoshi et al. (2003): The Homeoprotein Nanog Is Required for Maintenance of Pluripotency in Mouse Epiblast and ES Cells. In: *Cell* 113 (5), S. 631–642. DOI: 10.1016/s0092-8674(03)00393-3.

Miyazono, Kohei; Maeda, Shingo; Imamura, Takeshi (2005): BMP receptor signaling: transcriptional targets, regulation of signals, and signaling cross-talk. In: *Cytokine & growth factor reviews* 16 (3), S. 251–263. DOI: 10.1016/j.cytogfr.2005.01.009.

Mizoguchi, Fumitaka; Slowikowski, Kamil; Wei, Kevin; Marshall, Jennifer L.; Rao, Deepak A.; Chang, Sook Kyung et al. (2018): Functionally distinct disease-associated fibroblast subsets in rheumatoid arthritis. In: *Nature communications* 9 (1), S. 789. DOI: 10.1038/s41467-018-02892-y.

Mohammed, Hisham; Hernando-Herraez, Irene; Savino, Aurora; Scialdone, Antonio; Macaulay, Iain; Mulas, Carla et al. (2017): Single-Cell Landscape of Transcriptional

Heterogeneity and Cell Fate Decisions during Mouse Early Gastrulation. In: *Cell reports* 20 (5), S. 1215–1228. DOI: 10.1016/j.celrep.2017.07.009.

Mori, Tomoaki; Miyamoto, Takeshi; Yoshida, Hideyuki; Asakawa, Mayoko; Kawasumi, Miyuri; Kobayashi, Takashi et al. (2011): IL-1β and TNFα-initiated IL-6-STAT3 pathway is critical in mediating inflammatory cytokines and RANKL expression in inflammatory arthritis. In: *International immunology* 23 (11), S. 701–712. DOI: 10.1093/intimm/dxr077.

Mosser, David M.; Hamidzadeh, Kajal; Goncalves, Ricardo (2021): Macrophages and the maintenance of homeostasis. In: *Cellular & molecular immunology* 18 (3), S. 579–587. DOI: 10.1038/s41423-020-00541-3.

Mulas, Carla; Chia, Gloryn; Jones, Kenneth Alan; Hodgson, Andrew Christopher; Stirparo, Giuliano Giuseppe; Nichols, Jennifer (2018): Oct4 regulates the embryonic axis and coordinates exit from pluripotency and germ layer specification in the mouse embryo. In: *Development (Cambridge, England)* 145 (12). DOI: 10.1242/dev.159103.

Munter, W. de; Geven, E. J. W.; Blom, A. B.; Walgreen, B.; Helsen, M. M. A.; Joosten, L. A. B. et al. (2017): Synovial macrophages promote TGF-β signaling and protect against influx of S100A8/S100A9-producing cells after intra-articular injections of oxidized low-density lipoproteins. In: *Osteoarthritis and cartilage* 25 (1), S. 118–127. DOI: 10.1016/j.joca.2016.07.020.

Murray, P.; Edgar, D. (2000): Regulation of programmed cell death by basement membranes in embryonic development. In: *The Journal of cell biology* 150 (5), S. 1215–1221. DOI: 10.1083/jcb.150.5.1215.

Nagase, Hideaki; Visse, Robert; Murphy, Gillian (2006): Structure and function of matrix metalloproteinases and TIMPs. In: *Cardiovascular research* 69 (3), S. 562–573. DOI: 10.1016/j.cardiores.2005.12.002.

Nagy, György; van Vollenhoven, Ronald F. (2015): Sustained biologic-free and drug-free remission in rheumatoid arthritis, where are we now? In: *Arthritis research & therapy* 17, S. 181. DOI: 10.1186/s13075-015-0707-1.

Neagu, Alex; van Genderen, Emiel; Escudero, Irene; Verwegen, Lucas; Kurek, Dorota; Lehmann, Johannes et al. (2020): In vitro capture and characterization of embryonic rosette-stage pluripotency between naive and primed states. In: *Nature cell biology* 22 (5), S. 534–545. DOI: 10.1038/s41556-020-0508-x.

Nestorowa, Sonia; Hamey, Fiona K.; Pijuan Sala, Blanca; Diamanti, Evangelia; Shepherd, Mairi; Laurenti, Elisa et al. (2016): A single-cell resolution map of mouse hematopoietic stem and progenitor cell differentiation. In: *Blood* 128 (8), e20-31. DOI: 10.1182/blood-2016-05-716480.

Ngo, S. T.; Steyn, F. J.; McCombe, P. A. (2014): Gender differences in autoimmune disease. In: *Frontiers in neuroendocrinology* 35 (3), S. 347–369. DOI: 10.1016/j.yfrne.2014.04.004.

Ngondo, Richard Patryk; Cirera-Salinas, Daniel; Yu, Jian; Wischnewski, Harry; Bodak, Maxime; Vandormael-Pournin, Sandrine et al. (2018): Argonaute 2 Is Required for Extra-embryonic Endoderm Differentiation of Mouse Embryonic Stem Cells. In: *Stem cell reports* 10 (2), S. 461–476. DOI: 10.1016/j.stemcr.2017.12.023.

Niakan, Kathy K.; Schrode, Nadine; Cho, Lily T. Y.; Hadjantonakis, Anna-Katerina (2013): Derivation of extraembryonic endoderm stem (XEN) cells from mouse embryos and embryonic stem cells. In: *Nature protocols* 8 (6), S. 1028–1041. DOI: 10.1038/nprot.2013.049.

Nichols, Jennifer; Smith, Austin (2009): Naive and primed pluripotent states. In: *Cell stem cell* 4 (6), S. 487–492. DOI: 10.1016/j.stem.2009.05.015.

Niswander, L.; Martin, G. R. (1992): Fgf-4 expression during gastrulation, myogenesis, limb and tooth development in the mouse. In: *Development (Cambridge, England)* 114 (3), S. 755–768.

Niwa, Hitoshi; Toyooka, Yayoi; Shimosato, Daisuke; Strumpf, Dan; Takahashi, Kadue; Yagi, Rika; Rossant, Janet (2005): Interaction between Oct3/4 and Cdx2 determines trophectoderm differentiation. In: *Cell* 123 (5), S. 917–929. DOI: 10.1016/j.cell.2005.08.040.

Nizet, V.; Ohtake, T.; Lauth, X.; Trowbridge, J.; Rudisill, J.; Dorschner, R. A. et al. (2001): Innate antimicrobial peptide protects the skin from invasive bacterial infection. In: *Nature* 414 (6862), S. 454–457. DOI: 10.1038/35106587.

Nowotschin, Sonja; Costello, Ita; Piliszek, Anna; Kwon, Gloria S.; Mao, Chai-an; Klein, William H. et al. (2013): The T-box transcription factor Eomesodermin is essential for AVE induction in the mouse embryo. In: *Genes & development* 27 (9), S. 997–1002. DOI: 10.1101/gad.215152.113.

O'Neil, Liam J.; Kaplan, Mariana J. (2019): Neutrophils in Rheumatoid Arthritis: Breaking Immune Tolerance and Fueling Disease. In: *Trends in molecular medicine* 25 (3), S. 215–227. DOI: 10.1016/j.molmed.2018.12.008.

Orr, Carl; Vieira-Sousa, Elsa; Boyle, David L.; Buch, Maya H.; Buckley, Christopher D.; Cañete, Juan D. et al. (2017): Synovial tissue research: a state-of-the-art review. In: *Nature reviews. Rheumatology* 13 (10), S. 630. DOI: 10.1038/nrrheum.2017.161.

Paca, Agnieszka; Séguin, Cheryle A.; Clements, Melanie; Ryczko, Michael; Rossant, Janet; Rodriguez, Tristan A.; Kunath, Tilo (2012): BMP signaling induces visceral endoderm differentiation of XEN cells and parietal endoderm. In: *Developmental biology* 361 (1), S. 90–102. DOI: 10.1016/j.ydbio.2011.10.013.

Parkin, Jacqueline; Cohen, Bryony (2001): An overview of the immune system. In: *The Lancet* 357 (9270), S. 1777–1789. DOI: 10.1016/S0140-6736(00)04904-7.

Parsonage, Greg; Filer, Andrew D.; Haworth, Oliver; Nash, Gerard B.; Rainger, G. Ed; Salmon, Michael; Buckley, Christopher D. (2005): A stromal address code defined by fibroblasts. In: *Trends in immunology* 26 (3), S. 150–156. DOI: 10.1016/j.it.2004.11.014.

Payer, Bernhard; Saitou, Mitinori; Barton, Sheila C.; Thresher, Rosemary; Dixon, John P. C.; Zahn, Dirk et al. (2003): Stella is a maternal effect gene required for normal early development in mice. In: *Current biology : CB* 13 (23), S. 2110–2117. DOI: 10.1016/j.cub.2003.11.026.

Peitz, Michael; Jäger, Richard; Patsch, Christoph; Jäger, Andrea; Egert, Angela; Schorle, Hubert; Edenhofer, Frank (2007): Enhanced purification of cell-permeant Cre and germline transmission after transduction into mouse embryonic stem cells. In: *Genesis (New York, N.Y. : 2000)* 45 (8), S. 508–517. DOI: 10.1002/dvg.20321.

Perea-Gomez, A.; Lawson, K. A.; Rhinn, M.; Zakin, L.; Brulet, P.; Mazan, S.; Ang, S. L. (2001): Otx2 is required for visceral endoderm movement and for the restriction of posterior signals in the epiblast of the mouse embryo. In: *Development (Cambridge, England)* 128 (5), S. 753–765. DOI: 10.1242/dev.128.5.753.

Picelli, Simone; Björklund, Asa K.; Reinius, Björn; Sagasser, Sven; Winberg, Gösta; Sandberg, Rickard (2014): Tn5 transposase and tagmentation procedures for massively scaled sequencing projects. In: *Genome research* 24 (12), S. 2033–2040. DOI: 10.1101/gr.177881.114.

Picelli, Simone; Björklund, Åsa K.; Faridani, Omid R.; Sagasser, Sven; Winberg, Gösta; Sandberg, Rickard (2013): Smart-seq2 for sensitive full-length transcriptome profiling in single cells. In: *Nature methods* 10 (11), S. 1096–1098. DOI: 10.1038/nmeth.2639.

Pijuan-Sala, Blanca; Griffiths, Jonathan A.; Guibentif, Carolina; Hiscock, Tom W.; Jawaid, Wajid; Calero-Nieto, Fernando J. et al. (2019): A single-cell molecular map of mouse gastrulation and early organogenesis. In: *Nature* 566 (7745), S. 490–495. DOI: 10.1038/s41586-019-0933-9.

Plusa, Berenika; Piliszek, Anna; Frankenberg, Stephen; Artus, Jérôme; Hadjantonakis, Anna-Katerina (2008): Distinct sequential cell behaviours direct primitive endoderm

formation in the mouse blastocyst. In: *Development (Cambridge, England)* 135 (18), S. 3081–3091. DOI: 10.1242/dev.021519.

Posfai, Eszter; Petropoulos, Sophie; Barros, Flavia Regina Oliveira de; Schell, John Paul; Jurisica, Igor; Sandberg, Rickard et al. (2017): Position- and Hippo signaling-dependent plasticity during lineage segregation in the early mouse embryo. In: *eLife* 6. DOI: 10.7554/eLife.22906.

Posfai, Eszter; Schell, John Paul; Janiszewski, Adrian; Rovic, Isidora; Murray, Alexander; Bradshaw, Brian et al. (2021): Evaluating totipotency using criteria of increasing stringency. In: *Nature cell biology* 23 (1), S. 49–60. DOI: 10.1038/s41556-020-00609-2.

Pullig, Oliver; Weseloh, Gerd; Gauer, Stefan; Swoboda, Bernd (2000): Osteopontin is expressed by adult human osteoarthritic chondrocytes: protein and mRNA analysis of normal and osteoarthritic cartilage. In: *Matrix Biology* 19 (3), S. 245–255. DOI: 10.1016/s0945-053x(00)00068-8.

Ramirez-Montagut, Teresa; Blachere, Nathalie E.; Sviderskaya, Elena V.; Bennett, Dorothy C.; Rettig, Wolfgang J.; Garin-Chesa, Pilar; Houghton, Alan N. (2004): FAPalpha, a surface peptidase expressed during wound healing, is a tumor suppressor. In: *Oncogene* 23 (32), S. 5435–5446. DOI: 10.1038/sj.onc.1207730.

Reubinoff, B. E.; Pera, M. F.; Fong, C. Y.; Trounson, A.; Bongso, A. (2000): Embryonic stem cell lines from human blastocysts: somatic differentiation in vitro. In: *Nature biotechnology* 18 (4), S. 399–404. DOI: 10.1038/74447.

Rhee, David K.; Marcelino, Jose; Baker, MacArthur; Gong, Yaoqin; Smits, Patrick; Lefebvre, Véronique et al. (2005): The secreted glycoprotein lubricin protects cartilage surfaces and inhibits synovial cell overgrowth. In: *The Journal of clinical investigation* 115 (3), S. 622–631. DOI: 10.1172/JCI22263.

Ricklin, Daniel; Hajishengallis, George; Yang, Kun; Lambris, John D. (2010): Complement: a key system for immune surveillance and homeostasis. In: *Nature immunology* 11 (9), S. 785–797. DOI: 10.1038/ni.1923.

Ritchie, Matthew E.; Phipson, Belinda; Di Wu; Hu, Yifang; Law, Charity W.; Shi, Wei; Smyth, Gordon K. (2015): limma powers differential expression analyses for RNA-sequencing and microarray studies. In: *Nucleic acids research* 43 (7), e47. DOI: 10.1093/nar/gkv007.

Rivron, Nicolas C.; Frias-Aldeguer, Javier; Vrij, Erik J.; Boisset, Jean-Charles; Korving, Jeroen; Vivié, Judith et al. (2018): Blastocyst-like structures generated solely from stem cells. In: *Nature* 557 (7703), S. 106–111. DOI: 10.1038/s41586-018-0051-0.

Rock, Kenneth L.; Reits, Eric; Neefjes, Jacques (2016): Present Yourself! By MHC Class I and MHC Class II Molecules. In: *Trends in immunology* 37 (11), S. 724–737. DOI: 10.1016/j.it.2016.08.010.

Rodriguez, Tristan A.; Srinivas, Shankar; Clements, Melanie P.; Smith, James C.; Beddington, Rosa S. P. (2005): Induction and migration of the anterior visceral endoderm is regulated by the extra-embryonic ectoderm. In: *Development (Cambridge, England)* 132 (11), S. 2513–2520. DOI: 10.1242/dev.01847.

Rosner, M. H.; Vigano, M. A.; Ozato, K.; Timmons, P. M.; Poirier, F.; Rigby, P. W.; Staudt, L. M. (1990): A POU-domain transcription factor in early stem cells and germ cells of the mammalian embryo. In: *Nature* 345 (6277), S. 686–692. DOI: 10.1038/345686a0.

Rossant, Janet; Tam, Patrick P. L. (2021): Opportunities and challenges with stem cell-based embryo models. In: *Stem cell reports* 16 (5), S. 1031–1038. DOI: 10.1016/j.stemcr.2021.02.002.

Rountree, Ryan B.; Schoor, Michael; Chen, Hao; Marks, Melissa E.; Harley, Vincent; Mishina, Yuji; Kingsley, David M. (2004): BMP receptor signaling is required for postnatal maintenance of articular cartilage. In: *PLoS biology* 2 (11), e355. DOI: 10.1371/journal.pbio.0020355.

Rugg-Gunn, Peter J.; Cox, Brian J.; Lanner, Fredrik; Sharma, Parveen; Ignatchenko, Vladimir; McDonald, Angela C. H. et al. (2012): Cell-surface proteomics identifies lineage-specific markers of embryo-derived stem cells. In: *Developmental cell* 22 (4), S. 887–901. DOI: 10.1016/j.devcel.2012.01.005.

Saito, Atsushi; Hino, Shin-ichiro; Murakami, Tomohiko; Kanemoto, Soshi; Kondo, Shinichi; Saitoh, Masahiro et al. (2009): Regulation of endoplasmic reticulum stress response by a BBF2H7-mediated Sec23a pathway is essential for chondrogenesis. In: *Nature cell biology* 11 (10), S. 1197–1204. DOI: 10.1038/ncb1962.

Saito, Atsushi; Kanemoto, Soshi; Zhang, Yizhou; Asada, Rie; Hino, Kenta; Imaizumi, Kazunori (2014): Chondrocyte proliferation regulated by secreted luminal domain of ER stress transducer BBF2H7/CREB3L2. In: *Molecular cell* 53 (1), S. 127–139. DOI: 10.1016/j.molcel.2013.11.008.

Salter, D. M.; Millward-Sadler, S. J.; Nuki, G.; Wright, M. O. (2001): Integrin-interleukin-4 mechanotransduction pathways in human chondrocytes. In: *Clinical orthopaedics and related research* (391 Suppl), S49-60. DOI: 10.1097/00003086-200110001-00006.

Savic, Sinisa; Ouboussad, Lylia; Dickie, Laura J.; Geiler, Janina; Wong, Chi; Doody, Gina M. et al. (2014): TLR dependent XBP-1 activation induces an autocrine loop in rheumatoid

arthritis synoviocytes. In: *Journal of autoimmunity* 50, S. 59–66. DOI: 10.1016/j.jaut.2013.11.002.

Schenten, Dominik; Medzhitov, Ruslan (2011): The control of adaptive immune responses by the innate immune system. In: *Advances in immunology* 109, S. 87–124. DOI: 10.1016/B978-0-12-387664-5.00003-0.

Scherer, Hans Ulrich; Huizinga, Tom W. J.; Krönke, Gerhard; Schett, Georg; Toes, Rene E. M. (2018): The B cell response to citrullinated antigens in the development of rheumatoid arthritis. In: *Nature reviews. Rheumatology* 14 (3), S. 157–169. DOI: 10.1038/nrrheum.2018.10.

Schett, Georg; Stach, Christian; Zwerina, Jochen; Voll, Reinhard; Manger, Bernhard (2008): How antirheumatic drugs protect joints from damage in rheumatoid arthritis. In: *Arthritis & Rheumatism* 58 (10), S. 2936–2948. DOI: 10.1002/art.23951.

Schlaak, J. F.; Pfers, I.; zum Meyer Büschenfelde, K. H.; Märker-Hermann, E. (1996): Different cytokine profiles in the synovial fluid of patients with osteoarthritis, rheumatoid arthritis and seronegative spondylarthropathies. In: *Clinical and experimental rheumatology* 14 (2), S. 155–162.

Schneider, Caroline A.; Rasband, Wayne S.; Eliceiri, Kevin W. (2012): NIH Image to ImageJ: 25 years of image analysis. In: *Nature methods* 9 (7), S. 671–675. DOI: 10.1038/nmeth.2089.

Schöler, H. R.; Dressler, G. R.; Balling, R.; Rohdewohld, H.; Gruss, P. (1990): Oct-4: a germline-specific transcription factor mapping to the mouse t-complex. In: *The EMBO Journal* 9 (7), S. 2185–2195.

Schubert, David; Maier, Bert; Morawietz, Lars; Krenn, Veit; Kamradt, Thomas (2004): Immunization with glucose-6-phosphate isomerase induces T cell-dependent peripheral polyarthritis in genetically unaltered mice. In: *Journal of immunology (Baltimore, Md. : 1950)* 172 (7), S. 4503–4509. DOI: 10.4049/jimmunol.172.7.4503.

Schumacher, B. L.; Hughes, C. E.; Kuettner, K. E.; Caterson, B.; Aydelotte, M. B. (1999): Immunodetection and partial cDNA sequence of the proteoglycan, superficial zone protein, synthesized by cells lining synovial joints. In: *Journal of orthopaedic research : official publication of the Orthopaedic Research Society* 17 (1), S. 110–120. DOI: 10.1002/jor.1100170117.

Selesniemi, Kaisa; Albers, Renee E.; Brown, Thomas L. (2016): Id2 Mediates Differentiation of Labyrinthine Placental Progenitor Cell Line, SM10. In: *Stem cells and development* 25 (13), S. 959–974. DOI: 10.1089/scd.2016.0010.

Shahbazi, Marta N.; Zernicka-Goetz, Magdalena (2018): Deconstructing and reconstructing the mouse and human early embryo. In: *Nature cell biology* 20 (8), S. 878–887. DOI: 10.1038/s41556-018-0144-x.

Shannon, Paul; Markiel, Andrew; Ozier, Owen; Baliga, Nitin S.; Wang, Jonathan T.; Ramage, Daniel et al. (2003): Cytoscape: a software environment for integrated models of biomolecular interaction networks. In: *Genome research* 13 (11), S. 2498–2504. DOI: 10.1101/gr.1239303.

Shi, Jing; van de Stadt, Lotte A.; Levarht, E. W. Nivine; Huizinga, Tom W. J.; Hamann, Dörte; van Schaardenburg, Dirkjan et al. (2014): Anti-carbamylated protein (anti-CarP) antibodies precede the onset of rheumatoid arthritis. In: *Annals of the rheumatic diseases* 73 (4), S. 780–783. DOI: 10.1136/annrheumdis-2013-204154.

Shwartz, Yulia; Viukov, Sergey; Krief, Sharon; Zelzer, Elazar (2016): Joint Development Involves a Continuous Influx of Gdf5-Positive Cells. In: *Cell reports* 15 (12), S. 2577–2587. DOI: 10.1016/j.celrep.2016.05.055.

Sibley, C. P.; Coan, P. M.; Ferguson-Smith, A. C.; Dean, W.; Hughes, J.; Smith, P. et al. (2004): Placental-specific insulin-like growth factor 2 (Igf2) regulates the diffusional exchange characteristics of the mouse placenta. In: *Proceedings of the National Academy of Sciences of the United States of America* 101 (21), S. 8204–8208. DOI: 10.1073/pnas.0402508101.

Smolen, Josef S.; Aletaha, Daniel; Barton, Anne; Burmester, Gerd R.; Emery, Paul; Firestein, Gary S. et al. (2018): Rheumatoid arthritis. In: *Nature reviews. Disease primers* 4, S. 18001. DOI: 10.1038/nrdp.2018.1.

Smolen, Josef S.; Aletaha, Daniel; McInnes, Iain B. (2016): Rheumatoid arthritis. In: *The Lancet* 388 (10055), S. 2023–2038. DOI: 10.1016/S0140-6736(16)30173-8.

Soneson, Charlotte; Love, Michael I.; Robinson, Mark D. (2015): Differential analyses for RNA-seq: transcript-level estimates improve gene-level inferences. In: *F1000Research* 4, S. 1521. DOI: 10.12688/f1000research.7563.2.

Sozen, Berna; Amadei, Gianluca; Cox, Andy; Wang, Ran; Na, Ellen; Czukiewska, Sylwia et al. (2018): Self-assembly of embryonic and two extra-embryonic stem cell types into gastrulating embryo-like structures. In: *Nature cell biology* 20 (8), S. 979–989. DOI: 10.1038/s41556-018-0147-7.

Stegle, Oliver; Teichmann, Sarah A.; Marioni, John C. (2015): Computational and analytical challenges in single-cell transcriptomics. In: *Nature reviews. Genetics* 16 (3), S. 133–145. DOI: 10.1038/nrg3833.

Stephenson, William; Donlin, Laura T.; Butler, Andrew; Rozo, Cristina; Bracken, Bernadette; Rashidfarrokhi, Ali et al. (2018): Single-cell RNA-seq of rheumatoid arthritis synovial tissue using low-cost microfluidic instrumentation. In: *Nature communications* 9 (1), S. 791. DOI: 10.1038/s41467-017-02659-x.

Svensson, Mattias N. D.; Zoccheddu, Martina; Yang, Shen; Nygaard, Gyrid; Secchi, Christian; Doody, Karen M. et al. (2020): Synoviocyte-targeted therapy synergizes with TNF inhibition in arthritis reversal. In: *Science advances* 6 (26), eaba4353. DOI: 10.1126/sciadv.aba4353.

Tak, Paul Peter; Bresnihan, Barry (2000): The pathogenesis and prevention of joint damage in rheumatoid arthritis: Advances from synovial biopsy and tissue analysis. In: *Arthritis & Rheumatism* 43 (12), S. 2619–2633. DOI: 10.1002/1529-0131(200012)43:12<2619::AID-ANR1>3.0.CO;2-V.

Takahashi, Kazutoshi; Tanabe, Koji; Ohnuki, Mari; Narita, Megumi; Ichisaka, Tomoko; Tomoda, Kiichiro; Yamanaka, Shinya (2007): Induction of pluripotent stem cells from adult human fibroblasts by defined factors. In: *Cell* 131 (5), S. 861–872. DOI: 10.1016/j.cell.2007.11.019.

Takahashi, Kazutoshi; Yamanaka, Shinya (2006): Induction of pluripotent stem cells from mouse embryonic and adult fibroblast cultures by defined factors. In: *Cell* 126 (4), S. 663–676. DOI: 10.1016/j.cell.2006.07.024.

Takano, Shotaro; Uchida, Kentaro; Miyagi, Masayuki; Inoue, Gen; Fujimaki, Hisako; Aikawa, Jun et al. (2016): Nerve Growth Factor Regulation by TNF-α and IL-1β in Synovial Macrophages and Fibroblasts in Osteoarthritic Mice. In: *Journal of immunology research* 2016, S. 5706359. DOI: 10.1155/2016/5706359.

Takaoka, Katsuyoshi; Yamamoto, Masamichi; Hamada, Hiroshi (2011): Origin and role of distal visceral endoderm, a group of cells that determines anterior-posterior polarity of the mouse embryo. In: *Nature cell biology* 13 (7), S. 743–752. DOI: 10.1038/ncb2251.

Takaoka, Katsuyoshi; Yamamoto, Masamichi; Shiratori, Hidetaka; Meno, Chikara; Rossant, Janet; Saijoh, Yukio; Hamada, Hiroshi (2006): The mouse embryo autonomously acquires anterior-posterior polarity at implantation. In: *Developmental cell* 10 (4), S. 451–459. DOI: 10.1016/j.devcel.2006.02.017.

Tan, Eng M.; Smolen, Josef S. (2016): Historical observations contributing insights on etiopathogenesis of rheumatoid arthritis and role of rheumatoid factor. In: *The Journal of experimental medicine* 213 (10), S. 1937–1950. DOI: 10.1084/jem.20160792.

Tanaka, S.; Kunath, T.; Hadjantonakis, A. K.; Nagy, A.; Rossant, J. (1998): Promotion of trophoblast stem cell proliferation by FGF4. In: *Science (New York, N.Y.)* 282 (5396), S. 2072–2075. DOI: 10.1126/science.282.5396.2072.

Tang, Fuchou; Barbacioru, Catalin; Wang, Yangzhou; Nordman, Ellen; Lee, Clarence; Xu, Nanlan et al. (2009): mRNA-Seq whole-transcriptome analysis of a single cell. In: *Nature methods* 6 (5), S. 377–382. DOI: 10.1038/nmeth.1315.

Tew, Simon R.; Clegg, Peter D.; Brew, Christopher J.; Redmond, Colette M.; Hardingham, Timothy E. (2007): SOX9 transduction of a human chondrocytic cell line identifies novel genes regulated in primary human chondrocytes and in osteoarthritis. In: *Arthritis research & therapy* 9 (5), R107. DOI: 10.1186/ar2311.

Toyono, Tetsuya; Usui, Tomohiko; Yokoo, Seiichi; Taketani, Yukako; Nakagawa, Suguru; Kuroda, Masahiko et al. (2015): Angiopoietin-like 7 is an anti-angiogenic protein required to prevent vascularization of the cornea. In: *PloS one* 10 (1), e0116838. DOI: 10.1371/journal.pone.0116838.

Trentham, D. E.; Dynesius, R. A.; David, J. R. (1978): Passive transfer by cells of type II collagen-induced arthritis in rats. In: *The Journal of clinical investigation* 62 (2), S. 359–366. DOI: 10.1172/JCI109136.

Trouw, Leendert A.; Rispens, Theo; Toes, Rene E. M. (2017): Beyond citrullination: other post-translational protein modifications in rheumatoid arthritis. In: *Nature reviews. Rheumatology* 13 (6), S. 331–339. DOI: 10.1038/nrrheum.2017.15.

Turner, Jason D.; Filer, Andrew (2015): The role of the synovial fibroblast in rheumatoid arthritis pathogenesis. In: *Current opinion in rheumatology* 27 (2), S. 175–182. DOI: 10.1097/BOR.0000000000000148.

van Lent, P. L. E. M.; Blom, A. B.; van der Kraan, P.; Holthuysen, A. E. M.; Vitters, E.; van Rooijen, N. et al. (2004): Crucial role of synovial lining macrophages in the promotion of transforming growth factor beta-mediated osteophyte formation. In: *Arthritis & Rheumatism* 50 (1), S. 103–111. DOI: 10.1002/art.11422.

Walker, J. G.; Ahern, M. J.; Coleman, M.; Weedon, H.; Papangelis, V.; Beroukas, D. et al. (2006): Expression of Jak3, STAT1, STAT4, and STAT6 in inflammatory arthritis: unique Jak3 and STAT4 expression in dendritic cells in seropositive rheumatoid arthritis. In: *Annals of the rheumatic diseases* 65 (2), S. 149–156. DOI: 10.1136/ard.2005.037929.

Walz, A.; Burgener, R.; Car, B.; Baggiolini, M.; Kunkel, S. L.; Strieter, R. M. (1991): Structure and neutrophil-activating properties of a novel inflammatory peptide (ENA-78) with homology to interleukin 8. In: *The Journal of experimental medicine* 174 (6), S. 1355–1362. DOI: 10.1084/jem.174.6.1355.

Wamaitha, Sissy E.; Del Valle, Ignacio; Cho, Lily T. Y.; Wei, Yingying; Fogarty, Norah M. E.; Blakeley, Paul et al. (2015): Gata6 potently initiates reprograming of pluripotent and differentiated cells to extraembryonic endoderm stem cells. In: *Genes & development* 29 (12), S. 1239–1255. DOI: 10.1101/gad.257071.114.

Waschke, Jens; Böckers, Tobias M.; Paulsen, Friedrich (2015): Anatomie. Das Lehrbuch. 1. Aufl. München: Elsevier Urban & Fischer. Online verfügbar unter http://institut.elsevierelibrary.de/product/sobotta-lehrbuch-anatomie.

Weber, Susanne; Eckert, Dawid; Nettersheim, Daniel; Gillis, Ad J. M.; Schäfer, Sabine; Kuckenberg, Peter et al. (2010): Critical function of AP-2 gamma/TCFAP2C in mouse embryonic germ cell maintenance. In: *Biology of reproduction* 82 (1), S. 214–223. DOI: 10.1095/biolreprod.109.078717.

Wei, Kevin; Korsunsky, Ilya; Marshall, Jennifer L.; Gao, Anqi; Watts, Gerald F. M.; Major, Triin et al. (2020): Notch signalling drives synovial fibroblast identity and arthritis pathology. In: *Nature* 582 (7811), S. 259–264. DOI: 10.1038/s41586-020-2222-z.

Wen, Jing; Zeng, Yanwu; Fang, Zhuoqing; Gu, Junjie; Ge, Laixiang; Tang, Fan et al. (2017): Single-cell analysis reveals lineage segregation in early post-implantation mouse embryos. In: *The Journal of biological chemistry* 292 (23), S. 9840–9854. DOI: 10.1074/jbc.M117.780585.

Werling, Uwe; Schorle, Hubert (2002): Transcription factor gene AP-2 gamma essential for early murine development. In: *Molecular and cellular biology* 22 (9), S. 3149–3156. DOI: 10.1128/MCB.22.9.3149-3156.2002.

Wickham, Hadley (2016): ggplot2. Elegant graphics for data analysis. Unter Mitarbeit von Carson Sievert. Second edition. Cham: Springer International Publishing (Use R!). Online verfügbar unter http://gbv.eblib.com/patron/FullRecord.aspx?p=4546676.

Wu, Xunwei; Li, Shaohua; Chrostek-Grashoff, Anna; Czuchra, Aleksandra; Meyer, Hannelore; Yurchenco, Peter D.; Brakebusch, Cord (2007): Cdc42 is crucial for the establishment of epithelial polarity during early mammalian development. In: *Developmental dynamics : an official publication of the American Association of Anatomists* 236 (10), S. 2767–2778. DOI: 10.1002/dvdy.21309.

Yap, Hooi-Yeen; Tee, Sabrina Zi-Yi; Wong, Magdelyn Mei-Theng; Chow, Sook-Khuan; Peh, Suat-Cheng; Teow, Sin-Yeang (2018): Pathogenic Role of Immune Cells in Rheumatoid Arthritis: Implications in Clinical Treatment and Biomarker Development. In: *Cells* 7 (10). DOI: 10.3390/cells7100161.

Ye, Jin; Rawson, Robert B.; Komuro, Ryutaro; Chen, Xi; Davé, Utpal P.; Prywes, Ron et al. (2000): ER Stress Induces Cleavage of Membrane-Bound ATF6 by the Same

Proteases that Process SREBPs. In: *Molecular cell* 6 (6), S. 1355–1364. DOI: 10.1016/S1097-2765(00)00133-7.

Ying, Qi-Long; Stavridis, Marios; Griffiths, Dean; Li, Meng; Smith, Austin (2003): Conversion of embryonic stem cells into neuroectodermal precursors in adherent monoculture. In: *Nature biotechnology* 21 (2), S. 183–186. DOI: 10.1038/nbt780.

Ying, Y.; Liu, X. M.; Marble, A.; Lawson, K. A.; Zhao, G. Q. (2000): Requirement of Bmp8b for the generation of primordial germ cells in the mouse. In: *Molecular endocrinology (Baltimore, Md.)* 14 (7), S. 1053–1063. DOI: 10.1210/mend.14.7.0479.

Ying, Y.; Zhao, G. Q. (2001): Cooperation of endoderm-derived BMP2 and extraembryonic ectoderm-derived BMP4 in primordial germ cell generation in the mouse. In: *Developmental biology* 232 (2), S. 484–492. DOI: 10.1006/dbio.2001.0173.

Yoo, Seung-Ah; You, Sungyong; Yoon, Hyung-Ju; Kim, Dong-Ho; Kim, Hyun-Sook; Lee, Kyungho et al. (2012): A novel pathogenic role of the ER chaperone GRP78/BiP in rheumatoid arthritis. In: *The Journal of experimental medicine* 209 (4), S. 871–886. DOI: 10.1084/jem.20111783.

Yoshimizu, T.; Sugiyama, N.; Felice, M. de; Yeom, Y. I.; Ohbo, K.; Masuko, K. et al. (1999): Germline-specific expression of the Oct-4/green fluorescent protein (GFP) transgene in mice. In: *Development, growth & differentiation* 41 (6), S. 675–684. DOI: 10.1046/j.1440-169x.1999.00474.x.

Yu, Guangchuang; Wang, Li-Gen; Han, Yanyan; He, Qing-Yu (2012): clusterProfiler: an R package for comparing biological themes among gene clusters. In: *Omics : a journal of integrative biology* 16 (5), S. 284–287. DOI: 10.1089/omi.2011.0118.

Yu, Junying; Vodyanik, Maxim A.; Smuga-Otto, Kim; Antosiewicz-Bourget, Jessica; Frane, Jennifer L.; Tian, Shulan et al. (2007): Induced pluripotent stem cell lines derived from human somatic cells. In: *Science (New York, N.Y.)* 318 (5858), S. 1917–1920. DOI: 10.1126/science.1151526.

Zhang, Cheng-Hai; Gao, Yao; Jadhav, Unmesh; Hung, Han-Hwa; Holton, Kristina M.; Grodzinsky, Alan J. et al. (2021): Creb5 establishes the competence for Prg4 expression in articular cartilage. In: *Communications biology* 4 (1), S. 332. DOI: 10.1038/s42003-021-01857-0.

Zhang, Fan; Wei, Kevin; Slowikowski, Kamil; Fonseka, Chamith Y.; Rao, Deepak A.; Kelly, Stephen et al. (2019a): Defining inflammatory cell states in rheumatoid arthritis joint synovial tissues by integrating single-cell transcriptomics and mass cytometry. In: *Nature immunology* 20 (7), S. 928–942. DOI: 10.1038/s41590-019-0378-1.

Zhang, Shaopeng; Chen, Tianzhi; Chen, Naixin; Gao, Dengfeng; Shi, Bingbo; Kong, Shuangbo et al. (2019b): Implantation initiation of self-assembled embryo-like structures generated using three types of mouse blastocyst-derived stem cells. In: *Nature communications* 10 (1), S. 496. DOI: 10.1038/s41467-019-08378-9.